

POLITECNICO
MILANO 1863

**School of Industrial and Information Engineering**

**Engineering Physics**

# Design, realization and characterization of an experimental setup for Transient Reflectivity experiments

*Author:*
Bruno Moio

*Supervisor:*
Prof. Mauro Nisoli
*Assistant Supervisor:*
Dr. Matteo Lucchini

October 3, 2018

*A mia madre, mio padre e mia sorella. A Simone. Ad Anto e Anto. A tutti coloro che lo hanno reso possibile.*

# Contents

List of Figures 4

Abstract 7

Sommario 9

Introduction 10

Chapter 1. Transient Reflection 12

Chapter 2. Experimental Setup 16
1. Laser Source 16
2. Pulse Compression Stage 20
3. HHG Generation Chamber and Recombination Chamber 27
4. ToF spectrometer 30
5. Reflectometer Chamber 33
6. XUV Spectrometer 37

Chapter 3. Experimental Characterization of XUV Pulses 40
1. FROG 40
2. RABBITT 48
3. FROG CRAB 65

Chapter 4. Benchmarking the Experimental Setup 77
1. Silicon Sample 79
2. Titanium Sample 82
3. Germanium Sample 85

Chapter 5. Conclusions and future perspectives 87

Appendix A. Acousto-optic modulators 89

Appendix B. High-order harmonic generation 96

Appendix C. Calculation of angle-resolved reflectance 106

Appendix D. Determination of the refractive index 111

Bibliography 112

Acknowledgments 116

# List of Figures


2.1 Schematic representation of the CPA system. 17

2.2 Amplification in the regenerative amplifier. 19

2.3 Self-phase modulation. 22

2.4 Spectral broadening after the hollow-core fiber. 23

2.5 Laser beam pointing stabilization system 25

2.6 Fiber and chirp mirrors. 26

2.7 HHG cells. 28

2.8 HHG and recombination chambers. 30

2.9 Time of flight electron spectrometer. 32

2.10 Reflectometer chamber. 33

2.11 Sample and mirror holders. 35

2.12 Second mirror holder. 36

2.13 XUV spectrometer. 38

2.14 Measured MCP gain. 39

2.15 Example of a measured XUV spectrum. 39

3.1 Iterative procedure for reconstruction with FROG. 42

3.2 SHG FROG setup. 45

3.3 FROG trace for longer pulses. 46

3.4 Reconstruction of the IR pulse. 47

3.5 FROG trace for short pulses. 47

3.6 Reconstruction of the IR pulse. 48

3.7 Principle of the RABBITT. 49

3.8 RABBITT trace. 51
3.9 Sideband. 53
3.10 Fourier transform of the sideband signal. 54
3.11 Filtered sideband. 55
3.12 Fit of the filtered sideband. 55
3.13 Harmonic phase difference from RABBITT. 56
3.14 Attosecond pulse train from RABBITT. 57
3.15 XUV photon spectrum. 58
3.16 RABBITT with full spectrum. 59
3.17 Reconstructed complex spectrum. 61
3.18 RABBITT trace for short pulses. 62
3.19 XUV photon spectrum for short pulses. 63
3.20 Harmonic phase differences in the case of short pulses. 63
3.21 Infinite APT with filled hollow-core fiber. 64
3.22 Reconstruction of the XUV bursts with filled hollow-core fiber. 65
3.23 Electron spectrum correction. 71
3.24 CRAB trace correction. 72
3.25 XUV APT with empty fiber. 72
3.26 Comparison of the reconstructed and experimental CRAB trace. 73
3.27 Comparison of the IR pulses reconstructed by FROG and CRAB. 74
3.28 Electron spectrum and CRAB trace correction. 75
3.29 CRAB IR and XUV reconstruction. 76

4.1 Gold reflectance. 79
4.2 Si reflectance. 81
4.3 Ti reflectance. 83

4.4 Ti reflectance with complex oxide structure. 84

4.5 Ge reflectance. 86

A.1 Basic operating principle of the AOPDF and AOPGCF. 90

B.1 Three-step model for high order harmonic generation. 97

B.2 Barrier width estimation. 98

B.3 Graphical solution of recombination equation. 100

B.4 Solution of recombination equation. 102

B.5 Electron kinetic energy 103

B.6 Electron kinetic energy as a function of the recombination time 105

C.1 Multilayer structure. 107

## Abstract

In the recent years, the interest in table-top extreme-ultraviolet (XUV) sources, generating ultra-short pulses in the attosecond time domain, has grown. Fast electron dynamics can be investigated in a pump-and-probe scheme, using such very short pulses. Indeed, due to their short duration, the resulting temporal resolution is enough for assessing such phenomena with very high precision. Understanding the ultra-fast dynamics of electrons can give the chance to unveil hidden properties of matter, from standard semiconductors to much more exotic compounds, or even disclose unknown phenomena. The impact of this can be significant, as in many technological fields, like in microelectronics, a major breakthrough is awaited for overcoming the intrinsic limitations of the classical schemes those sectors strongly rely on.

In this perspective, our final aim is to use ultra-short pulses obtained by means of a well known process, called high-order harmonic generation (HHG), to study the electron dynamics in solids, despite we can also use gas samples. To do so, we plan to perform experiments and measure the transient reflectance of the XUV radiation, after the excitation of the sample by means of an infrared (IR) short laser pulse, with a duration of few femtoseconds. The reflectance can be linked to the electron properties of the sample.

In this work, we discuss the realization of an entire experimental setup for transient reflectivity pump-and-probe experiments. We will illustrate in details the main features of the experimental setup we have designed and built and present some preliminary results we have obtain for the characterization of the possible performances of the apparatus. Additionally, we will discuss some results for the benchmarking of the

setup, obtained by means of simplified experiments on well characterized samples.

# Sommario

Negli ultimi tempi si è osservato un crescente interesse per le sorgenti di radiazione nell'estremo ultravioletto (XUV), in grado di generare impulsi ultrabrevi della durata di centinaia di attosecondi. Tali impulsi sono particolarmente indicati per investigare le veloci dinamiche elettroniche poiché, data la loro breve durata, forniscono una risoluzione temporale tale da permettere di studiare questi fenomeni. La comprensione di tali dinamiche può dare la possibilità di svelare proprietà nascoste della materia, dai semiconduttori a composti più esotici, nonché scoprire nuovi e sconosciuti fenomeni. L'impatto di ciò sarebbe significativo, considerando che in molti campi tecnologici da tempo si attende una scoperta, tale da permettere di superare i limiti intrinseci degli schemi classici, verso cui si sta inesorabilmente andando.
In questa prospettiva, il nostro scopo finale è quello di usare impulsi ultrabrevi, ottenuti nell'ambito della generazione di armoniche di ordine elevato (HHG), per investigare le dinamiche elettroniche in solidi, sebbene nel nostro apparato sia possibile anche usare campioni gassosi. Per fare ciò, intendiamo condurre esperimenti per misurare come varia la riflettività dei campioni nel dominio XUV, in seguito all'eccitazione per mezzo di un impulso infrarosso (IR), dalla durata di pochi femtosecondi.
In questo lavoro discuteremo della realizzazione di un apparato per condurre esperimenti di riflettività transiente, in uno schema di pump-and-probe. Mostreremo in dettaglio le caratteristiche del sistema che

abbiamo progettato e costruito e presenteremo alcuni risultati preliminari, usati per caratterizzarne le possibili prestazioni. Inoltre, discuteremo di alcuni risultati di prova ottenuti su campioni noti, qui usati come riferimento.

# Introduction

The process of high-order harmonic generation (HHG) is widely used for the generation of ultra-short extreme ultra-violet (XUV) pulses, that can have a duration below 100 as. HHG is obtained by focusing an intense laser beam (intensity of about $10^{14}$ W/cm$^2$) onto a target (typically a noble gas). The result is the generation of XUV pulse trains or, with other small expedients, an isolated attosecond pulse. In any case, the resulting duration is very small, linked to the ultra broad spectra that can be obtained in such scheme. The extremely short duration makes such pulses the best tools for investigating processes that occur within an ultrafast timescale, like electron dynamics. Indeed, many processes that occur in molecules or solids evolve within femtoseconds or hundreds of attoseconds. For this reason, to study such processes a much shorter probe is required. The classical scheme we can use for such task is a pump-and-probe experiment. In this picture, a pump pulse is driven onto the sample and perturbs the electrons inside it. Then, a delayed pulse is used as a probe to interrogated the sample and some data are collected. Several measurements are done, at different delays between the pump and the probe.

To obtain such results, a complex apparatus is needed, both for generation of the XUV radiation and for the measurements. In particular, to perform transient reflectivity experiments on solid-state materials we have designed and built a reflectometer, a device capable of measuring the reflectance of the XUV radiation for a wide range of angles of incidence onto the sample. This, together with an XUV spectrometer, allows us to perform experiments that are resolved in angle, energy and

time.

The thesis work we present here is structured as follows:

- The **first chapter** gives a brief introduction to the field of transient reflectance measurements, highlighting the main advantages of this scheme, over other more mature methods;
- The **second chapter** illustrated in details the experimental setup we have designed and built, describing the apparatus, showing each stage used for the preparation of the IR pulse, generation of the XUV radiation and for carrying out the experiments;
- The **third chapter** describes the characterization of the XUV and IR pulses that we use for the experiments, using very sophisticated tools, like the FROG-CRAB methodology for the precise retrieval of the temporal features of the XUV pulses;
- The **fourth chapter** describes the results from some simple benchmark experiments, where we tested our apparatus on well known samples, to understand the reliability of what we have built;
- The **fifth and last chapter** draws the conclusions and illustrates some future perspectives for our setup.

CHAPTER 1

# Transient Reflection

Understanding the fast electronic response of solid materials to ultrashort pulses is crucial for the development of many applications, as fast electron dynamics is determinant in optoelectronics [**1**], hot carriers solar panels [**2**] and a plethora of other semiconductor-based devices. For this reason, a good comprehension of such phenomena is fundamental to efficiently develop those useful new-generation devices. An important tool that can be applied for such purpose is represented by the transient absorption. It is a well known methodology that was extensively used in the past for time-resolved experiments, for example with femtosecond resolution [**3**]. More recently, transient absorption in the attosecond time domain was successfully used to probe electron dynamics in gas samples, allowing to study phenomena like electron motion in krypton ions [**4**], autoionization of argon atoms [**5**] and interference of transiently bound electron wave packets in helium [**6**]. Recent works have also demonstrated the power of such technique, showing that extreme ultra-violet (XUV) transient absorption spectroscopy is a powerful tool to probe complex dynamics in solids. Indeed, it was used to demonstrate the possibility to control the properties of dielectrics, like silicon dioxide ($SiO_2$) [**7**], or semiconductors, like gallium nitride (GaN) [**8**], up to the petahertz regime, paving the way to ultrafast signal sampling and processing. Also, such technique was successfully employed for tracking the early steps of electron excitation in silicon [**9**], for addressing the electron density of states in warm dense copper [**10**] and it was used to study the dynamical Franz-Keldysh effect in polycrystalline diamond [**11**]. The main limit of such technique is that it requires the use of very thin samples (typically $< 100$ nm). If the

sample is too thick, the absorption is too strong and the transmitted signal would be too low to be properly detected. Very thin samples are, however, difficult to be created. Moreover, even from the practical point of view it is really complicated to set up an experiment of this kind, as thin samples are very delicate, they break easily and it is impossible to obtain a free-standing sample, so that special supports are required. For this reason, developing a tool to provide reliable, spectral and time-resolved information about the properties of thick, single-crystal sample is crucial for unveiling the ultrafast processes behind such solid materials. A good candidate for such role is transient reflectivity. Indeed, being not limited to very thin samples, transient reflectivity may easily access information about well-defined, optically thick samples and extend the range of applicability of such method to many systems, like in the study of internal dynamics in ferromagnetic alloys [**12**] to applications involving multilayer structures [**13**], also reducing the complications related to obtaining and handling the sample.

Another important feature of such experimental methodology is its large sensitivity to the surface. Recently such approach was successfully applied for time-resolved spectroscopic observations of electron dynamics in metals oxides [**14**]. This work, in particular, illustrated that the reflectance is tightly bound to the full, complex dielectric function $\epsilon(\omega) = \epsilon_1(\omega) + i\epsilon_2(\omega)$ of the sample, both to the real, dispersive part and the imaginary, absorptive part. Accessing such physical quantity is the main purpose of our work.

A special mention is required for another possible field of application of this technique. Indeed, being very sensitive to surface makes this a suitable tool for studying a very exotic yet extremely promising class of materials: the topological insulators. Topological effects are phenomena predicted to appear in substances with a strong spin-orbit interaction [**15**], showing up as metallic states on the surface of materials with otherwise insulating properties in the bulk [**16**]. Understanding

and possibly controlling this kind of phenomena would be a very important result from the technological point of view.

One of the main problem related to this method is that, to date, very few XUV transient reflectance experiments have been performed on single crystals, making it difficult to compare to known benchmark data. Also, it is not clear yet what is the sensitivity of an experiment of this kind to electron or lattice dynamics in single-crystals. In this perspective, our aim is to develop and validate an experimental setup able to track the evolution of the dielectric function in different samples by monitoring the reflectance in the XUV spectral range, subsequent to the excitation with a 800-nm, few-cycle pump pulse.

According to a previous work [**17**], where electron dynamics with femtosecond resolution is addressed, transient reflectivity is determined by different, spectrally separated contributions, involving electron and hole dynamics. Indeed, such phenomena determine a variation of the real and imaginary part of the dielectric function that results in a variation of the reflectance of the sample. The changes are due to state blocking as a consequence of the excitation of electron and holes in the system. In particular, the role of the carriers can be easily understood if we imagine the interaction with a single XUV energy. When an IR photon is absorbed, provided that its energy is larger than the band gap, it promotes an electron from the valence band (VB) to conduction band (CB). As a result, one state in the conduction band is occupied whereas another in the valence band is freed. When an XUV photon arrives, since its energy is much larger than the gap, it can often access and excite electrons from a core level. Transitions to the conduction band, where one state has been occupied, are inhibited whereas transitions to the valence band, presumably from lower energy levels, are enhanced since an additional free state at these energies is available. This perturbation continues until the excited electron relaxes back to the VB and the system returns to the ground state. Such process

of electron relaxation can be very complicated and our aim is to access it, by measuring how the XUV reflectance changes with time. In particular, we designed and built an experimental setup, able to measure transient reflectance with attosecond resolution, being this a very promising field, yet rarely explored [**18**].

CHAPTER 2

# Experimental Setup

In order to generate and characterize XUV ultrashort pulses and to use them for carrying out the experiments we have briefly discussed in the previous chapter, a complex equipment is needed. Our experimental setup consists in several sections:

- Laser source;
- Pulse compression apparatus;
- HHG generation and recombination chambers;
- Time of Flight (ToF) electron spectrometer;
- Reflectometer chamber;
- XUV spectrometer.

This setup was rearranged from another laser system that was not designed for experiments in solids. In particular, we had to reorganize most of the beam line, from the pulse compression system to the spectrometer, not to mention that we had to entirely design the reflectometer chamber from scratch. Also, we had to take care of all the secondary elements, like the computer software for running the apparatus.

## 1. Laser Source

The laser source is a commercial laser system, delivering pulses at 10-kHz with central wavelength of 800 nm. It consists of a Ti:Sapphire mode-locked oscillator by Femtolasers used as seed, followed by a three-stage chirped-pulse amplification (CPA) system made of a regenerative amplifier and two consecutive four-step multipass amplifiers (called preamplifier and booster), pumped with a high-power Q-switched Etna laser, delivering pulses at 532 nm with an average power of 130 W.

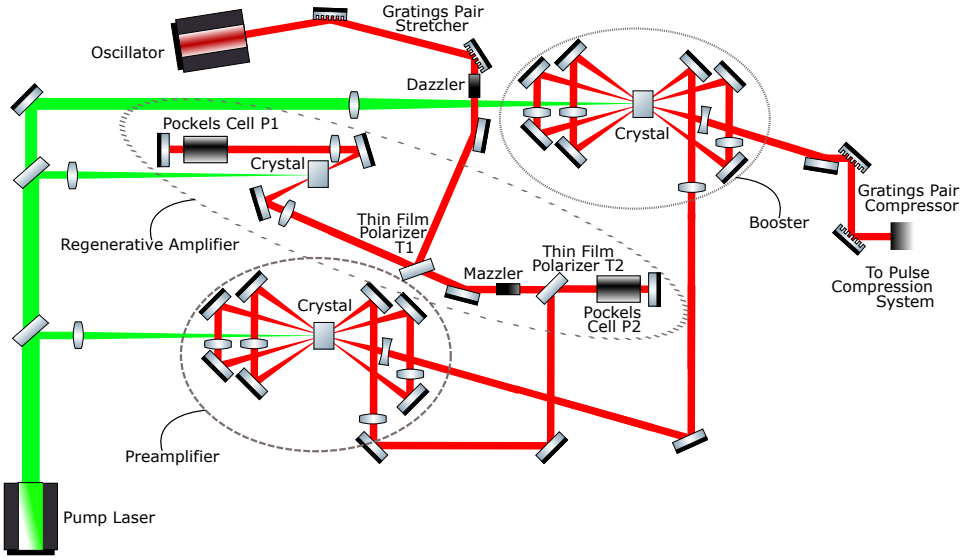


FIGURE 2.1. Schematic representation of the CPA system. The three amplification stages (regenerative amplifier, preamplifier and booster) are highlighted. The beam from the oscillator, with a power of about 120 mW, enters the regenerative amplifier after passing through a stretcher, that increases the time duration of the pulse to hundreds of femtoseconds. After four passages in the cavity, the beam has a power of 1.2 W. Then, the four passages in the preamplifier increase the power to about 2.4 W and finally the booster produces pulses with a power of about 30 W. Because of the compressor, a part of the energy is lost, but eventually the beam carries more than 19 W, corresponding to an energy of 1.9 mJ per pulse, and has a duration of 21 fs.

The overall laser system, schematically represented in Fig. 2.1, is able to give pulses with a duration of roughly 21 fs. At each stage of the amplification path, the IR pulses pass through a pumped crystal producing amplification of the input pulse. As high energies are typically reached, the crystal may be burnt because of the high peak intensity

of the pulse itself. This is the main reason why the pulse is stretched before entering the amplifiers. This approach is called chirped pulse amplification.

The first amplification stage is the regenerative amplifier. As the laser pulse is emitted by the oscillator, it has a well defined polarization. The first thin film polarizer (TFP, T1) is desgined to fully reflect the incoming beam. A TFP is, indeed, an optical element characterized by 100% reflectance for one polarization state and 100% transmittance for the other. The pulse, then, is focused onto the pumped crystal and it is amplified. After this, it enters the first Pockels cell (P1), a voltage-controlled optical device that exploits the Pockels effect to produce birefringence and control the polarization of the input beam. At the first passage, the Pockels cell is on and the polarization of the beam is changed. Therefore, the pulse is fully transmitted by both TFPs and is trapped inside the cavity. At each round trip, the pulse experiences a further amplification. However, if the number of subsequent passes becomes too large, the crystal starts being depleted and therefore the pulse is absorbed. In order to avoid this, after a number of passages that can be set by software via the Pockels cells controller, the second Pockels cell "opens", the polarization state of the beam is changed again, thus the second TFP can now reflect the pulse and send it to the next amplification stage. In our setup, the optimal number of passages to maximize the amplification and avoid re-absorption is four. Figure 2.2 shows the signal from a photodiode, representing the energy of the pulse after each round trip in the regenerative cavity. The typical output power we can obtain in this configuration, starting from 120 mW input power, is 1.2 W.

The second amplification stage is the preamplifier. The working principle of the preamplifier is quite similar to the one of the regenerative: the same pulse passes many times through a pumped crystal and at each passage it is amplified. The main difference is that now, the number of passages is set by hardware and, in our system, limited to four.

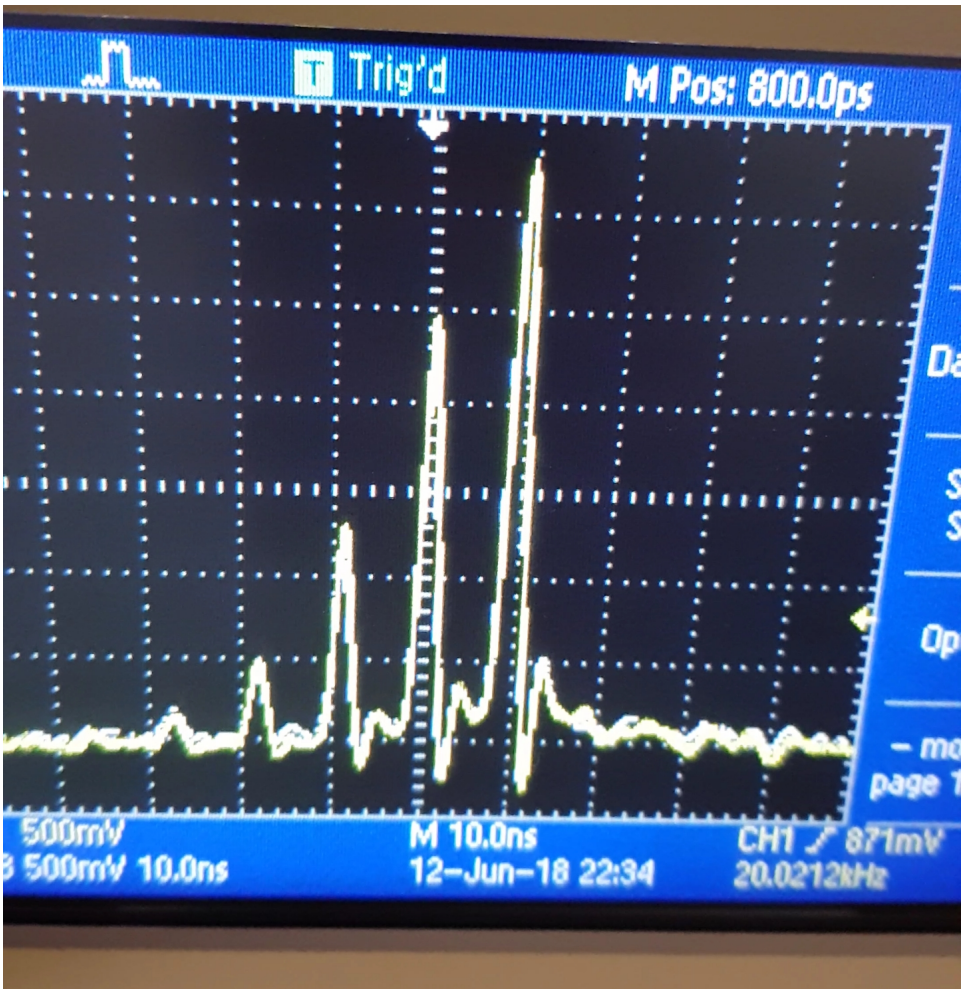


FIGURE 2.2. Signal from a photodiode representing the energy of the pulse at each passage in the regenerative amplifier cavity. The optimal number of passages before re-absorption occurs is four.

Indeed, in this second stage there is no cavity and the pulses are amplified in a multipass configuration. This is stage is typically able to more than double the power of the pulse.

The final stage is the so-called booster. It is nominally identical to the preamplifier but characterized by a much more important amplification effect (the majority of the pump energy is used to pump the booster

crystal, rason why it is cooled by liquid helium at -180°C), producing an output beam with 30 W power. Eventually, if we consider the losses mainly introduced by the compressor we obtain a final pulse of typically 19 W power, for an overall amplification factor of almost 160.
A special mention is owed to two important parts of the CPA system: the acousto-optic programmable dispersive filter (AOPDF, called Dazzler) and the acousto-optic programmable gain control filter (AOPGCF, called Mazzler). The first one, placed right after the stretcher, is able to provide full control of the pulse spectral amplitude and phase thus compensating for dispersion in a wide range, whereas the second one, placed inside the regenerative amplifier cavity, directly opposes to gain narrowing. Such devices are fundamental for obtaining the high performances our apparatus is capable of and play a very important role in obtaining a short pulse out of a CPA system. Indeed, one of the main issues in chirped-pulse amplifiers is the phenomenon of gain narrowing, preventing very short pulses from being obtained. Gain narrowing in the amplification system directly reflects in the narrowing of the band of the pulse, as central frequencies in the spectrum are amplified more than the peripheral ones. Since the bandwidth of the pulse is inversely proportional to its minimum time duration, the gain narrowing directly impacts the optimal temporal characteristics a pulse can have. This said, the reduction of gain narrowing is a required step for high performing systems. The use of AOPGCF for spectral amplitude shaping, together with AOPDF for spectral phase control, is very effective in coping with such a problem. A detailed description of the operating principle of such devices is presented in Appendix A

## 2. Pulse Compression Stage

Once properly amplified, the 21-fs pulse needs to be compressed, in order to reduce its time duration. The compression system consists of an hollow-core fiber filled with Neon, that produces spectral broadening

by a third order non-linear phenomenon called *self-phase modulation* (SPM), followed by a battery of chirp mirrors, producing the required compression.

Self-phase modulation is a phenomenon that arises as a consequence of the Kerr effect in $\chi^{(3)}$ materials (any material in principle will do). Such effect consists of having a refractive index of the material with a dependence on the intensity of the laser beam itself. The equation describing such phenomenon reads:

$$n = n_0 + n_2 I \tag{2.1}$$

where $n_2 \propto \chi^{(3)}$. Considering now a pulse with a Gaussian envelope and a carrier frequency $\omega_0$

$$E(z,t) = E_{env}(t)e^{i(k_0 z - \omega_0 t)} \tag{2.2}$$

where $k_0 = \omega_0 n/c = \omega_0 n_0/c + I\omega_0 n_2/c$ and $I = I(t) \propto |E_{env}(t)|^2$. Considering now the instantaneous frequency, defined as follows

$$\omega_i(t) := \frac{d}{dt}(\omega_0 t - k_0 z) = \frac{d}{dt}(\omega_0 t - z\omega_0 n_0/c - zI\omega_0 n_2/c) \tag{2.3}$$

we obtain

$$\omega_i(t) = \omega_0 - \frac{dI}{dt}(z\omega_0 n_2/c) \tag{2.4}$$

where $z$ is the position alongside the propagation in the $\chi^{(3)}$ material. As we can clearly see in figure 2.3, as the propagation goes on new frequencies are added to the pulse. In particular, for a positive $\chi^{(3)}$, "lower" frequencies are generated earlier in the pulse, whereas "higher" frequencies are generated later, producing the spectral broadening we already discussed. In figure 2.4 we show the comparison of the spectrum before and after the hollow-core fiber. As a result of this phenomenon, the output beam is non-transform-limited, since the spectrum has been broadened but the duration of the pulse is not changed. Therefore, additional pulse compression is required.

In our system we employed a 90-cm long fiber, with an internal diameter of 300 $\mu$m, filled with neon at 1.5 bar. Besides having a suitable broadening of the spectrum of the pulse, a part of the beam power

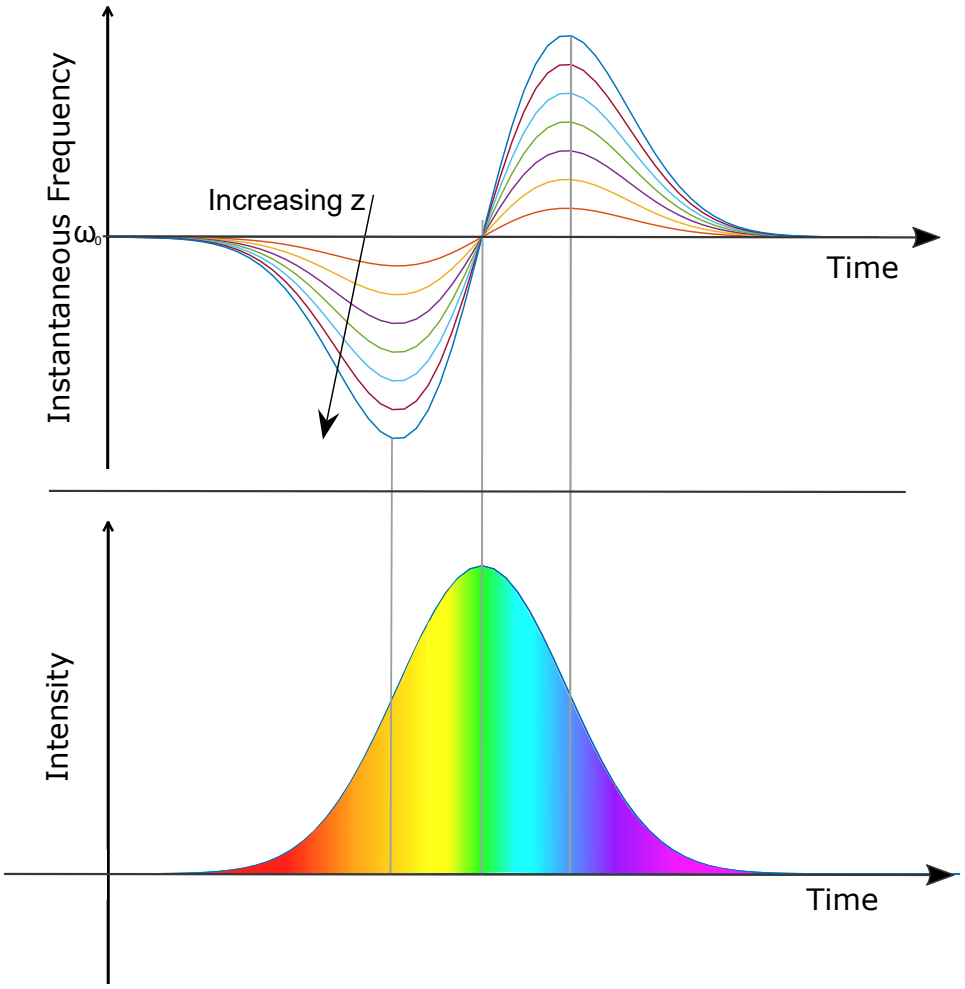


FIGURE 2.3. Self-phase modulation in a material with $\chi^{(3)} > 0$ for a Gaussian laser pulse: at different instants within the pulse temporal profile and for increasing interaction lengths in the medium ($z$), new frequencies are generated, following the derivative of the pulse intensity. In particular at earlier times, lower frequencies ($\omega < \omega_0$, where $\omega_0$ is the pulse central frequency) are generated. Notice that this phenomenon produces spectral broadening without changing the temporal characteristics of the pulse.

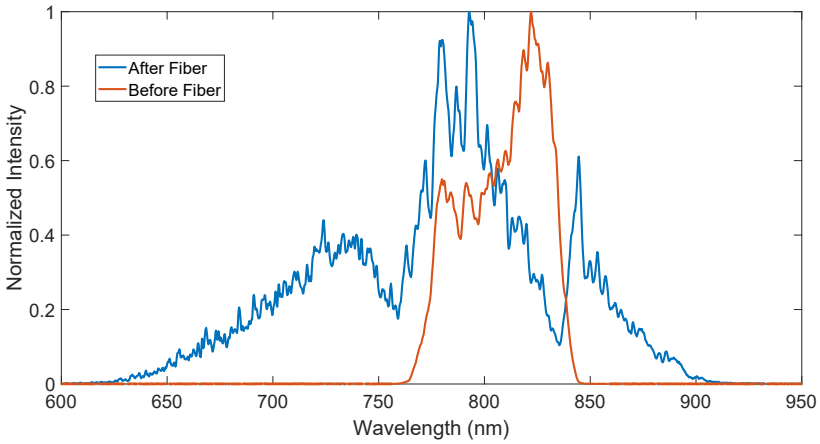


FIGURE 2.4. Spectral broadening after the hollow-core fiber: the red line shows the spectrum of the pulse before the hollow-core fiber whereas the blue line the one after it. The spectrum is broadened by SPM, from roughly 60-nm to more than 123-nm bandwidth, with only 1.5 bar of Ne in the fiber. The corresponding power loss is about 1 W.

is lost, due to absorption and other effects in the filled fiber. In particular, the amount of power we lose is on average 1 W. In order to achieve an optimal coupling with a Gaussian beam, the spot diameter has to be equal to about 2/3 of the fiber diameter [**21**]. To obtain this we used a telescope, made of the converging/diverging mirrors couple in figure 2.5, to change the beam spot size and fit to the optimal conditions. Finally, we mounted the fiber onto some micro-metric manipulators, allowing us to translate the fiber entrance and exit in a plane perpendicular to the propagation direction. This is useful since we can optimize the coupling efficiency by compensating by hand any possible position drift that may happen to the beam on daily basis.
Of course, optimization by such manipulators is useful but it cannot be used to compensate for fast fluctuations of the beam pointing. This is a crucial issue since the coupling efficiency dramatically depends on

the position and direction of the beam at the entrance of the fiber and even fluctuations of tens of microns can drop the performances of the system, not to mention that the pulses are so energetic that a slight misalignment can damage the fiber and permanently reduce the coupling efficiency. For this reason, we installed an active beam pointing stabilization system. Such device is able to provide stabilization of either position and direction at a specific point (the entrance of the fiber, of course) by compensating for fast fluctuations of the pointing using two piezoelectric actuators and for slow drifts using two motorized mirrors. The beam pointing stabilization system is shown in figure 2.5. The mirrors are driven by a micro-controller that elaborates the signals coming from two position-sensitive detectors (PSD), both able to identify the beam coordinates on their active areas. The first PSD (PSD A) is in the focus of the beam whereas the second one is right before it. Upon fixing the position of the two spots on the two PSDs (equivalent to fixing the beam in two positions along the propagation direction), the propagation line is fixed as well. The power of this stabilization system is not only its effectiveness (it can stabilize the beam pointing with a precision down to the micron) but also its versatility. Indeed, the micro-controller can run a special calibration procedure, consisting in simply moving the mirrors along some predefined paths and recording the position of the beam onto the detectors, by means of which it can "learn" the mirrors arrangement and find the optimal transfer function of the feedback loop. In this way, the stabilization system can be used with any arrangement and every modification of the system configuration requires only few steps for being again optimized.
After the fiber, the spectrally broadened pulse has to be compressed since, as we discussed, the SPM produces a chirped pulse (basically, it increases the bandwidth without changing the time duration). In order to do so, one could use a battery of chirp mirrors, as shown in figure 2.6.

A chirp mirror is a special kind of dielectric mirror, designed to reflect

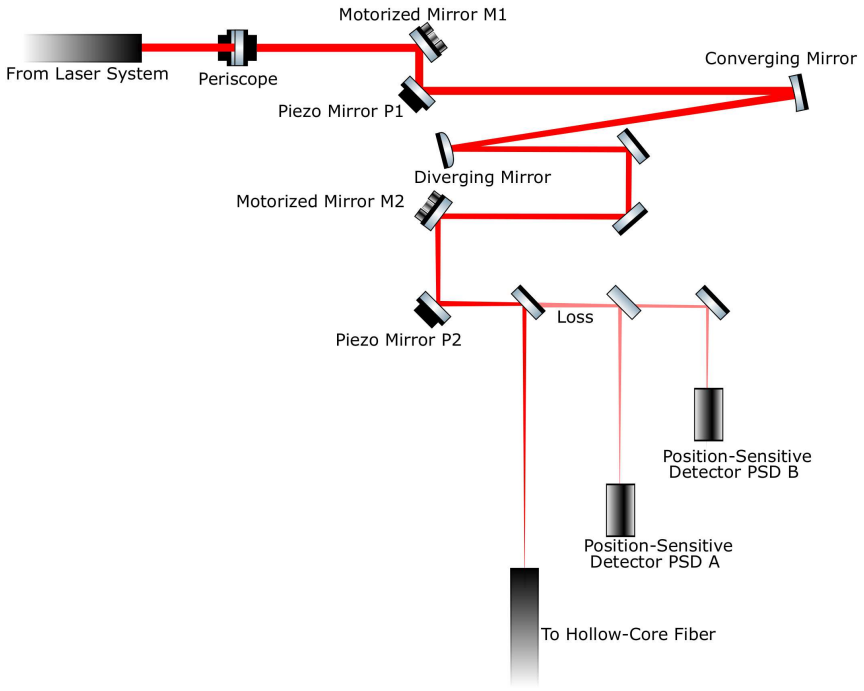


FIGURE 2.5. Laser beam pointing stabilization system: the two motorized mirrors (M1, M2) and piezo-mounted mirrors (P1, P2) are used to stabilize the position and direction of the beam at the entrance of the fiber, by means of the feedback signal produced by the two position-sensitive detectors (PSD A and B). The converging/diverging mirrors couple acts as a telescope and is used to change the beam spot size.

different wavelengths at different depths inside the mirror itself. In particular, since in order to compress a chirped pulse like the one we have after the fiber (where the lower frequencies are anticipated with respect to the higher ones) it is necessary to delay the longer wavelengths, the chirp mirrors we use reflect the higher energies early, right at the surface, whereas the lower energies penetrate a little inside the mirror before being reflected. As a result, the "red" part of the pulse is delayed whereas the "blue" part of the pulse is anticipated, resulting in

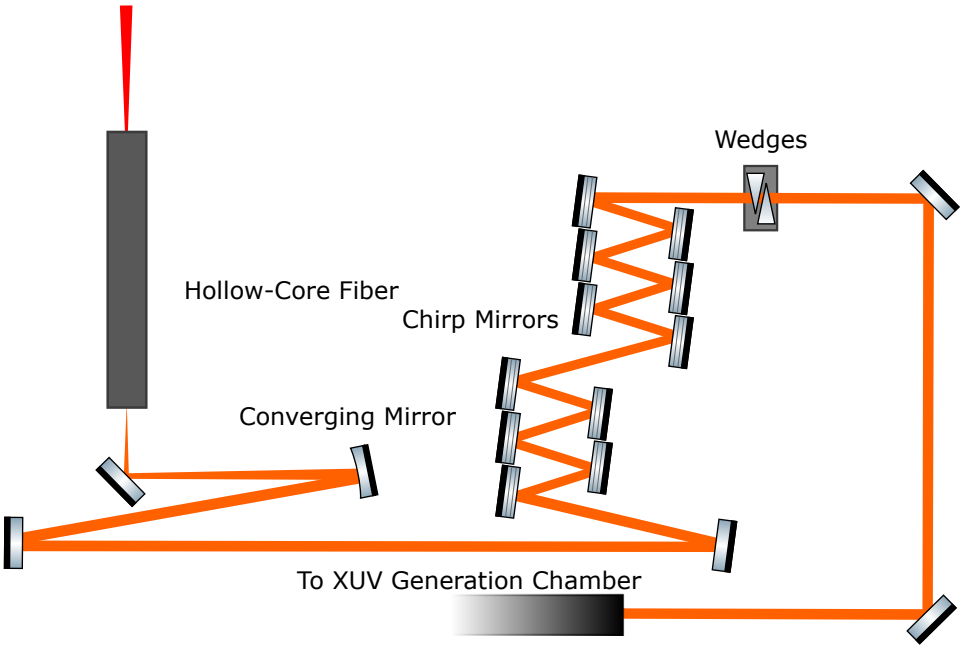


FIGURE 2.6. After the hollow-core fiber, the pulses need to be compressed. First the beam is collimated by a converging mirror and then driven onto a battery of eleven chirp mirrors, specially designed for compressing the pulses we have. For fine dispersion control the pulse travels through two wedges that can be inserted or removed.

a compressed pulse. The final pulse has a duration of about 10 fs, very close to its transform limited. Before entering the high-order harmonic generation chamber, the pulses pass through two fused silica wedges, mounted on a mechanical slide for fine positioning. The role of the wedges is to introduce negative dispersion after the chirp mirrors to finely optimize the pulse compression. Additionally, with the carrier-envelope phase (CEP) stabilization system activated (see Appendix A) the wedges can be used to control the value of the absolute phase.

## 3. HHG Generation Chamber and Recombination Chamber

Once the pulses are properly compressed, they can be used for high-order harmonic generation, referred to as HHG (a detailed description of the process is described in Appendix B). After the beam enters the HHG vacuum chamber, where the typical pressure is $10^{-7}$ mbar, through a Brewster-angle window, it is immediately split using a 60:40 beam splitter (BS), both because the intensity would be too much for our XUV line and because we need a part of the IR to be used as a probe or pump for our experiment. By means of two irises, electronically controlled from outside the chamber, the power of the beams can be finely tuned. The reflected part, with an energy of 500 $\mu$J per pulse, is focused using a 100-mm-radius converging mirror onto a cell, filled with Argon, where generation occurs. As seen in figure 2.7, the HHG cell we designed is a steel parallelepiped, with a 5-mm hole in it. It is 1-cm thick (despite we have also built a cell with 0.5-cm thickness, the rightmost one in the picture, to test the best configuration and in some cases it produces better results) and three of them are mounted onto an xyz-translation stage, controlled by software. The slides are mainly used to switch from one cell to another and to move the cell along the propagation direction: this, in some cases, may be used for optimization of the generation process. The hole is covered with aluminum tape and filled with gas (Ar in our case). When the beam is focused onto the cell, the laser digs a small hole in the tape, with the size of the beam spot, and HHG takes place: a train of XUV pulses is generated. The main advantage of this approach is the ease of use, as there is no need for extremely fine alignment of the beam and the cell can be easily replaced by replacing the aluminum tape only (we have however noticed that the same cell can be used for several times in a row without replacement).

The transmitted pulse (about 300 $\mu$J per pulse), goes through a controlled delay line, made of a simple retro-reflector mounted on a piezoelectric actuator, and will be used for pump and probe experiments

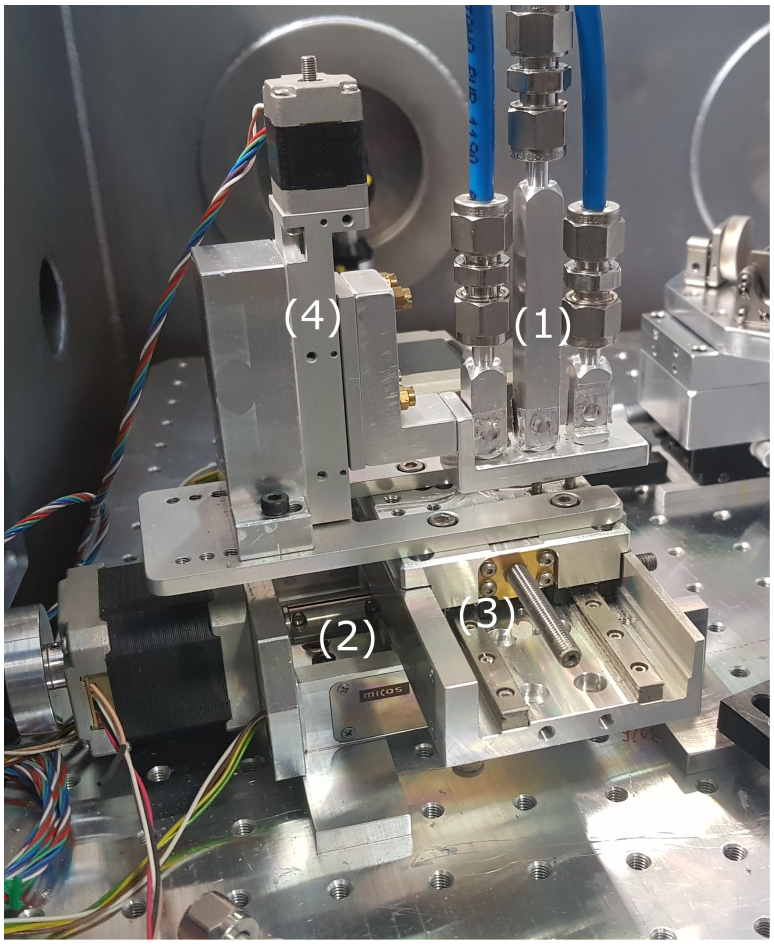


FIGURE 2.7. Picture of the three HHG cells in our system (1). Each cell consists of a simple parallelepiped with a small hole. When on use, the hole is covered with aluminum tape and filled with gas, using the valve on top of the cell. To switch from one cell to another, they are mounted on a translator (2). In principle, the support provides motion also in the other two directions by means of two other slits (3)(4) but it is practically used only for moving it along the propagation direction, for efficiency optimization.

(e.g. transient reflection), after the recombination with the generated XUV pulse. The recombination of the two pulses takes place in the recombination chamber. The residual IR on the XUV line is removed by means of an aluminum filters, mounted on a motorized wheel that allows to insert and remove the filter without opening the chamber. The filters are simply very thin layers of aluminum, characterized by almost zero transmission for the longer wavelengths, without excessively attenuating the XUV radiation. We use two different kinds of aluminum filters with different thickness (100 nm and 250 nm), mainly depending on the power of the IR radiation that has to be removed. Once the XUV beam is separated from the generating IR beam, the recombination is obtained by means of a drilled mirror, placed right after the filter wheel. It is a mirror with a 3-mm through-hole, oriented at 45° with respect to the surface normal. The XUV pulse passes through the hole whereas the IR from the delay line, impinging onto the mirror from the front side, is reflected. This simple scheme allows to have collinear propagation of the delayed IR and XUV pulses. Once the pulses are superimposed to one another, they are both focused by a gold-coated toroidal mirror, a special grazing-angle optical element mainly used to focus XUV pulses. This kind of elements is typically required for the manipulation of the XUV radiation, since incidence with small angle may degrade the beam because of the large absorption of the XUV in basically any material. Therefore, the use of standard mirrors is not recommended for this kind of radiation. However, it is able to focus almost any kind radiation, regardless the wavelength. The HHG cell, that we can consider as a point-like XUV source, is placed at 80 mm from the center of the toroidal mirror and is focused at the same distance after it. Before the recombination, the collimated IR beam is reflected by a diverging mirror with a virtual focus at the same distance from the toroidal mirror as the HHG cell. As a consequence, not only the XUV and IR are collinear but they are also focused in the same position, at 80 mm after the toroidal mirror. The basic scheme of

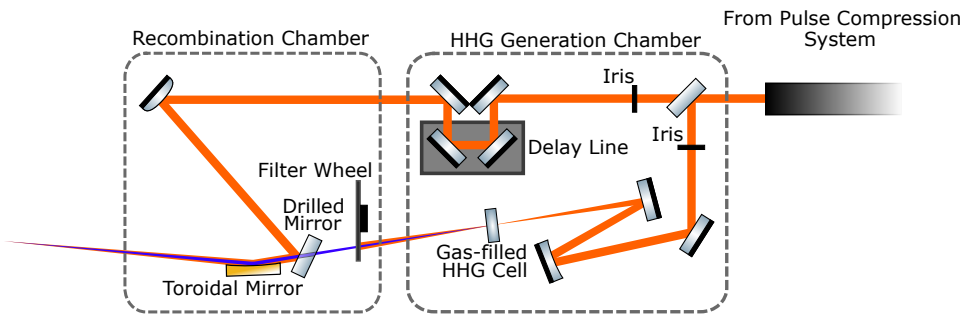


FIGURE 2.8. HHG and recombination chambers: a beam splitter is used to obtain two separated lines, the XUV line for high-order harmonic generation and the IR delay line. The recombination takes place by means of a drilled mirror and the beams are focused in the same position by a toroidal, gold-coated grazing-incidence mirror.

both the generation and recombination chamber is shown in figure 2.8.

## 4. ToF spectrometer

In order to characterize the XUV pulse in terms of time duration and chirp and for performing pump-and-probe experiments in gas phase, a time of flight (ToF) electron spectrometer is needed. The ToF allows for the measurement of electrons kinetic energy by measuring the time that it takes for the electrons to travel a known distance. It is clear that the larger the kinetic energy, the faster the electron and therefore the earlier the arrival onto the detector. The basic working principle is relatively easy to be understood: the chamber is filled with gas (Ne or Ar, for example) using a needle that injects gas at the focal point of the XUV/IR beam. The gas we use is typically a noble gas since we want to have single transitions only, in order to have an electron spectrum that resembles the photon spectrum as much as possible, only shifted in energy by the ionization potential of the gas. Indeed,

at the focal point XUV photons are absorbed by the gas atoms and photoelectrons are produced, but only by those harmonics having an energy larger than the ionization potential. Such electrons first interact with the IR pulse (as a result of this interaction, the measured electron spectra can be used to retrieve information on the characteristics of the XUV pulse, as shown in chapter 3). In a simple and general configuration, they are then collected and accelerated by some electron optics that modify the kinetic energy of the electrons, allowing to change the shape of the electron spectrum and, by properly setting the parameters, having it similar to the photon one. After this, the electron travel through the so-called drift tube, a metal cylinder held at a constant potential such that electron within experience no force. Inside this, the electrons with different speed are separated. Eventually, a microchannel plate (MCP) amplifies the single-electron signal, produced by each XUV photon ionizing the gas atoms in the chamber, and for each detection produces a current burst, that can be measured. A representation of a ToF spectrometer is exhibited in figure 2.9. In general, the measurements are done by recording, at each delay between the XUV and IR pulses, an entire electron spectrum, producing a trace that can be used for pulse reconstruction (Chapter 3). The detection is driven by a trigger, locking the beginning of the measurement to the emission of an IR pulse from the laser system. Then the system measures the time between the starting event and the detection of an electron. By using a power law, the resulting spectrum can be fitted and the energy of the electrons can be retrieved. Indeed, from simple dynamics and kinematics we have that

$$\begin{aligned} E_k &= \tfrac{1}{2} m_e v^2 \\ v &= \tfrac{L}{t_f} \end{aligned} \tag{2.5}$$

where $E_k$ is the electron kinetic energy, $m_e$ is its mass, $v$ its velocity, $L$ the ToF tube length and $t_f$ the "time of flight" as measured by the device. Notice that, for sake of simplicity, we have neglected any

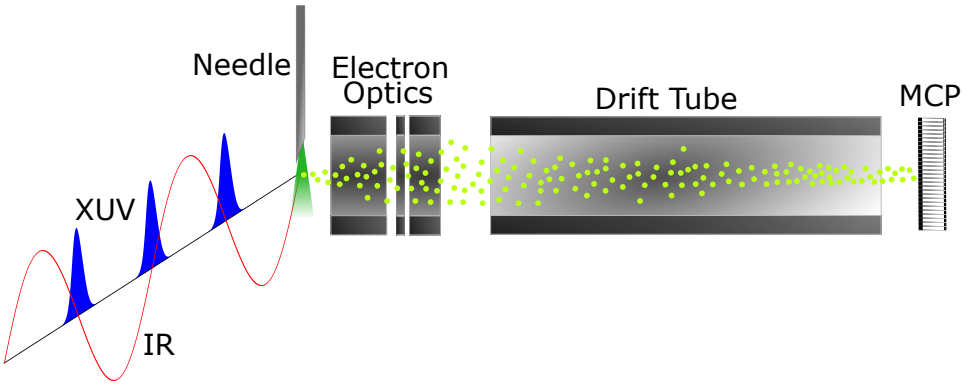


FIGURE 2.9. Basic structure of a time of flight (ToF) electron spectrometer. A needle injects gas at the focal point of the IR/XUV beams. The gas atoms are ionized and the emitted electrons are collected and focused by the electron optics. After this, they travel through the drift tube and are temporally separated, depending on their kinetic energy. Eventually, the detection takes place by means of a phosphorous screen, after the signal amplification by a micro-channel plate.

additional energy contribution due to the voltage that is applied to the ToF and have assumed that the electrons travel with a constant kinetic energy (the one they have when emitted) with no acceleration. If we now merge the two results and consider, in addition, that there can be some delay between the trigger and the actual electron emission ($t_0$) we obtain

$$E_k = \frac{1}{2} m_e \frac{L^2}{(t_f - t_0)^2} \tag{2.6}$$

Such relation binds the kinetic energy of the electron to its time of flight in the spectrometer tube. If we now consider the ionization potential ($I_p$) of the chemical species we have filled the ToF with, we can retrieve the photon energy as follows:

$$E_{XUV} = E_k + I_p \tag{2.7}$$

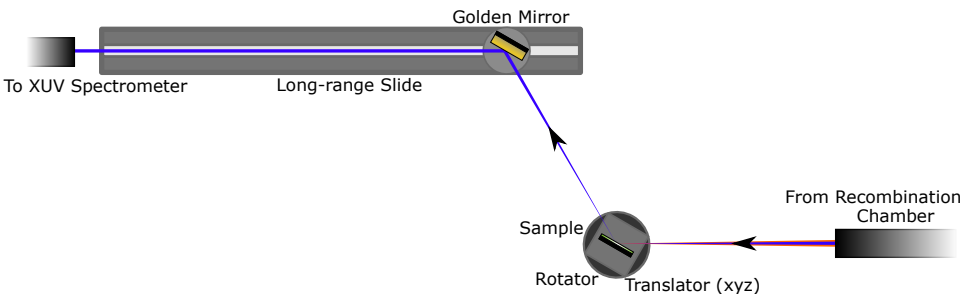


FIGURE 2.10. Reflectometer chamber: the XUV/IR pulses impinge on the sample and they are reflected at a given angle. The golden mirror mounted onto a rotator and a long-range slide is used to intercept the beam and sent it into the spectrometer, with the proper direction of propagation.

In conclusion, we can measure the trace $S(E_k, \tau)$, made of spectra measured at different IR/XUV delays, that can be used to fully characterize the XUV burst or do experiments in the gas phase.

## 5. Reflectometer Chamber

As our aim is to perform transient reflection experiments on solids as well as in gas samples, the reflectometer is the core of our apparatus. Unlike the rest of the beam line that we had to adapt from an existing system, we had to fully design this entire section from scratch, from the vacuum chamber to the sample and mirror holders, their movements and the computer software needed for their actuation. The reflectometer consists of two main elements allowing us to perform reflectance measurements in a wide range of angles of incidence onto the sample (the basic scheme is shown in figure 2.10). The first element is a motorized sample support, providing many degrees of freedom to the sample, such that we can translate it along the three directions in space, thanks to three motors (MP-21 by Micronix, with a resolution of 0.1 $\mu$m), and rotate it around one axis, using a rotor model PR-50SM by Micronix, with a resolution of 10m°. The sample support has also a mount for

a gold-coated mirror that can be positioned in place of the sample if a sample-free calibration is needed. The sample/mirror holder is shown in figure 2.11. It is made of two independent elements, mounted on the same roto-translational stage. The mirror support (the top element in figure 2.11) is simply a piece of steel with a 13-mm grove, designed to hold a gold-coated mirror, kept in position by a special silver-based glue. The mirror is used, in place of the sample, to collect background or reference data in our experiments. The sample holder is slightly more complex. As no vertical-tilt is allowed by the 3D-rototranslator only, we designed the sample support to implement manual vertical tilt. When the sample is mounted (and therefore the chamber is in air), we can use the screw to manually align the the beam reflected by the sample, to direct it in the same direction as the one reflected by the mirror. As a result, no massive correction of the vertical tilt of the second mirror (we will address it later on in the discussion) is needed when switching from the sample to the mirror and viceversa. The mirror and sample holders are then mounted onto a motorized stage that allows motion of the sample and the first mirror in the three directions in space, with a vertical range of 25 mm and horizontal ranges of 10 mm. The longer vertical range is needed for selecting the mirror or the sample to be in position. The 3D-translator is then assembled to a 360° rotator. The rotational degree of freedom is used to change the angle of incidence of the XUV pulse and the 3D-translational stage is used to change the position of the beam onto the sample.

Once the XUV photons interacts with the sample and are reflected back, they should be directed along a precise direction inside the spectrometer. For doing so, a second optical element is used. It is a golden mirror, similar to the one we use for reference measurements, able to intercept the beam that is reflected by the sample and send it into the spectrometer. To have full motion freedom, needed since we plan to run experiments in a wide range of angles of incidence, it is mounted to motorized supports (figure 2.12). First of all, the mirror is inserted in

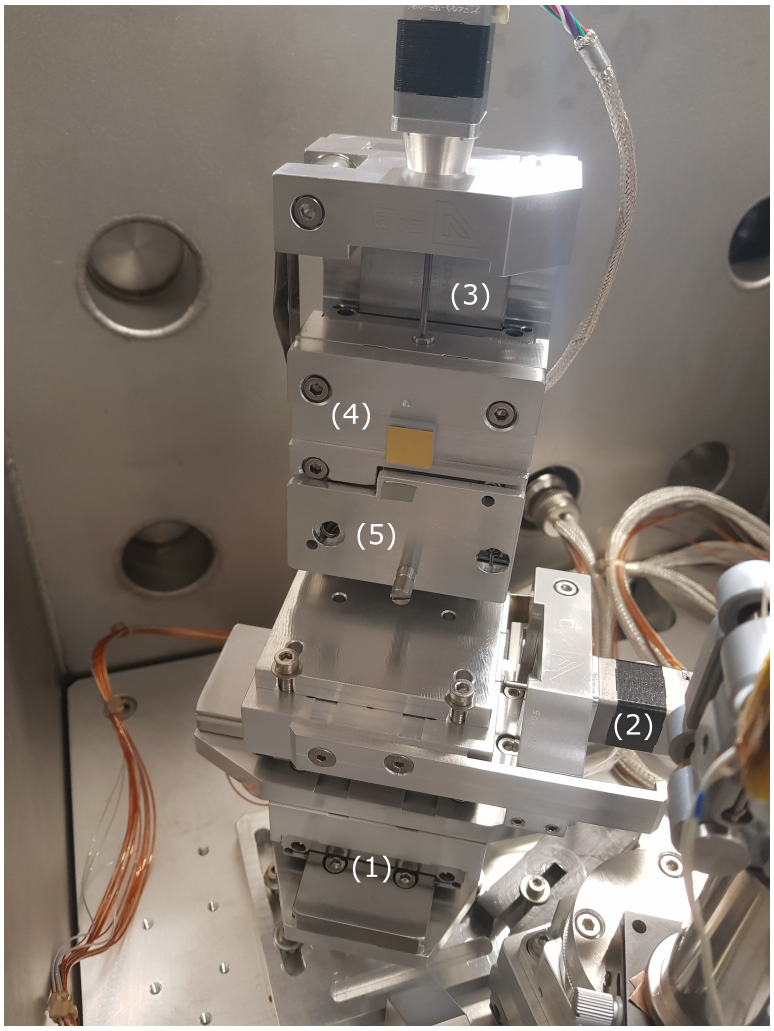


FIGURE 2.11. The sample and first mirror holders: two independent elements are screwed to the same motorized support, allowing for 3D-translation (1)(2)(3) and rotation (below the structure, not visible in the picture). The mirror holder (4) is a piece of steel with a groove to accomodate the golden mirror. The sample support (5) is a slab to which the sample is glued on and allows to vertically tilt the sample by means of a screw.

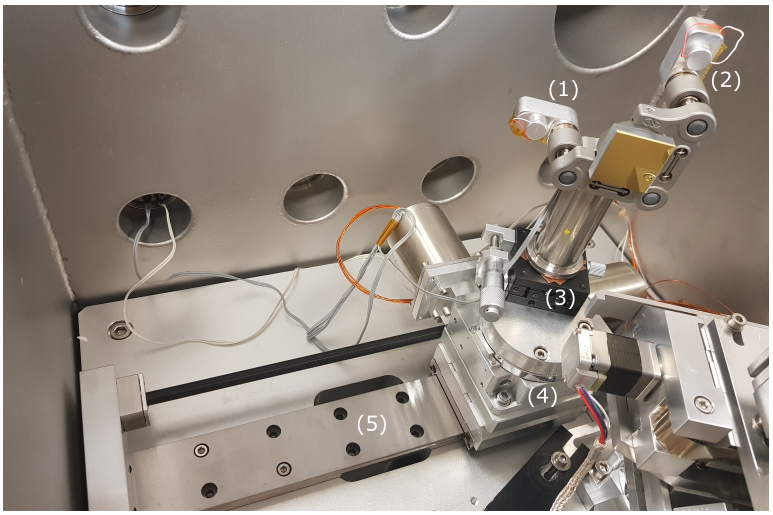


FIGURE 2.12. The second mirror is mounted to a motorized holder for full motion freedom. Two motors (1)(2) allow for very fine adjustment of the vertical and horizontal tilt of the mirror. A manual slit (3) is used for placing the mirror surface on the rotation axis of the rotor (4). The block is then mounted onto a long-range slide (5), able to translate the mirror for almost 200 mm

a motorized holder for very fine horizontal and vertical tilt, controlled by an external driver. The holder is placed onto a 360° rotator, like the one used in the first stage. The rotator is used to compensate for the angle variation of the beam propagation direction dictated by the sample holder, such that the beam at the entrance of the spectromater is propagating along the same direction as at the entrance of the reflectometer, besides a spatial shift. Between the mirror holder and the rotator we placed a manual slit, providing a translation of the mirror of about ± 10 mm. It is used to make sure that the surface of the mirror is aligned to the axis of rotation. Finally, the whole support is mounted to a long-range translator (model MP-21 by Micronix, with a resolution of 0.1 $\mu$m), able to shift the mirror for almost 200 mm. It is fundamental for intercepting the reflected beam, as even a small

variation of the angle of incidence onto the sample may produce a large change in the beam position alongside the propagation direction before the spectrometer.
With such system, upon properly setting the angle and position parameters of either the sample and the mirror, we can access the information about the sample reflection at any angle, spanning from less than 60° to almost 80°, in a time-resolved pump-and-probe scheme.

## 6. XUV Spectrometer

The final stage of our experimental setup is the XUV spectrometer. It is a simple device, used to spectrally analyze the XUV pulse after interacting with the sample. This configuration, together with the reflectometer, allows us to obtain measurements that are resolved both in angle and energy. The structure of the XUV spectrometer, as one can see in figure 2.13, is very simple: a diffraction grating (at grazing incidence, since working in the XUV spectral domain, just like the toroidal mirror in the recombination chamber) separates the different harmonics generated with the HHG process. The resulting spatially separated harmonics are characterized by a well known angular separation depending on the energy. Such relation can be used to determine which harmonic we are detecting at each position. The detection takes place using an MCP. As a matter of fact, this kind of detectors may typically show a variable gain over the active area, thus producing a little distortion to the measured spectra. To cope with that, we decided to perform some measurements to characterize it and measure the gain as a function of the position. The idea is the following: we chose one auxiliary harmonic (the narrowest) and using a translational stage placed under the MCP, we moved the detector and collected a spectrum for each position, sweeping the entire area of interest on the plate. The result is a set of single-harmonic spectra that we could compare one another to calibrate, pixel by pixel, the MCP gain. To compute the gain pattern what we did was to chose a position as a

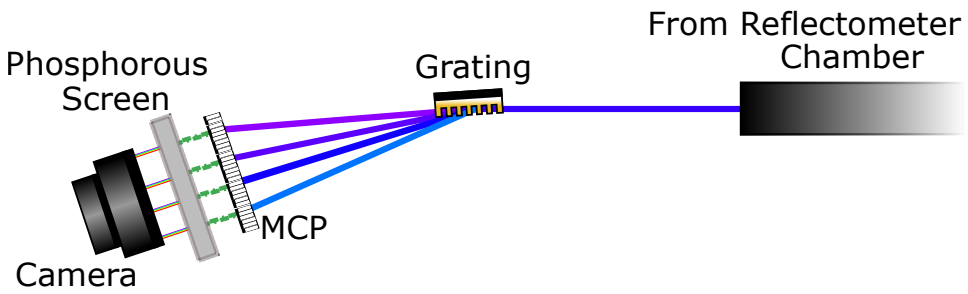


FIGURE 2.13. XUV spectrometer: a grazing-angle diffraction grating is used to spatially separate the different harmonics, since different wavelengths are diffracted at different angles. The harmonics are then collected by an MCP and converted to an electron signal, amplified by the MCP itself. The so-generated current pulse is accelerated towards a phosphorous screen that converts the electron kinetic energy to a light signal, in the visible wavelength range. Such signal is then imaged by a standard camera.

reference, with a defined relative gain of 1, and then compute, for each MCP position, the relative gain as the ratio between the harmonic in such position and the reference one. Considering the bandwidth of the harmonic we used as the reference, we were able to obtain a gain function with an estimated resolution of almost 10 pixels, corresponding to about 300 $\mu$m. Such function can be used to correct the measured spectra. Figure 2.14 shows the gain function we measured. To obtain a result that is defined at each position, we computed such function as a slice-by-slice 9-degree polynomial fit, along the longer axis. The result shows a variable gain function ranging from 0.2 to 2, with respect to the reference value we have discussed.

After the electron signal is generated and appreciably amplified by the MCP, the electron beam from the MCP is accelerated and then delivered to a phosphorous screen. It converts the energy carried by the electrons into photons in the visible wavelength range that are then

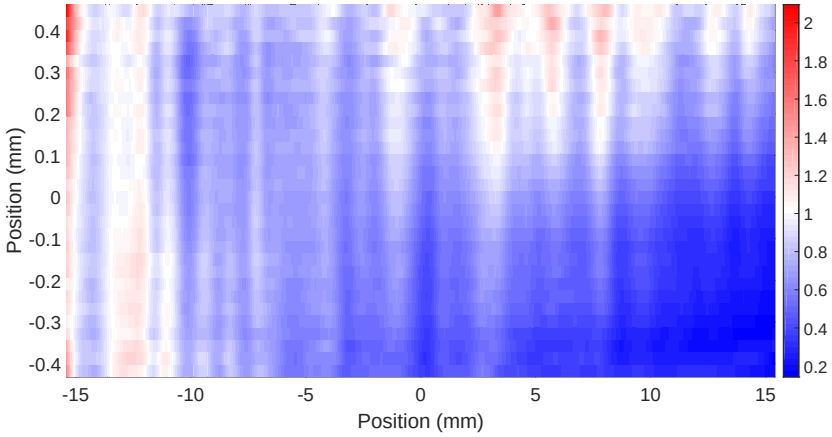


FIGURE 2.14. Measured MCP gain, at each position on the plate. The red areas are the ones with higher gain whereas the blue ones are characterized by lower gain, with respect to an arbitrary reference value (white areas).

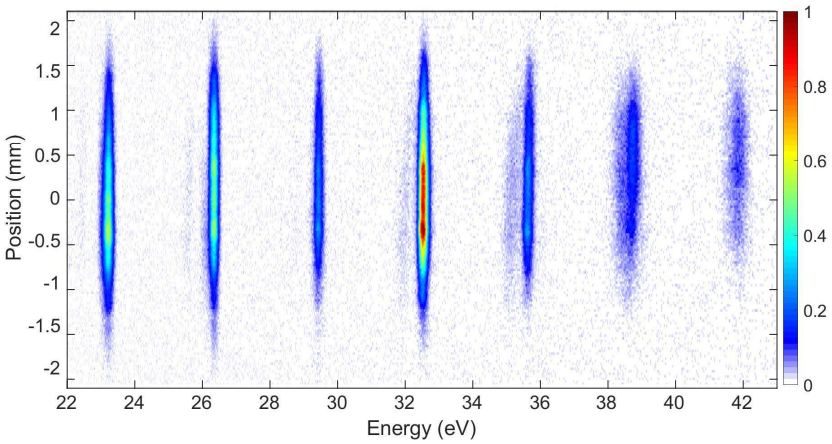


FIGURE 2.15. Example of a measured XUV spectrum. The lowest-energy harmonic is the $15^{th}$.

recorded by a standard camera. Figure 2.15 shows an experimental spectrum. The horizontal axis is the energy and the vertical axis represents the spatial extension of the harmonic. The harmonics that we have measured in the spectrum range from order 15 to 27.

CHAPTER 3

# Experimental Characterization of XUV Pulses

The first step to validate our experimental setup is to understand the temporal characteristics of the generated pulses. In particular, both the IR pulse and the generated XUV pulse train need to be characterized. In order to do so, several techniques can be used: FROG (frequency-resolved optical gating) [**22**], a method based on the measurement of a series of spectra and an iterative algorithm, is a robust method for the reconstruction of the IR pulse, whereas RABBITT (reconstruction of attosecond beatings by interference of two-photon transitions) [**23**] is suitable for the reconstruction of very long XUV pulse trains. Eventually, a very powerful tool, called frequency-resolved optical gating for complete reconstruction of attosecond bursts (FROG-CRAB) [**24**], can be used for a very robust and precise reconstruction of the XUV field.

## 1. FROG

Frequency-Resolved Optical Gating is a technique widely used for the measurement of the time-dependent intensity and phase of an ultrashort laser pulse, without prior assumptions on the form of the pulse. FROG simply relies on the measurement of a spectrogram, obtained by "gating" the target electric field with a variable-delay gate function and measuring a spectrum for each delay. The idea is to extract the information on "which" frequencies are present and "when" they appear. After measuring the spectrogram, an iterative algorithm is applied and the pulse is fully reconstructed by few iterations [**25, 26**]. This complicated approach is required since no direct measurement of the pulse features is possible. Indeed, there is no photodetector fast enough to

track the temporal evolution of the electric field in the pulse, that oscillates at a frequency of more than 374 THz, but it is neither possible to do a measurement in the spectral domain, since no information about the phase can be extracted by a standard spectrometer, as we always measure intensity spectra. The power of FROG is that it works in the frequency domain but combines many spectra to extract information on the phase, thus allowing for a complete reconstruction of the pulse. Let $E(t)$ be the electric field pulse and $g(t-\tau)$ be a viable-delay gate function. The experimental spectrogram, measured as the spectrum of the gated field, is defined as

$$S(\omega,\tau) = \left| \int_{-\infty}^{+\infty} E_{sig}(t,\tau) e^{-i\omega t} dt \right|^2 \tag{3.1}$$

where

$$E_{sig}(t,\tau) = E(t)g(t-\tau) \tag{3.2}$$

is the gated field. As we said, an iterative procedure, explained in the figure 3.1, is needed for the reconstruction. Such procedure tries to retrieve the electric field that satisfies two conditions at the same time, represented by Eqs. 3.1 (match to the FROG trace, called data constraint) and 3.2 (the so-called physical form constraint), and goes through the following steps:

(0) Assume a tentative, initial guess for the electric field to be reconstructed. We call this function $E(t)$;

(1) Multiply by the variable-delay gate, $g(t-\tau)$, to obtain the gated electric field $E_{sig}(t,\tau) = E(t)g(t-\tau)$. Such function represents a small portion of the electric field, around the time instant $t = \tau$. The choice of a suitable gain function in the experiment is crucial: indeed, having a gate that is too narrow, will enhance the temporal resolution of the measurement but will degrade, at the same time, the spectral resolution, whereas a gate with a long duration will improve the spectral resolution and worsen the temporal one. A suitable trade-off is needed;

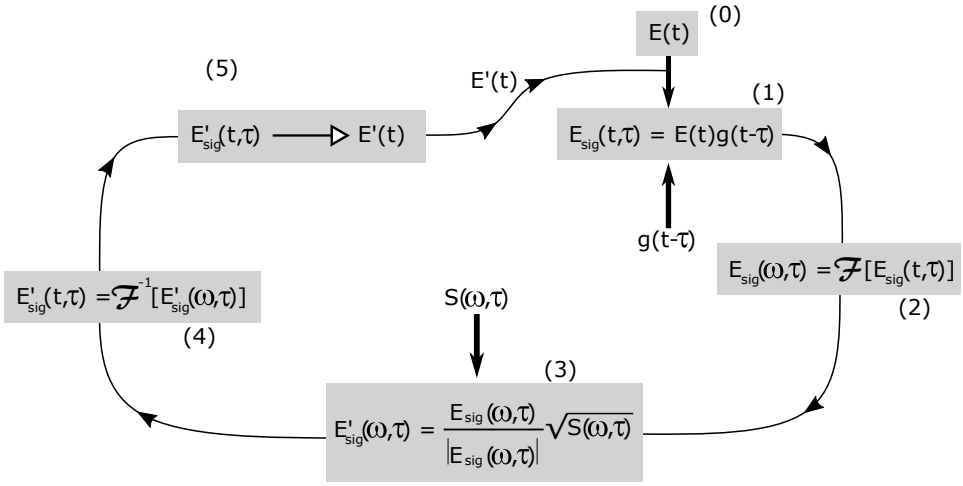


FIGURE 3.1. Schematic representation of the iterative procedure for pulse reconstruction using FROG. Starting from an initial guess for the electric field (0) and defining a suitable gate function, the gated signal can be computed. Applying a Fourier transform, the reconstructed spectrogram is computed (2). The magnitude of the spectrogram is replaced with the experimental value (3). An inverse Fourier transform is applied to retrieve the corrected gated signal (4). Using a suitable procedure, the corrected electric field can be computed (5) and then used for another cycle.

(2) Compute the Fourier transform of the gated signal, thus obtaining the reconstructed spectrogram $E_{sig}(\omega, \tau)$.

(3) Compare now the reconstructed spectrogram to the experimental information. In particular, as we know, the square root of the experimental spectrogram is the modulus of the Fourier transform of the experimental gated field (see Eq. 3.1). The correction we can set, in order to drive the iterative procedure towards convergence, is to modify the reconstructed spectrogram and force it to have the right modulus. Therefore, we

obtain the corrected spectrogram $E'_{sig}(t,\tau)$ by simply replacing the magnitude of the spectrogram at the previous step and preserving the same phase. It is computed as

$$E'_{sig}(\omega,\tau) = \frac{E_{sig}(\omega,\tau)}{|E_{sig}(\omega,\tau)|}\sqrt{S(\omega,\tau)} \tag{3.3}$$

This is to satisfy the data constraint;

(4) Compute now the inverse Fourier transform and retrieve the new, corrected gated signal ($E'_{sig}(t,\tau)$);

(5) Extract the electric field from the gated signal. To do this, many mathematical procedures are available. In any case, they are all designed to satisfy the physical form constraint.
Once the corrected electric field is obtained, another cycle can be run, starting from step (1), where now the initial guess field is replaced by the corrected field.

The iterative procedure we have outlined is a general description of the method used for the reconstruction and it is meant only to explain what is the underlying idea of the method. Indeed, very sophisticated approaches have been developed, like the Generalized Projections (GP) method [**26**], for the electric field extraction at step (5), providing a robust procedure and almost certain and quick convergence even in the case of very complicated field structures. In particular, the methods that are actually used nowadays rely on the definition of a cost function (error function) to be minimized, in order to match the physical form constraint, despite the satisfaction of the data constraint is always achieved by replacing the magnitude of the reconstructed trace, as we did. Also, many different experimental implementations of FROG are possible. The difference among them is in how the gate function is obtained. Here we briefly discuss the most popular geometries [**25**]:

- Polarization-gated FROG (PG-FROG): here the gate is obtained by focusing the pulse and its delayed replica, polarized at 45°, into a $\chi^{(3)}$ crystal. The replica rotates the polarization of the pulse by means of induced birefringence, depending on

the intensity of the replica. Then a polarizer is placed and only the rotated field is let through. As a result of this, the gate is the intensity profile of the replica field;

- Self-diffraction FROG (SD-FROG): two beams, one the replica of the other, even with the same polarization, are overlapped in a $\chi^{(3)}$ crystal, generating by non-linear effects a refractive index grating. Both pulses are diffracted into new beams and one of them can be used for detection;
- Transient-grating FROG (TG-FROG): three pulses are used in this configuration, starting from a single pulse that is then split twice. In particular, two pulses are focused in a crystal, producing a diffraction grating, like in the SD-FROG configuration. Then, a third pulse is diffracted and then detected;
- Second-harmonic generation FROG (SHG-FROG): the most popular FROG geometry, it is base on a $\chi^{(2)}$ crystal, where the pulse and its delayed replica are focused. Here, the gate is the pulse electric field itself, producing a trace that is symmetrical with respect to the zero of the delay axis.

Of course, many other approaches are available. For the characterization of the IR pulses in our setup we used the SHG-FROG. A representation of the home-made setup we used for the IR pulse reconstruction is shown in figure 3.2. Here, to obtain the gate and the pulse, we extracted a part of the beam using a wedge, right before the generation chamber in order to have a reliable reconstruction, that we first split by a 50:50 beam splitter; then the two replicas are delayed one with respect to the other by means of a retro-reflector mounted on a motorized slide. After that, both beams are focused onto a thin $\chi^{(2)}$ crystal (we used a BBO crystal) where SHG occurs. At the output of the crystal a $2\omega$ field is generated, being $\omega$ the fundamental frequency of the pulse, with the form

$$E_{SH}(t) \propto E(t) \cdot E(t-\tau) \tag{3.4}$$

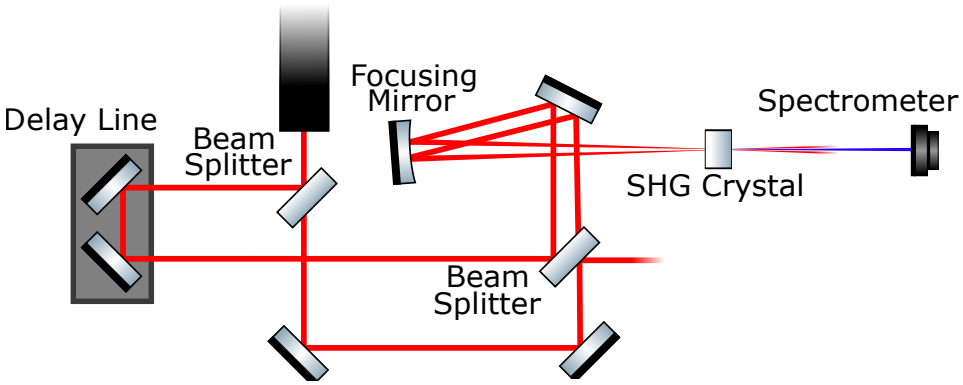


FIGURE 3.2. Schematic representation of a SHG FROG setup: the 50:50 beam splitter creates the replica of the pulse, that is delayed by a retro-reflector. The two pulses are then overlapped and focused in the SHG crystal. Depending on the phase matching condition, a beam at $2\omega$ is generated along another direction. By recording a spectrum at each delay, the spectrogram is recorded.

Then at each delay a spectrum is measured, corresponding to the spectrogram

$$I(\omega,\tau) \propto \left| \int_{+\infty}^{-\infty} E(t) \cdot E(t-\tau) e^{-i\omega t} dt \right|^2 \tag{3.5}$$

and using a standard FROG algorithm the pulse can be reconstructed. We have measured the FROG trace and attempted a reconstruction in two different cases: with a Ne-filled hollow-core fiber, used to compress the pulses, and with an empty fiber.

The case of longer, uncompressed pulses is presented hereafter. Figure 3.3 shows the FROG trace in this case where, as we discussed, the pulse compression system is unused. It has a temporal extension that ranges for about 40 fs, and a spectral range of 20-30 nm. As expected since we use an SHG-FROG, it is symmetrical with respect to the zero delay and, in addition, it has some structures for extreme delays, showing that the pulse has some spectral components far from

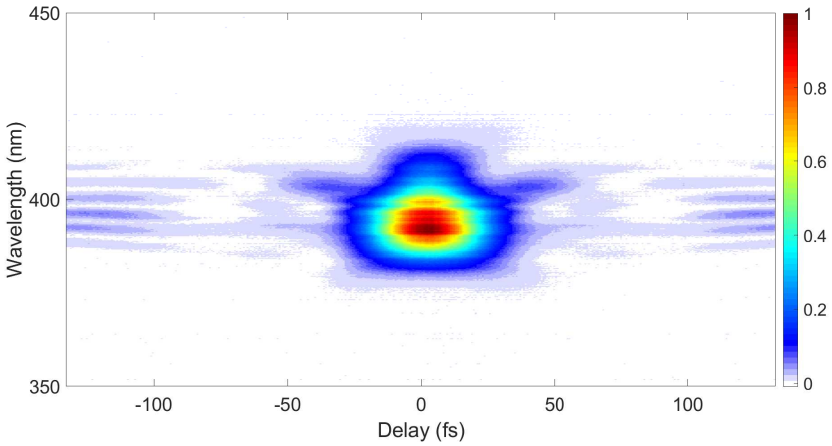


FIGURE 3.3. FROG trace for longer IR pulses, measured with empty hollow-core fiber. As expected, the trace is symmetrical. Also, some spectral components at extreme delays are present.

the peak, resulting in an after or pre-pulse. The result of the reconstruction is exhibited in figure 3.4. We obtain a pulse, quite near to its transform-limited (the TL duration is 19.1 fs), with a duration FWHM of 20.4 fs.

After characterizing the longer pulses, we filled the fiber with 1.5 bar of Ne and did the FROG for compressed, shorter pulses. The result in this case, more of interest for our experimental purposes, is presented hereafter. Figure 3.5 illustrates the experimental FROG trace in this case. The trace extends for roughly 20 fs, quite shorter with respect to the case of longer pulses, and also it occupies a broader spectral region, from 380 to 420 nm. Even in this case the trace has some structures for extreme delays, that however have a smaller temporal extension with respect to the short pulses. The result of the reconstruction is shown in figure 3.6. As we can see, the actual pulse is almost transform limited (TL) and has a time duration of only 11.8 fs, enough for producing short XUV pulse trains, as we will see in section 2.

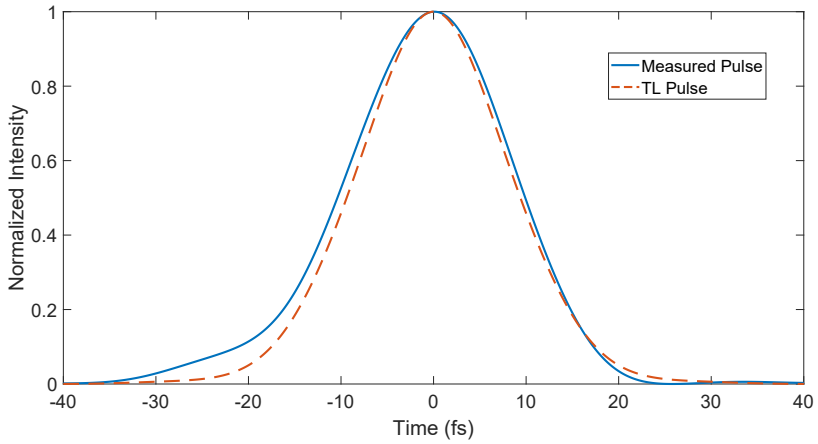


FIGURE 3.4. Reconstruction of the IR pulse: the solid line shows the reconstructed IR pulse, compared to the corresponding transform-limited (dashed line). The two are slightly different, with a duration FWHM of 20.4 fs against the shorter TL pulse (19.1 fs).

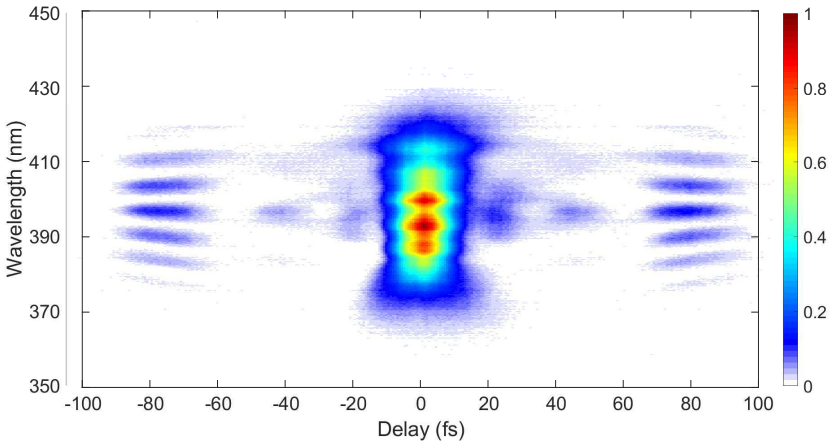


FIGURE 3.5. FROG trace for short pulses, compressed by means of 1.5 bar of Ne in the hollow-core fiber, showing the spectrum for each delay. The trace is symmetrical with respect to the zero delay, as expected in the SHG FROG geometry and has some structures for extreme delays.

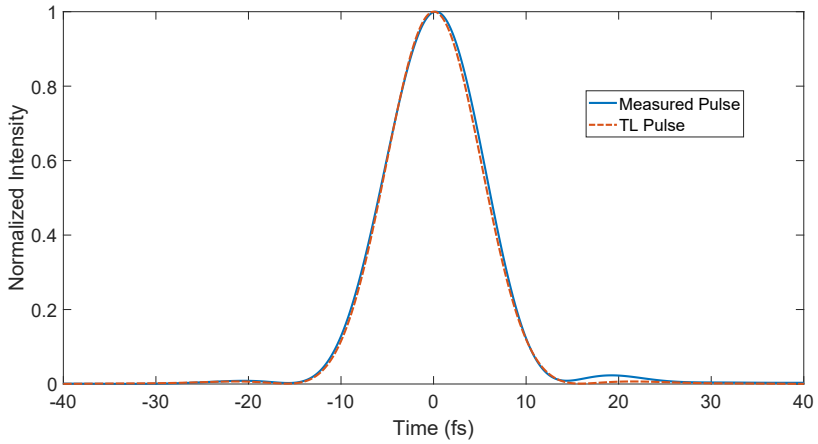


FIGURE 3.6. Reconstruction of the IR pulse: the solid line shows the reconstructed IR pulse, compared to the corresponding transform-limited (dashed line). The two are almost identical, with a duration of less than 12 fs.

## 2. RABBITT

Reconstruction of attosecond beating by interference of two-photon transition (RABBITT) is a technique developed for measuring the average duration of a pulse in an attosecond train [**27**], based on the assumption that only monochromatic fields are involved. It relies on the measurement of photoelectron spectra from a noble gas, called a RABBITT trace, produced in a pump-and-probe scheme where an attosecond pulse train (APT) initiates the electron dynamics by triggering the ionization, overlapped to a dressing IR pulse. Since in the HHG scheme only odd harmonics are generated, the photoelectrons are emitted with an energy corresponding to an odd multiple of the IR energy [**28, 29**]. In particular, accounting for the ionization potential ($I_p$) of the gas atoms, the electron kinetic energies can be written in the form;

$$E_e = (2q+1)\hbar\omega_{IR} - I_p \tag{3.6}$$

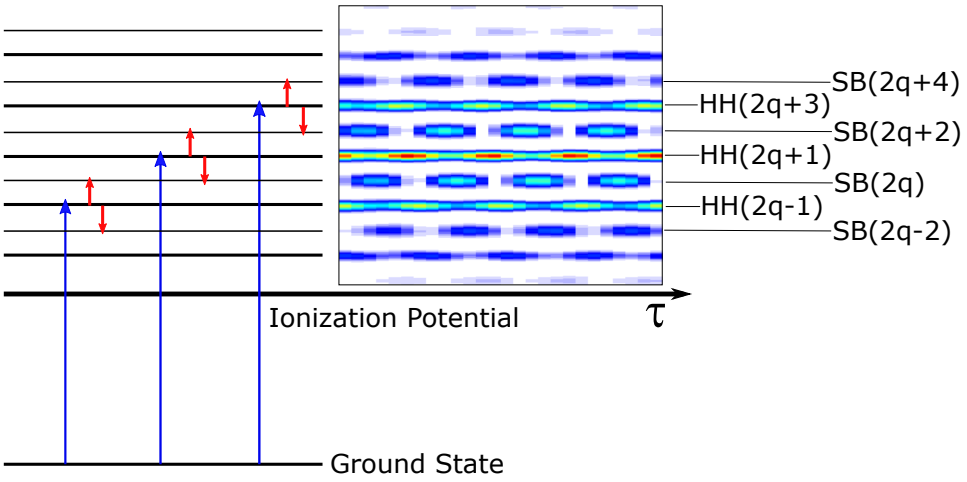


FIGURE 3.7. RABBITT trace: one XUV photon is absorbed (blue arrows) and one electron is emitted with a kinetic energy related to an odd multiple of the photon energy (minus the ionization potential). The photoelectron then interacts with one IR photon and either absorbs or emits it (red arrows). The electron has now a kinetic energy, corresponding to an even multiple of the IR photon energy, between two subsequent harmonics. This, populates the so-called sidebands (SB), while depleting the harmonics (HH). At different delays ($\tau$) the sidebands and the harmonics oscillate.

where $\omega_{IR}$ is the IR angular frequency and $q$ and integer. After the electrons are extracted from the atoms, they can interact with one or more IR photons that produces additional transitions in the continuum. In particular, if we consider interactions with single IR photons, one of them can be absorbed or emitted by a photoelectron. Therefore, electron with an energy corresponding to an even multiple of the IR energy is produced. The signal associated to such energies in the RABBITT trace is referred to as the sideband. This process is shown in figure 3.7. With low intensity of the IR field, where the problem can be treated via a second-order perturbation theory, each harmonic

has only one sideband per side, such that the signal of each sideband is determined by the contribution of only two neighboring harmonics, via two different quantum paths. As a result of the interference of the two different electron paths to the same final state, the sideband oscillates as the delay $\tau$ between the IR and XUV fields is scanned. Using Fermi's golden rule in the second-order perturbation framework and assuming monochromatic IR field and XUV harmonics, the intensity of the sideband can be written as:

$$I_{2q}(\tau) \propto 1 + cos(2\omega_{IR}\tau - \Phi_{SB}) \tag{3.7}$$

where

$$\Phi_{SB} = \Delta\theta_{HH} + \Delta\theta_{Atom} - \theta_{IR} \tag{3.8}$$

In Eq. 3.8, $\theta_{IR}$ is the IR phase, related to the choice of the zero delay and therefore common to every sideband, $\Delta\theta_{Atom}$ is a term related to the photo-ionization process and $\Delta\theta_{HH}$ is the phase difference of the two adjacent harmonics, related to the chirp of the XUV pulses. In particular, such term is directly connected to the emission time of the considered harmonics, and it is the information we need for the reconstruction.

In general, the determination of the harmonic phase difference is not straightforward, because of the presence of the atomic phase $\Delta\theta_{Atom}$. This term is mainly determined by two independent contributions: a scattering term (called the Wigner phase), related to the delay introduced by the fact that the electron does not propagate in the free space but experiences the potential of the parent ion, and the continuum-continuum contribution, due to the absorption/emission of the IR photon. Such terms are typically much smaller than the harmonic phase difference and therefore can be neglected, at least for pulse characterization, despite their value could be precisely computed to be used for fine corrections. This said, the phase of each harmonic can be easily determined by concatenating the phase differences of the subsequent

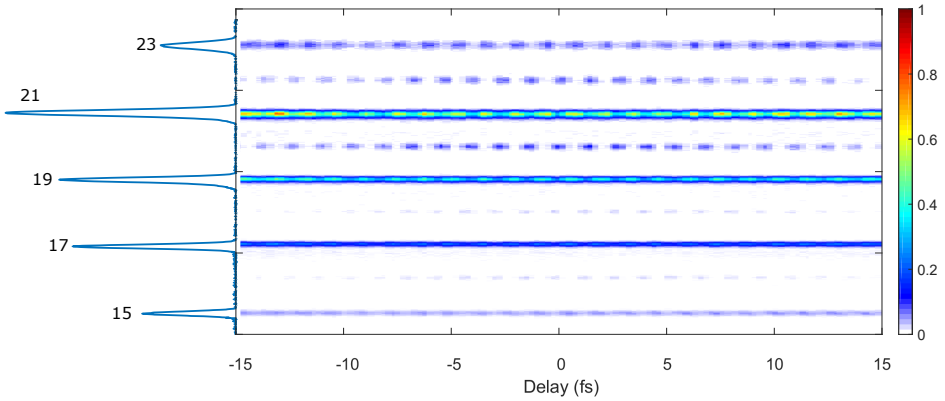


FIGURE 3.8. Experimental RABBITT trace, obtained in the ToF using neon, compared to the measured photon spectrum, where the harmonic order is also shown. Such trace is characterized by four different sidebands, appearing halfway between the harmonics, that oscillate in counterphase with respect to them.

harmonics, as extracted from the sidebands. Combining this information to the one we can extract from a spectrum, the XUV burst can be reconstructed.

Figure 3.8 shows the experimental RABBITT trace we used for the reconstruction, in the case of empty hollow-core fiber. The harmonics are generated in Ar, whereas the trace is measured using Ne in the ToF spectrometer. The extraction of the phase out of the experimental trace can be performed in several different ways, involving either the Fourier transform or a fit using a known model. The simplest approach consists in identifying an interval along the electron kinetic energy axis around the sideband and integrating the signal over it. It is referred to as the spectral integration method. The great advantage of this approach is that the spectral integration behaves like and averaging filter, thus reducing the noise and enhancing the signal-to-noise (SNR) ratio. In many cases, however, this approach does not produce accurate results, for examples if two different sidebands are spectrally overlapped

[**30**]. This happens when the energy level structure of the employed gas is complex, for example when using molecules in the ToF spectrometer. In such cases, other methods should be used. We decided to apply the spectral integration method, since we used Ne as the auxiliary gas in the time of flight spectrometer. It has indeed a very simple energy level structure, that with our energy range is not producing any appreciable spectral overlap. In particular, the maximum energy we achieved in all the experiments we carried out is about 45 eV (see figure 3.19, representing the spectrum of the XUV APT with filled hollow-core fiber). In this case, we can only extract electrons from state 2p (binding energy of 21.6 eV) but not from the state 2s right below (binding energy of almost 50 eV) [**31**]. This implies that the photoelectron spectrum directly replicates the photon spectrum, since electrons at a particular kinetic energy can only be produced by a single harmonic. Eventually, the sidebands where extracted using this simple approach. In figure 3.9 sideband 20 is shown, together with the neighboring harmonic 19, both extracted by means of this method. As expected from the theory, the sideband and the harmonic oscillate at a frequency that is the double of the optical one and they are in counterphase: the population of the sideband determined the depletion of the harmonic and viceversa. Figure 3.10 shows the Fourier transform of the sideband signal, represented by the blue line. It appears very close to the value we expect from theory, marked by the red line and corresponding to about 0.748 PHz. In the same figure we also display the band-pass function (yellow line), that is used to filter the sideband oscillation, in order to clean it from additional contribution, non-related to the phenomenon we rely on for the pulse characterization. Figure 3.11 illustrates the same signal in figure 3.9, filtered at around twice the IR frequency.
Once the sidebands have been extracted the phase of the oscillation has to be obtained. We decided to extract the phase by fitting the filtered sideband with the following function [**32**]:

$$SB(\tau) = Ae^{\left(\frac{\tau-\tau_0}{c}\right)^2} cos(\omega\tau - \Phi_{SB}) + b \tag{3.9}$$

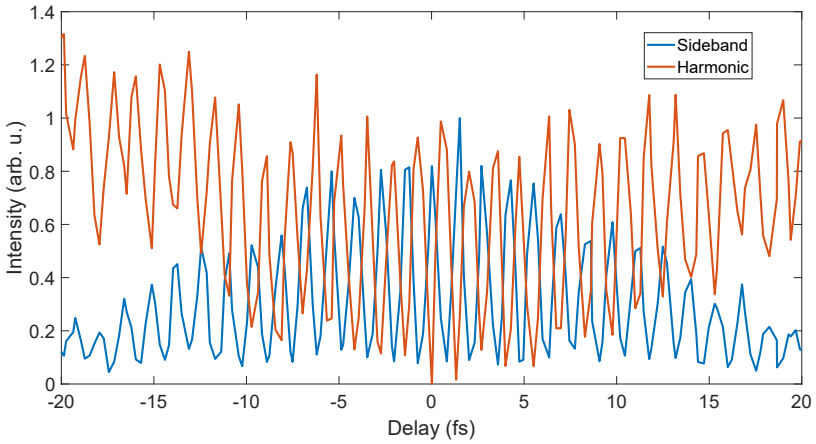


FIGURE 3.9. Rough intensity profile of the sideband/harmonic signal in the RABBITT trace, before filtering them around twice the IR frequency. The blue curve is the experimental sideband 20 and the red line shows the neighboring harmonic 19, both extracted by integrating the signal inside an interval along the electron kinetic energy axis. As expected, both the sideband and the harmonic oscillate with a period that is half of the IR optical cycle. Moreover, they are in counter-phase: when the sideband is populated, the harmonic is depleted and viceversa.

where A is the amplitude of the oscillation, $b$ an offset parameter, $c$ is related to the width of the envelope, connected to the crosscorrelation of the envelope of the IR and XUV fields that produce the trace, $\omega$ is the angular frequency of the oscillation, that has to be equal to twice the IR frequency, $\tau_0$ the zero of the delay axis and finally $\Phi_{SB}$ the phase of the oscillation, the parameter of interest in the reconstruction. Among all those terms, all but $\tau_0$ where fitting parameters, whereas $\tau_0$, as the reference of the delay axis, was previously calibrated. In particular, we first ran the fitting with a non-centered delay axis, for each sideband, and found the estimated zero delay. Then, computed the actual delay

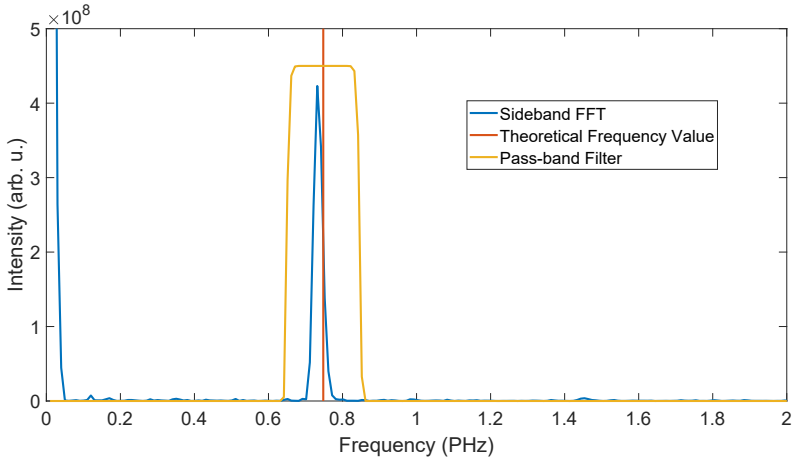


FIGURE 3.10. The Fourier transform of the sideband signal is represented by the blue line. The theoretical value of the oscillation frequency (about 0.748 PHz) is represented by the red vertical line and appear very close to the experimental value. We also show in yellow the function we used to filter the sideband and remove unwanted components, like the huge low-frequency part.

as the average of the values of $\tau_0$ for every sideband, in order to define a single common reference axis. Once the proper reference is set, we ran the fitting procedure again to obtain the phase terms of the sideband oscillations. Eventually, we left $\omega$ as a free parameter to check the actual frequency of the sideband. The result was in any case basically equal to the theoretical value, corresponding to $4.7 \cdot 10^{15}$ rad/s. Figure 3.12 exhibits the result of the fit for the sideband 20. The result is very positive, as the fitting curve, in red, follows very well the experimental data (blue circles). The extracted harmonic phase difference $\Delta\theta_{HH}$ for each harmonic, assuming it equal to the sidebands phases $\Phi_{SB}$, is shown in figure 3.13.

Once the harmonic phase differences are extracted and the harmonic phases are obtained, by concatenating the subsequent values we have

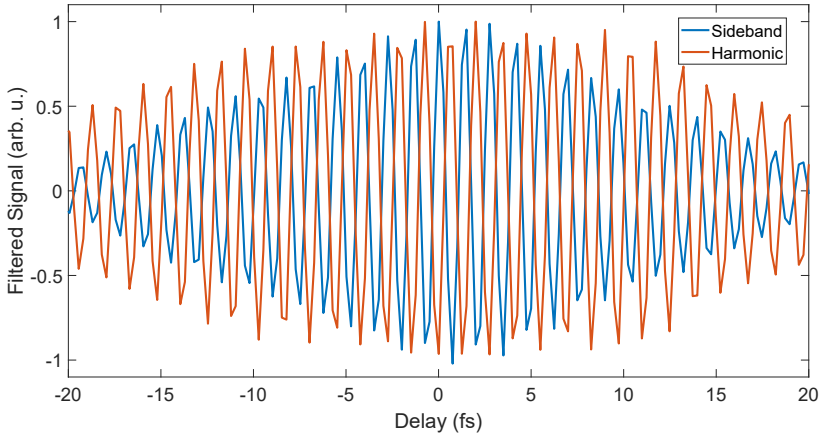


FIGURE 3.11. Sideband oscillation, filtered around the correct frequency (twice the IR one) by means of a Fourier transform. The signal shows the same features as in the non-filtered signal and compares better to the fitting model we use for phase extraction.

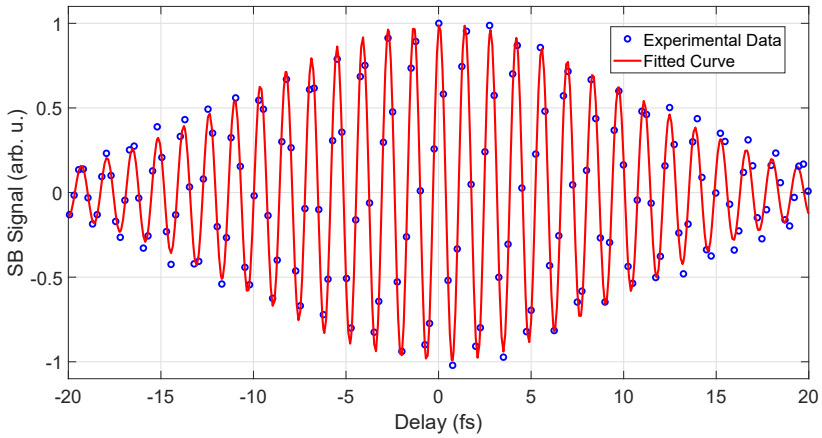


FIGURE 3.12. The fit of the filtered sideband 20 is represented by the red line. As we can see, it compares very well to the experimental data. The corresponding coefficient of determination is $R^2 = 0.97$.

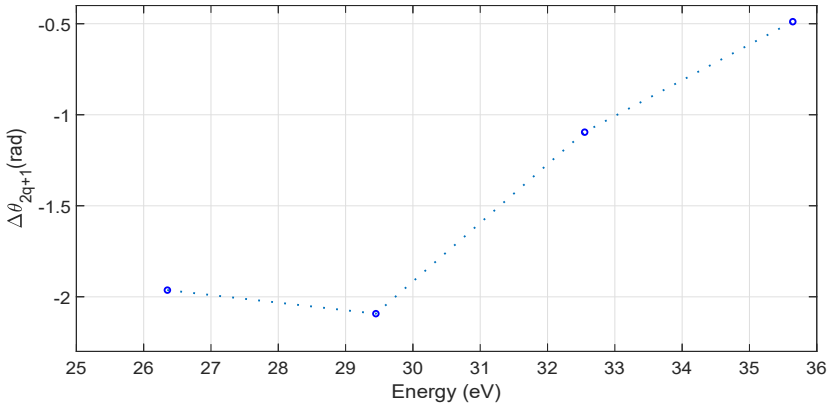


FIGURE 3.13. Harmonic phase difference extracted from the oscillations of the sidebands in the RABBITT trace.

extracted, the reconstruction can be carried out. As we already discussed, the method is designed to reconstruct the average pulse in train, since the main assumption is that the involved IR and harmonics are monochromatic. As a result, the XUV intensity profile can be simply reconstructed as follows:

$$I(t) = \left| \sum_{q \ odd} A_q e^{i(\omega_q t - \phi_q)} \right|^2 \tag{3.10}$$

where $A_q$ is the amplitude of the $q^{th}$ harmonic, extracted from the photon or photoelectron spectra (we used the directly measured photon spectrum), $\omega_q = q\omega_{IR}$ is the harmonic angular frequency and $\phi_q$ is the harmonic phase, computed as

$$\phi_q = \sum_{i=q_r}^{q} \Delta\theta_i \tag{3.11}$$

where the $q_r^{th}$ harmonic is the reference, such that $\phi_{q_r} = 0$ by definition and $\Delta\theta_i$ is the harmonic phase difference we measured. Notice that by computing the XUV field according to this approach is equivalent to considering the XUV spectrum as made of a comb of $\delta$-functions. Therefore, the reconstructed train is an infinite set of identical pulses.

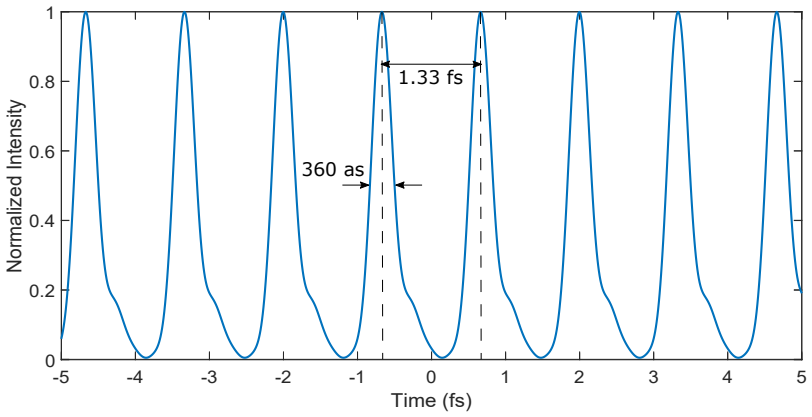


FIGURE 3.14. APT made of an infinite set of pulses, correctly separated by 1.33 fs. Each pulse has a duration of 360 as and shows a small shoulder for longer times.

In the following pages, we will present the reconstruction of the XUV burst, that we obtained in two different situations. In particular, like in section 1, in order to test the setup, we tried to measure the temporal characteristics of either short or long pulses, corresponding to an empty fiber or filled with neon, as we discussed. We first present the case of long pulses, obtained using an empty hollow-core fiber, as RABBITT best applies to this case.

By using RABBITT in its basic form, we reconstructed a train as a set of identical pulses, separated by half of the period of the IR field (1.33 fs), with a duration FWHM of 360 as and a slight shoulder after it, as illustrated in figure 3.14.

It is clear that the main limitation of this method is that it only allows for an estimation of the duration of the mean XUV pulse, but gives no information on the duration of the pulse train. Of course, since the XUV burst is generated by an IR pulse with finite duration, we expect the XUV burst to be finite as well. In this framework, this limitation is related to the assumption that the fields are monochromatic and therefore the pulse train is obtained as the superposition of harmonics of infinite duration. From this point of view, it should be possible to

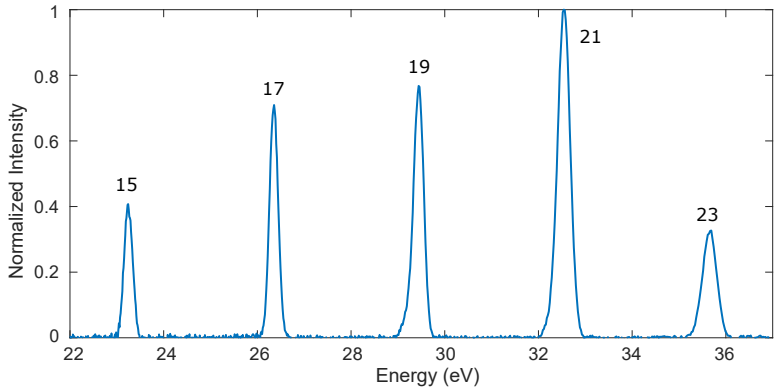


FIGURE 3.15. XUV photon spectrum generated in Ar, with the harmonics that are labeled with their order. In particular, harmonics from 15, with about 23 eV, to 23, with about 36 eV, are generated.

give an estimation of the pulse train duration by accounting for the non-zero bandwidth of the harmonics in the spectrum (figure 3.15). Since every harmonic has a different width, we decided to define a sort of average bandwidth, also keeping in account the amplitude of each peak as a weight. Let $\sigma_q$ be the spectral width (variance) of the $q^{th}$ harmonic and $A_q$ the corresponding magnitude, both measured in the amplitude spectrum. We can define the average harmonic bandwidth as follows:

$$\sigma = \frac{\sum_q A_q \sigma_q}{\sum_q A_q} \tag{3.12}$$

Then, if we assume that this value is the variance of a Gaussian function representing the average shape of the harmonics in the frequency domain, in the form

$$G(f) = exp\left(-\frac{f^2}{2\sigma^2}\right) \tag{3.13}$$

we can assume the temporal profile of the envelope to be the corresponding Fourier transform:

$$g(t) = exp\left(-2\pi^2\sigma^2 t^2\right) \tag{3.14}$$

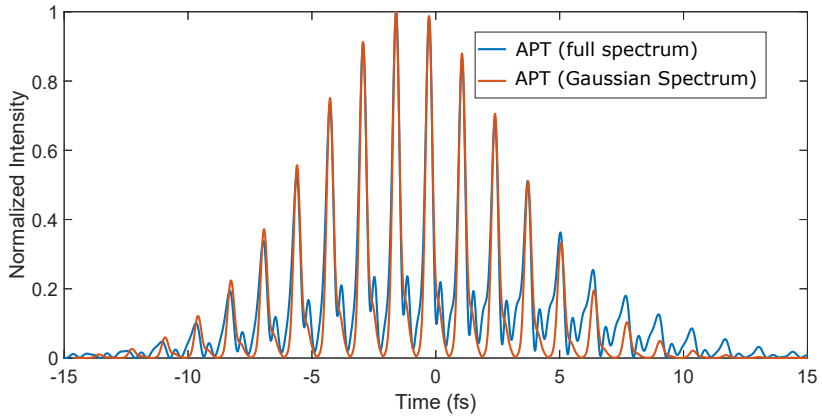


FIGURE 3.16. Experimental reconstruction of the XUV pulse train by inverse-transforming the full experimental XUV photon spectrum (blue line), compared to the reconstruction obtained by estimating the duration of the envelope assuming Gaussian harmonics. The finite duration of the train envelope amounts to almost 10 fs.

As a result of this, we can estimate the shape of the train by means of the following expression:

$$I(t) = \left| \left( \sum_{q \ \ odd} A_q e^{i(\omega_q t - \phi_q)} \right) e^{\left(-2\pi^2\sigma^2 t^2\right)} \right|^2 \tag{3.15}$$

where the electric field in Eq. 3.10 is tailored using the Gaussian in Eq. 3.14. With such approach, we were able to estimate the duration of the pulse train. In particular, we found out that the train contains about ten main pulses and has a duration of about 9.8 fs. The red line in figure 3.16 illustrates the corresponding intensity profile.

As we just observed, this method is very useful to give an estimation of the duration of the pulse train, but relies on the simplified assumption that the harmonic spectrum is a comb of Gaussian functions (the bandwidth measurement was obtained by fitting the experimental data with such a model). This could lead to error in the reconstruction since

the spectral features of the APT are modified. In order to overcome such possible issue, we designed an alternative approach, consisting on simply elaborating the experimental XUV spectrum and finding the temporal profile of the pulse train by applying an inverse Fourier transform to it. The advantage of this approach is that, since we do not change the shape of the spectrum, any possible spectral feature of the pulse train is preserved. However, before carrying out any reconstruction, the spectrum has to be properly modified, to account for the spectral phase we extracted from the RABBITT trace. As the phase function we measured is discrete, only made by values defined at each harmonic position, and since there is no possibility to extract the full phase information by means of the simple approach we implemented, further hypotheses are needed. In particular, we assumed that the spectral phase is flat over each harmonic bandwidth and equal to the value we measured. Then, we simply multiplied the experimental amplitude spectrum by this phase function and computed the inverse Fourier transform. The resulting complex spectrum is shown in figure 3.17 where the blue line represents the experimental intensity spectrum of the APT, whereas the red line shows the phase function we obtained by concatenating the experimental phase differences we measured. Also, in order to avoid discontinuities, we smoothed the phase function before the multiplication. The result of the inverse Fourier tranform is exhibited in figure 3.16 (blue line), showing basically the same features we obtained with the reconstruction by Eq. 3.15 (red line). An important difference is that now we can better discriminate the delayed shoulder that appears as a well defined afterpulse, probably because of the fine structure of the XUV spectrum we are keeping into account.

Once the reconstruction of the longer XUV APT has given such positive results, we tried to apply the same procedure in the case of shorter pulses obtained, as stated many times, using 1.5 bar of Ne in the hollow-core fiber. It has to be noticed that, as already discussed, RABBITT

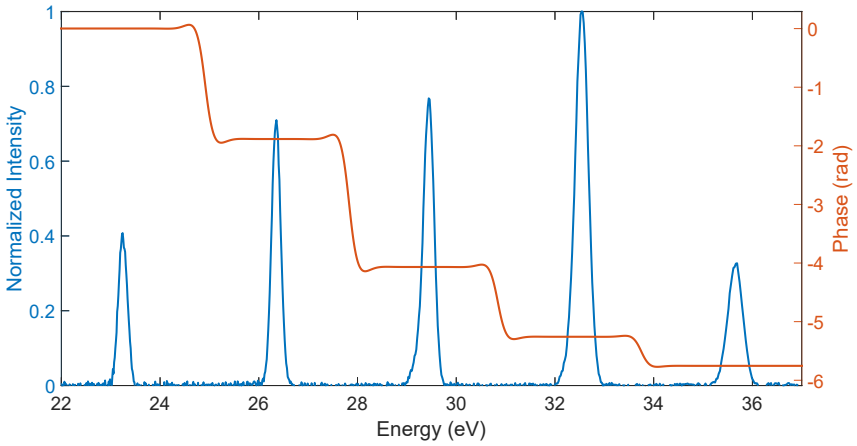


FIGURE 3.17. Reconstructed complex spectrum, represented in terms of the experimental spectral intensity (blue line) and a reconstructed phase function (red line). The phase function is obtained as an elaboration of the experimental phase differences measured by RABBITT. In particular, we assumed the phase to be flat over each harmonic bandwidth and built the overall phase accordingly. Then, to avoid discontinuities, we smoothed the function.

is not designed to work with very short pulses (remember that it is derived considering monochromatic fields). For this reason, we do not expect a very precise reconstruction in the case we are presenting hereafter.

Figure 3.18 shows the corresponding RABBITT trace in this case, directly compared to the photon spectrum. As expected, the sidebands and the harmonics are quite broader, if we compare to the case in figure 3.8, and also more of them are showing up, as a result of the increase in the cutoff frequency. The photon spectrum, illustrated in details in figure 3.19 shows of course the same features, with borades peaks and higher energies, considering that the maximum we achieve is 45 eV, much larger than the 36 eV we have obtained in the case of

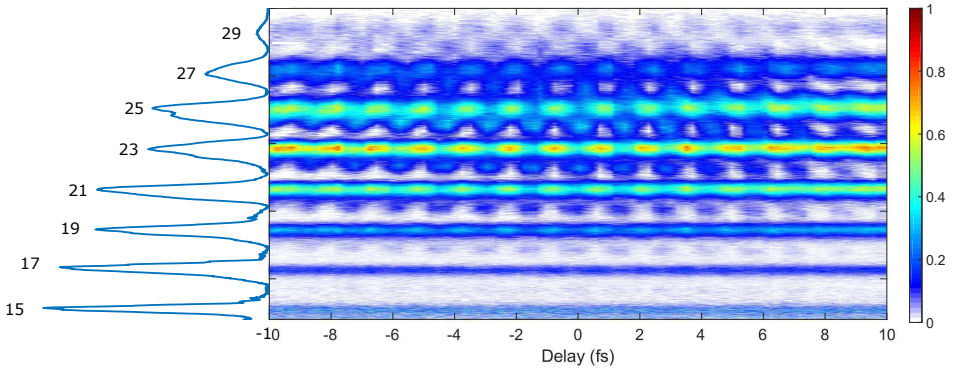


FIGURE 3.18. RABBITT trace for short pulses, generated in Ar, measured using Ne in the ToF. It is compared to the photon spectrum, directly measured on the spectrometer. In this case, the hollow-core fiber is filled with 1.5 bar of Ne. As a result of this, both the harmonics and the sidebands are broader and also higher orders are showing up, revealing that the cutoff frequency has increased.

figure 3.15. Upon applying the same approach we have discussed in details in the case of long pulses, we were able to extract the harmonic phase differences out of the RABBITT trace in figure 3.18, and the result is illustrated in figure 3.20. The blue circles represent the values extracted from the sidebands oscillations with the fitting procedure we have discussed and range from 1.2 to 2.6 rad. Using such values and the information contained in the photon spectrum, we were able to reconstruct the APT exhibited in figure 3.21. As expected, the identical pulses are separated by half of the period of the IR field and have a duration FWHM of only 212 as. Such pulses are also characterized by a small afterpulse, with a peak intensity of 17% of the one of the main pulse, that probably correspond to the small shoulder we have observed in the case of longer pulses (see figure 3.14), but now compressed as

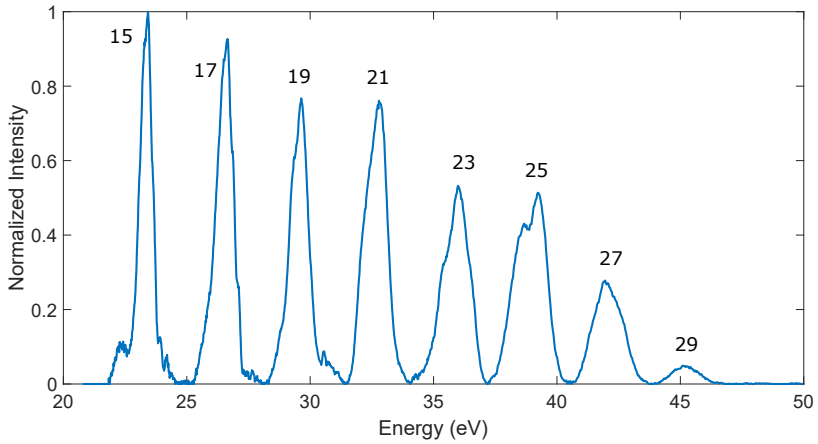


FIGURE 3.19. XUV photon spectrum generated in argon, consisting of a series of peaks, spaced by roughly 3 eV (corresponding to two IR photons), ranging from harmonic 15 at more or less 23 eV to harmonic 29, at 45 eV.

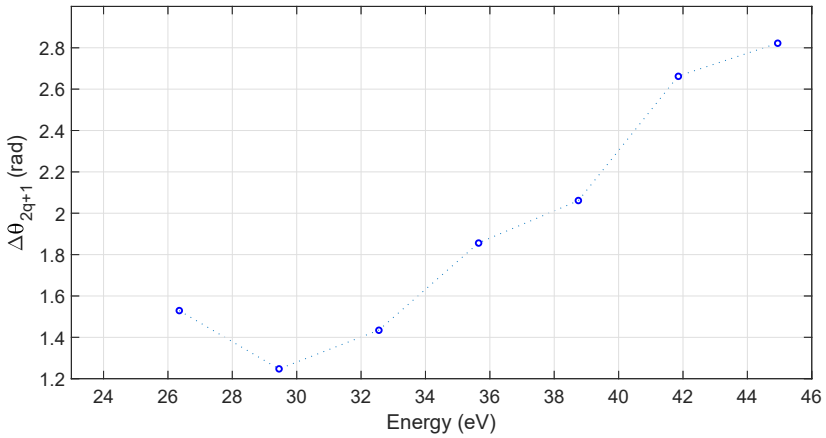


FIGURE 3.20. Harmonics phase difference, measured from the sidebands oscillations, in the case of short pulses.

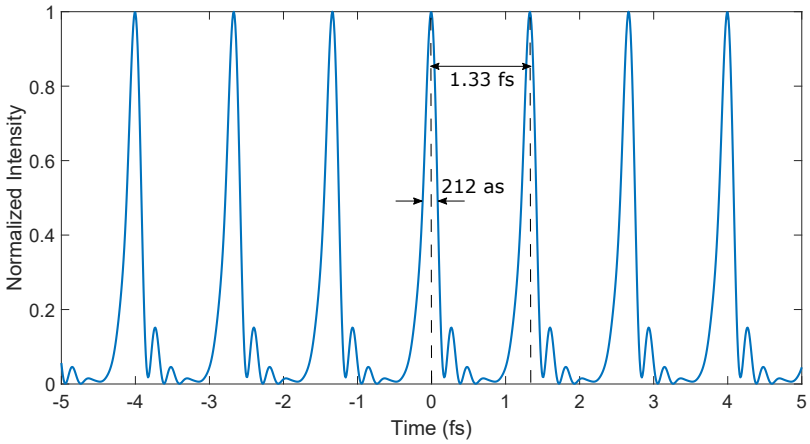


FIGURE 3.21. Attosecond pulse train reconstructed with the standard RABBITT. It consists of an infinite number of identical pulses, separated by 1.33 fs, half of the IR period, with a duration of 212 as FWHM. Also, a small afterpulse is shown, with a peak intensity of 17% of the one of the main pulse.

well. Finally, we have used the two methods we have discussed to estimate the duration of the APT, accounting for the non-zero bandwidth of the harmonics. The result is shown in figure 3.22. Here we see, for both methods, an APT made of three main pulses and a duration of only 3.1 fs. Such value is really too optimistic and it is probably an underestimation of the actual duration. Indeed, as already discussed, any attempt to retrieve information on the actual structure of the APT using RABBITT means pushing the methodology beyond its natural limit, even more so if the pulse train is so short. If our aim is to obtain a precise reconstruction of the XUV field, other methods must be applied.

Besides giving us general information about the temporal features of the XUV radiation we can generate, the results we have just discussed tell us another important property of our experimental setup: its stability. In fact, since we are able to perform RABBITT measurements,

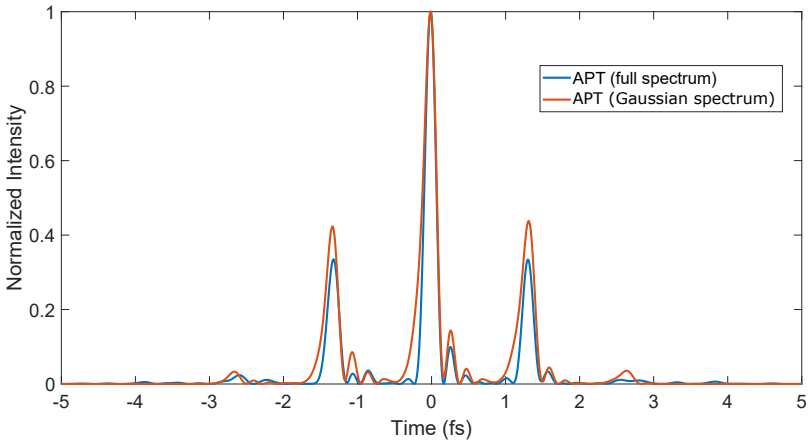


FIGURE 3.22. Experimental reconstruction of the XUV pulse train by inverse-transforming the full experimental XUV photon spectrum (blue line), compared to the reconstruction obtained by estimating the duration of the envelope assuming Gaussian harmonics. In both cases, the train duration amounts to 3.1 fs.

we can also be sure that the interferometer we have built is stable enough and suitable for measurements in the attosecond time domain.

## 3. FROG CRAB

An efficient technique we can use for the full reconstruction of the XUV field out of a trace obtained by means of photoionization of atoms, like in the RABBITT, is the frequency-resolved optical gating for complete reconstruction of attosecond bursts (FROG-CRAB, hereafter called CRAB) [**24**]. The power of this technique is that it allows to transpose the efficient tools developed in the mature field of ultrafast optics to the attosecond field. Indeed, CRAB is an extension of FROG (discussed in Section 1), as it is based on the same idea for the field reconstruction. In particular, FROG relies on the measurement of a spectrogram, obtained by means of a gate function (Eqs. 3.1 and 3.2). The basic approach requires an amplitude gate function but

in principle the technique can be successfully applied even with a pure phase gate. In this view, we will observe that the photoelectron trace is perfectly equivalent to the FROG spectrogram and that it can be used to fully reconstruct the fields.

Consider atoms with an ionization potential $Ip$, ionized by an XUV field $\mathbf{E}_X(t)$ in the presence of an IR field $\mathbf{E}_{IR}(t) = -\partial\mathbf{A}/\partial t$, described by the vector potential $\mathbf{A}(t)$ and shifted by a variable delay $\tau$. Here atomic units are used. The transition amplitude to the final continuum state $|\mathbf{v}\rangle$ of the extracted electron with momentum $\mathbf{v}$, can be described, in the strong field approximation where the final state is considered a plane wave, by the formula [**24**]:

$$a(\mathbf{v},\tau) = -i\int_{-\infty}^{+\infty} e^{i\phi(t)}\mathbf{d}_{\mathbf{p}(t)}\cdot\mathbf{E}_X(t-\tau)e^{i(W+Ip)t}dt \tag{3.16}$$

where $\mathbf{p}(t) = \mathbf{v} + \mathbf{A}(t)$ is the instantaneous momentum of the free electron in the IR field, $\mathbf{d}_{\mathbf{p}(t)}$ is the dipole transition matrix element from the initial bound state to the final continuum state $\mathbf{p}$, $W = v^2/2$ is the electron final kinetic energy and $\phi(t)$ is a phase term described by the following equation

$$\phi(t) = -\int_{t}^{+\infty}\left[\mathbf{v}\cdot\mathbf{A}(t') + A^2(t')/2\right] \tag{3.17}$$

In these equations, the scalar product $\mathbf{d}_\mathbf{p}\cdot\mathbf{E}_X$ represents the electron wavepacket generated in the continuum by the XUV field, on which the dressing IR field induces the temporal phase modulation in Eq. 3.17. This effect can be qualitatively described as follows: the trajectory of the photoelectron from the parent ion to the detector depends on the time at which it ionized by the XUV, within the IR optical cycle, since it depends on the strength of the the dressing field that interacts with it. As a result, the phase the wavepacket accumulates in each trajectory is temporally modulated by it. Notice that, due to the scalar product $\mathbf{v}\cdot\mathbf{A}$, a preferable direction for the measurement is defined. If we compare the FROG spectrogram we mentioned to the value $|a(\mathbf{v},\tau)|^2$ at a given direction, representing the electron emission probability as a

function of the electron momentum and the delay, we realize that such term (hereafter called the CRAB trace, equivalent to the RABBITT trace in our case) is formally identical to a FROG spectrogram, where the temporal gate is the pure phase term we already discussed. Actually, in order to have this formal equivalence, neither the pulse or the gate should be a function of the final electron momentum. To solve this issue, we can apply the central momentum approximation, and simply approximate $\mathbf{v}$ with the value of the center momentum in the XUV-only electron spectrum.

Once the trace, containing the information on both IR and XUV field (CRAB is a blind-FROG, where the gate is in principle unknown), has been measured, several algorithms for the reconstruction are available. Basically, any algorithm we can apply for the FROG can be adjusted and used here.

Among all the possibilities, we used a special algorithm for the attosecond pulse characterization, derived from a reconstruction scheme for lensless imaging, called ptychography [**33**]. In this framework, an object is illuminated by a coherent beam and a far-field diffraction pattern is measured for each position of the source, that is shifted every time. The illuminating beam is moved by a small amount at each measurement, in order to collect diffraction patterns from different, but partially overlapping, regions of the object. Then, an iterative algorithm is used for the reconstruction. Ptychography has been proved to correctly reconstruct the the image if the coherent illuminating beam is known, but works very well even if the characteristics of the beam are unknown. In this case, it is reconstructed together with the object image. This scheme can also be applied to object that are defined in the temporal rather than in the real space: in this case the temporal characteristics of the pulses are reconstructed, where here the measured diffraction patterns are spectra, recorded at different delays between the "coherent illuminating beam" (IR pulse in this case) and the XUV pulse to be characterized.

This methodology can be implemented in the ptychographic iterative engine (PIE) algorithm [**34**] or, if the IR pulse is unknown and has to be reconstructed as well, in the extended ptychographic iterative engine (ePIE) [**35**]. We used the latter for the reconstruction of XUV APT temporal characteristics.

The entire theoretical description of the reconstruction procedure is derived from the work [**33**]. This said, let $S(\omega, \tau)$ be the trace we already discussed, basically the modulus squared of Eq. 3.16, and $I_n(\omega)$ be a particular photoelectron spectrum at the delay $\tau_n$. For each iteration, labeled by $j$, the entire delay range is swept and every spectrum is used.

As a starting point, we consider white noise for the XUV field $E_{j=1,n=1}$ and assume a reasonable gate function $P_{j=1,n=1}$. Then, for increasing $n$, the algorithm first corrects the field and then the gate. In particular, at a given delay $\tau_n$ the exit function $\xi_{j,n}(t, \tau)$ is obtained from the field and gate functions $E_{j,n}$ and $P_{j,n}$ as follows:

$$\xi_{j,n}(t, \tau) = E_{j,n}(t) P_{j,n}(t - \tau_n) \tag{3.18}$$

Then, the corresponding Fourier transform $\xi_{j,n}(\omega, \tau)$ is computed and its magnitude is replace by the square root of the experimental function $I_n(\omega)$, while preserving its phase, just like in the FROG technique. The function is then transformed back to the time domain ($\xi'_{j,n}(t, \tau)$) and its used to correct the current estimation of the XUV pulse:

$$E_{j,n+1}(t) = E_{j,n}(t) + \beta_E U_{j,n}(t - \tau_n) \left[\xi'_{j,n}(t, \tau) - \xi_{j,n}(t, \tau)\right] \tag{3.19}$$

where $\beta_E \in (0, 1]$ is a weighting constant and the weighting function $U_{j,n}$ is computed from the gate as follows

$$U_{j,n}(t) = \frac{P^*_{j,n}(t)}{max\left\{|P_{j,n}(t)|^2\right\}} \tag{3.20}$$

The parameter $\beta_E$ must be properly set to guarantee a fast convergence and stability as well. Indeed, this parameters defines how large the field correction is: the larger, the faster the convergence but it may lead to

oscillations and instability.

A similar procedure is then used to compute the correction on the gate. Here, the exit function is computed as

$$\xi_{j,n}(t,\tau) = E_{j,n}(t+\tau_n)P_{j,n}(t) \tag{3.21}$$

then it is Fourier-transformed, its magnitude is corrected using $I_n(\omega)$ and inverse-Fourier transform $\xi'_{j,n}(t,\tau)$ is used to update the gate function, similarly to what we did with the field:

$$P_{j,n+1}(t) = P_{j,n}(t) + \beta_P V_{j,n}(t+\tau_n)\left[\xi'_{j,n}(t,\tau) - \xi_{j,n}(t,\tau)\right] \tag{3.22}$$

where $\beta_P \in (0,1]$ is a weighting constant, similar to $\beta_E$, and the weighting function $U_{j,n}$ is computed from the gate as follows

$$V_{j,n}(t) = \frac{E^*_{j,n}(t)}{max\left\{|E_{j,n}(t)|^2\right\}} \tag{3.23}$$

As an additional constraint, since in the CRAB scheme the gate is a pure phase term, we can set the gate as follows

$$P_{j,n+1}(t) = e^{i\ arg\{P_{j,n+1}(t)\}} \tag{3.24}$$

Once the entire delay range is considered, the same procedure is applied for the iteration $j+1$ and so on.

In order to have a successful reconstruction an important condition has to be met: the electron spectrum should be identical to the photon one. The reason for this is quite intuitive: the CRAB method is able to reconstruct the APT by extracting information from the spectrogram only. Therefore, the XUV burst that is obtained at the end is the one related to the electron spectrum: if the latter differs from the photon spectrum, the reconstructed APT would be untrue. To match such condition, different approaches are possible. The most efficient one is to set the voltage parameters of the lens and drift tube (Chapter 2, Section 4) in order to match the electron to the photon spectrum, during the measurement. The main reason for this difference is that in general the ToF does not have a flat response and therefore the photon spectrum is not directly reproduced into the electron one. This approach

is preferable if we want to minimize the elaboration of the signal after the measurement, operation that typically worsens the signal-to-noise ratio. This method is however difficult to be fully applied, since it is hard to compare the two spectra live. As a result, an additional elaboration of the signal is required. Figure 3.23 shows an example of the post-measurement electron spectrum correction, applied to the case of longer pulses (narrower spectra). The basic idea is very simple: find the energy-dependent transfer function that transforms the XUV-only electron spectrum to the photon spectrum (figures 3.23a and 3.23b) and apply it, slice by slice, to the entire trace. Figure 3.24 shows a comparison of the corrected and non corrected trace. As we can see from the previous figures, such approach is very powerful but critical at the same time. Indeed, since the correction typically involves the computational amplification of one part of the signal, the noise is typically increased as well, for example in the low-energy part of the trace in our case. If the SNR is an issue in the experiment, this method is not suitable.

Once the trace has been properly elaborated, we ran the ePIE algorithm to reconstruct both the IR pulse and XUV pulse train. The result shows a train of about ten main pulses and few more small satellites, with an average duration FWHM of 410 as, about 50 as more with respect to the reconstruction using RABBITT. Moreover, the train has a duration of about 10.7 fs , slightly longer than the result from section 2. The result is illustrated in figure 3.25. Despite both values are larger than the ones we obtained from RABBITT, nevertheless the results are comparable. For example, even in the reconstruction by CRAB the pulses appear with a small after-pulse that, in some cases, merges to the main pulse in a sort of "shoulder" (see figure 3.16). To prove the goodness of the reconstruction, we can observe a comparison of the experimental trace with the one we reconstructed, as illustrated in figure 3.26. The result is really encouraging, as the sidebands oscillations are properly reconstructed. The only issue is related to the

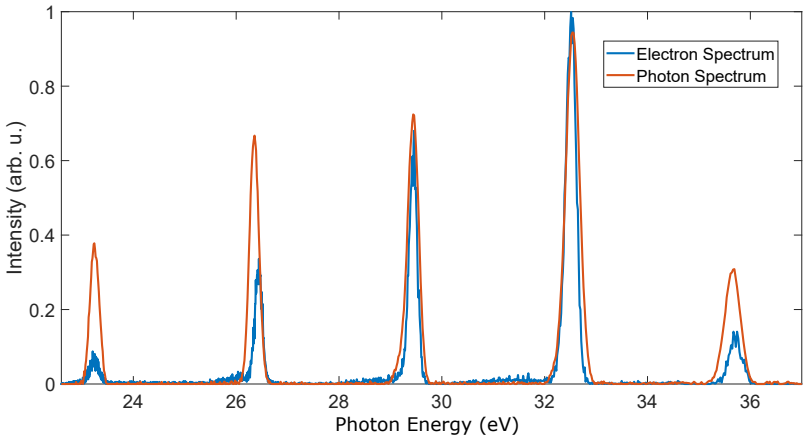


(A) Photon and non-corrected electron spectra.

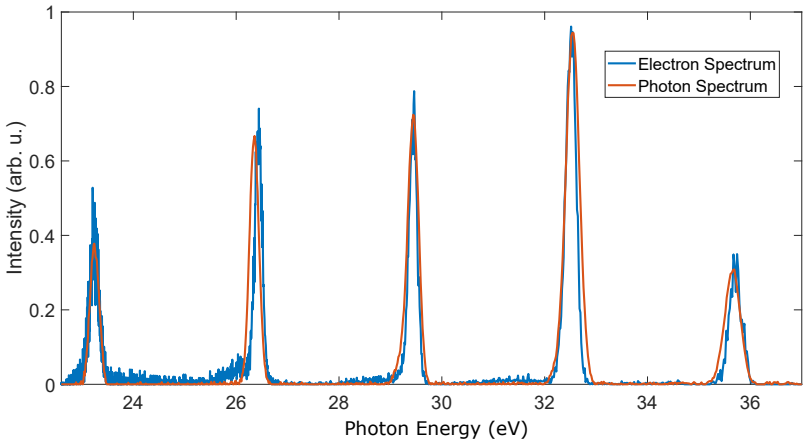


(B) Photon and corrected electron spectra.

FIGURE 3.23. Electron spectrum correction, obtained by calculating the transfer function that turns the electron to the photon spectrum. Such energy-dependent function can be used to correct the entire trace. The main drawback of this method is evident: the signal-to-noise ratio is worsened.

last sideband, at about 16 eV that is not properly reconstructed by the procedure. The main reason is that in this particular spectral region the signal-to-noise ration is very low.

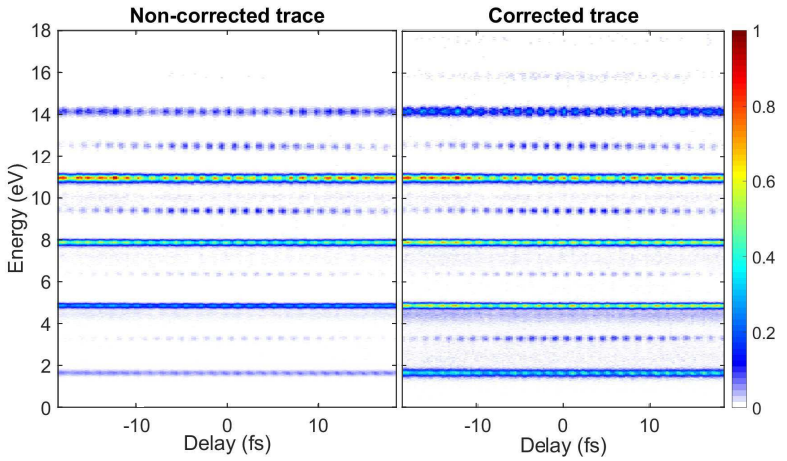


FIGURE 3.24. Crab trace correction, obtained by multiplying, slice by slice, the correction profile computed by properly comparing electron and photon spectra.

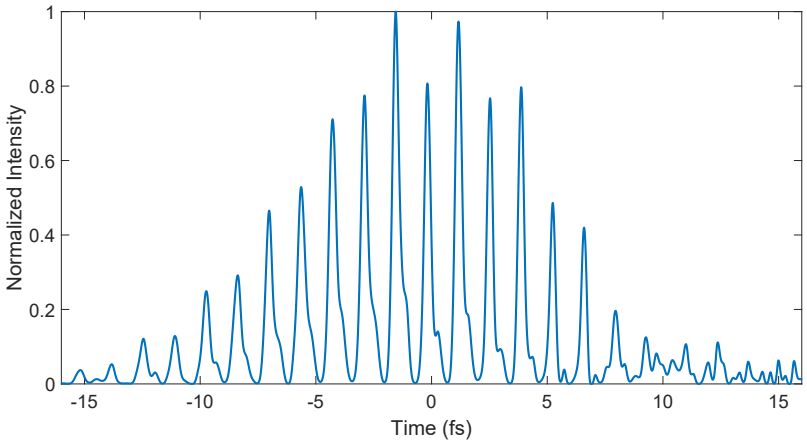


FIGURE 3.25. XUV APT generated by longer IR pulse (empty hollow-core fiber). It is made of 10 main pulses, with an average duration of about 410 as.

Being a blind-FROG method, the CRAB also provides a reconstruction of the IR pulse. To understand if the result is reliable we can compare the reconstructed IR field to the one we obtained from FROG, as we did in figure 3.27. The result is rather positive, since the IR FWHM

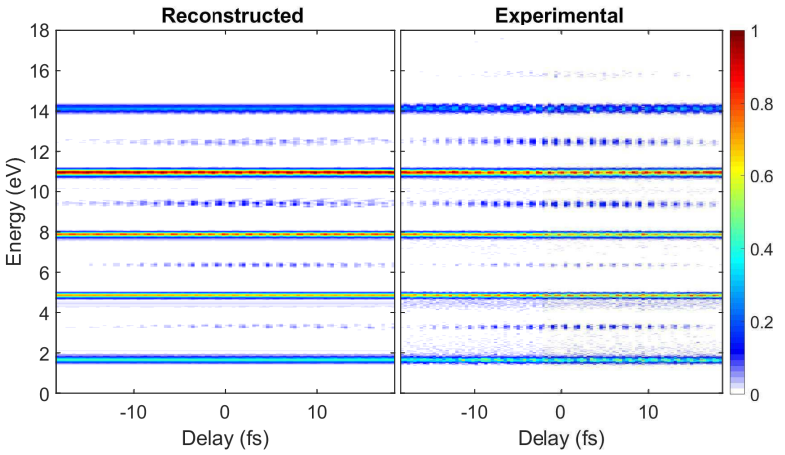


FIGURE 3.26. Comparison of the reconstructed and experimental CRAB trace.The result is very positive as the correct oscillation of the sidebands is reconstructed. The only issue is that the sideband at about 16 eV is not properly reconstructed. The main reason is that the noise in that spectral region is particularly relevant if compared to the sideband signal.

resulting from CRAB, computed using a Gaussian fit, is 20.1 fs, quite close to the value we obtained from FROG (20.4 fs). This suggests that the reconstruction is precise and the reconstructed XUV field is reliable.

We present now the case of shorter pulses obtained, as stated several times, by using an hollow-core fiber filled with 1.5 bar of Ne. The procedure we used for the reconstruction is the same as the one we applied in the case of longer pulses. Indeed, we first corrected the trace, using the transfer function we computed by comparing the electron and photon spectra (figure 3.28). Similarly to what we saw in figures 3.23 and 3.24, the correction procedure worsens the SNR in some spectral regions. However, the resulting trace is still suitable for a good reconstruction. The final result shows a train of four main pulses and four more small satellites, with an average duration FWHM of 263 as, about

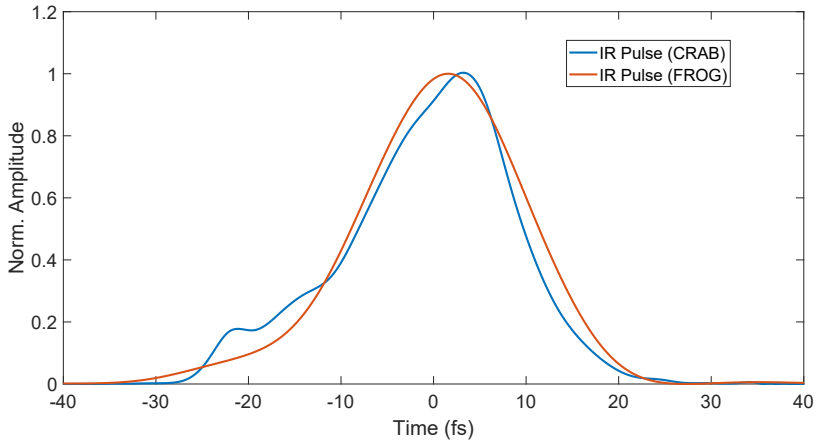


FIGURE 3.27. Comparison of the IR pulses reconstructed by FROG and CRAB. The durations of the two pulses, computed by means of a Gaussian fit, are 20.1 fs and 20.4 fs for the CRAB and FROG reconstruction respectively.

50 as more with respect to the reconstruction using RABBITT, like with longer pulses. Moreover, the train has a duration of about 3.4 fs, slightly longer than the result from section 2. Again, in order to be sure that the reconstruction is reliable, we can compare the reconstructed and experimental trace (figure 3.29a), and the IR pulse reconstructed by CRAB with the one we obtained by FROG (figure 3.29c). The result is in both cases rather positive. As for the trace comparison, we realize that the algorithm was able to reconstruct all the features of the experimental data, like the sidebands and harmonics oscillations and the tilt of the sidebands. As for the reconstructed IR profile, the FWHM resulting from CRAB is 10.9 fs, quite close to the value we obtained from FROG (11.8 fs).

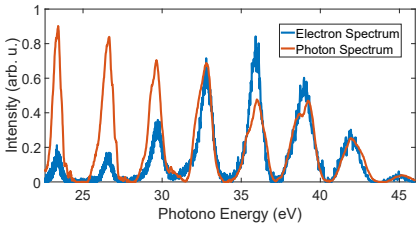


(A) Photon and non-corrected electron spectra.

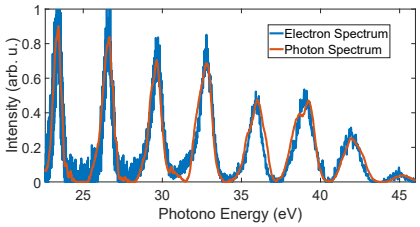


(B) Photon and corrected electron spectra.

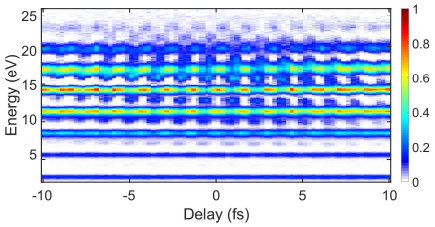


(C) Non-corrected CRAB trace.

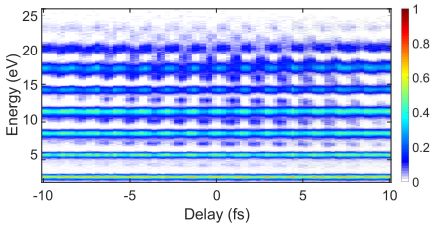


(D) Corrected CRAB trace.

FIGURE 3.28. Electron spectrum correction, obtained by calculating the transfer function that turns the electron to the photon spectrum. Such energy-dependent function can be used to correct the entire trace. The main drawback of this method is evident: the signal-to-noise ratio is worsened.

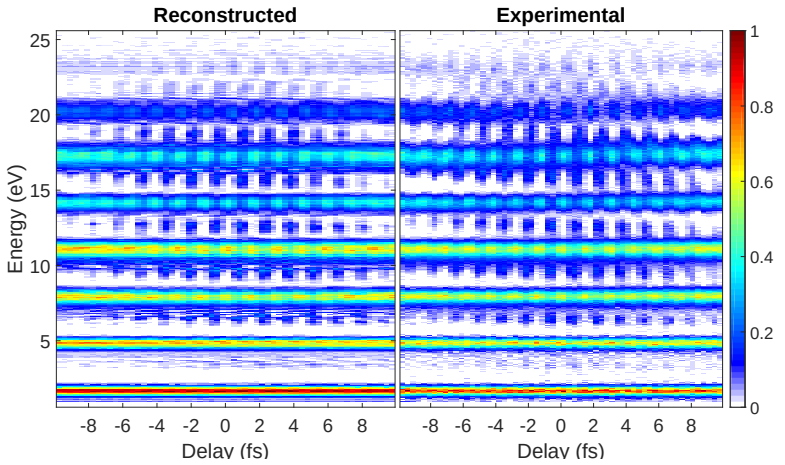


(A) Comparison of experimental and reconstructed CRAB trace.

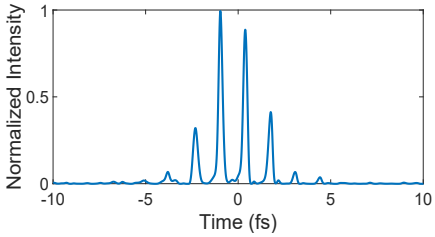


(B) Reconstructed XUV APT.

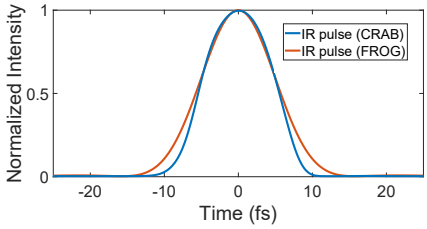


(C) Reconstructed IR pulse.

FIGURE 3.29. (A) Comparison of the experimental and reconstructed CRAB trace. The result is in very good agreement with the experimental data. (B)(C) Reconstruction of the XUV burst and IR pulse by means of the CRAB, corresponding to an APT of 3.4 fs length and containing pulses with a FWHM of 263 as. The comparison with the IR pulse obtained by FROG is also shown. The duration of the reconstructed pulse amounts to about 10.9 fs, similar to the value obtained by FROG (11.8 fs).

CHAPTER 4

# Benchmarking the Experimental Setup

After extracting the temporal properties of the IR and, most importantly, of the XUV pulses and after observing that, since we were able to do measurements described in Chapter 3, the apparatus is stable enough for measurements with attosecond resolution, we proceeded to the characterization of the experimental setup by performing some experiments on known samples. In particular, we measured the static reflectance of silicon, titanium and germanium samples at different incidence angles and for different energies, and compared the experimental results to either measured or calculated data. The results we found are very promising, as a very good agreement to the benchmark data is recovered.

We decided to collect 25 spectra for each angle, in order to mitigate the effect of the harmonic fluctuations and to reduce the noise on the measurement itself (uncertainty data are shown in the following figures via the displayed error bars). Moreover, we decided to collect the reference data together with the sample data, by switching back and forth between the sample and the gold-coated mirror (Chapter 2, Section 5), in order to reduce the error introduced by the uncertainty on the motors positions. Furthermore, in order to weaken the impact of the human control on the reflectometer motors, we decided to always measure twice and collect data in two separated sweeps.

To correctly measure the reflectance of the samples, some additional analysis is required. In particular, the reflectance of the second mirror must be taken into account, since it is made of gold that, in spite of being a very good reflector, may introduce some distortion of the measured spectra. In fact, being $I_0$ the input XUV intensity to the

reflectometer, the measured intensity is

$$I_{m,s} = R_2 R_s I_0 \tag{4.1}$$

where $R_2$ is the gold reflectance, related to the second mirror and $R_s$ is the sample reflectance, the one we should measure. Because of $R_2$, it is not possible to directly assess the sample reflectance by a single measurement. Moreover, as no information on $I_0$ is available, an additional measurement is required. We used another mirror in place of the sample, as described in Chapter 2, Section 5, to collect reference data, such that, for each run and angle, we also measured

$$I_{m,Ref} = R_2 R_1 I_0 \tag{4.2}$$

where now $R_1$ is the gold reflectance related to the first mirror, at the sample position. The final information we obtain is the relative reflectance of the sample, with respect to gold, computed as follows

$$\frac{I_{m,s}}{I_{m,Ref}} = \frac{R_s}{R_1} \tag{4.3}$$

Notice that such ratio is computed by considering the peak value of the harmonics in the measured spectra. In particular, we decided to use Gaussian fits to properly identify the position of the harmonics peaks in each spectrum and then extract the value of the intensity at that specific point.

As a result of Eq. 4.3, for extracting the information on the sample reflectance, absolute data about gold reflectance are needed. Since gold is a noble metal which does not degrade easily even if exposed to air, we decided to use calculated values for the reflectance of such material. As an example, figure 4.1 shows the reflectance of gold as a function of the angle of incidence, from 60° to 80°, for 39 eV (about the center of our typical XUV spectral region, corresponding to harmonic 25) and for s-polarized radiation. Such function is almost linear and the variation over 1° is of only 2%. Therefore, we expect that a possible error coming from the uncertainty on the angle of incidence would be negligible, considering that our rotors have a precision of 10m° by

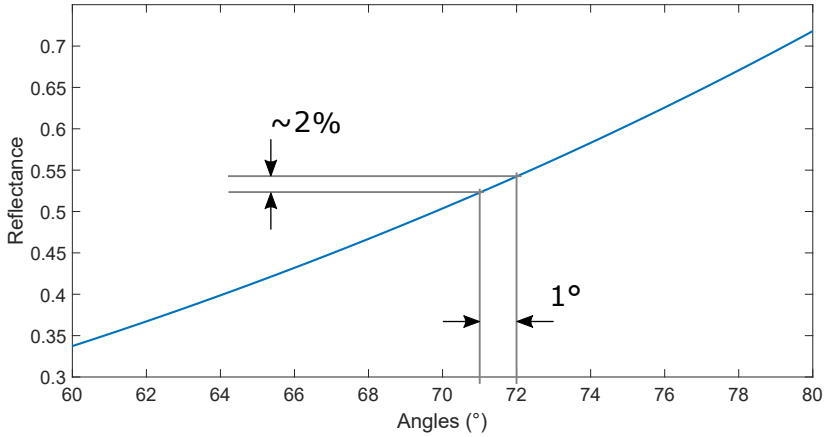


FIGURE 4.1. Gold reflectance as a function of the angle of incidence, at 39 eV (harmonic 25) and for s-polarized radiation. Over 1° variation, the reflectance changes of only 2%.

datasheet(Chapter 2, Section 5). Eventually, the results were very encouraging.

## 1. Silicon Sample

The first experiment we carried out was on silicon. The sample we used was a calibrated one, since its angle and energy-resolved reflectance was measured, with extremely high precision, at the Elettra synchrotron facility in Trieste, to be specifically used for testing our experimental apparatus. However, these results could not be directly used for the comparison, since they where measured for two angles, 5° and 80°, that lie outside the range our system can sweep (Chapter 2, Section 5). To elaborate them, we relied on the Fresnel law and fitted the reference data with the following model

$$R_s = \left| \frac{n_1 cos\theta_i - n_2 \sqrt{1 - \left(\frac{n_1}{n_2} sin\theta_i\right)^2}}{n_1 cos\theta_i + n_2 \sqrt{1 - \left(\frac{n_1}{n_2} sin\theta_i\right)^2}} \right|^2 \tag{4.4}$$

showing the angle-dependent reflectance for s-polarized light.

Figure 4.2 displays the experimental results for all the harmonics, at an angle of incidence from $60^o$ to $78^o$. The result is very promising as a good agreement with the reference data is reached, both in terms of angular and energy dependence. It is also worth mentioning that the experimental setup appears to be very robust, since the two experiments, that basically exhibit the same result, were run on different days and the apparatus was reset and moved in between the two. In spite of that, no meaningful difference appears in the two sets of data. An important issue is related to the measurement performed at higher incidence angles and the resulting data may be less reliable. Indeed, in this case the alignment procedure is much more delicate since a very small uncertainty on the angle of the sample or mirror rotor produces a very large uncertainty on the entrance direction and position of the beam in the spectrometer. Since before the detection the XUV pulse interacts with a grating at grazing incidence, a slight misalignment, resulting in part of the beam being cut away, may produce inaccurate data. This is particularly evident in our experiments, since for example for higher angles the reflectance seems to have a non-monotonic behavior. Also for this reason, in the second run we were forced to stop at $75°$.

As the comparison showed a quite satisfactory result, we tried to match the measured data to some calculated values, also considering that Si oxidizes as soon as it is exposed to air. In particular, we calculated the reflectance for a Si substrate, with a layer of variable thickness of $SiO_2$ on top. Unfortunately, any possible comparison failed and no silicon oxide thickness was found to produce a reflectance that matched the experimental value. The main reason for this could be that the quality of the sample is very poor and it was probably contaminated by alien substances, changing its surface properties.

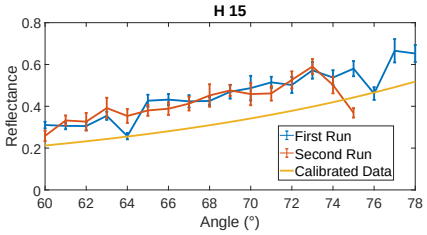


(A) Si reflectance at about 23 eV.

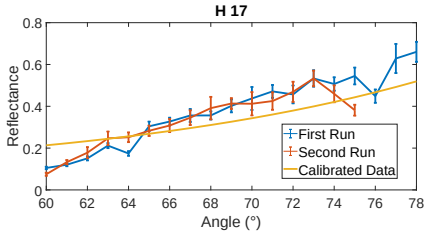


(B) Si reflectance at about 26 eV.

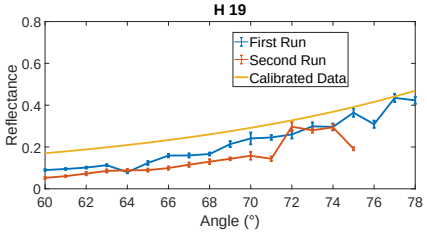


(C) Si reflectance at about 29.5 eV.

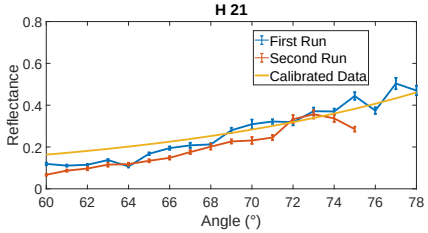


(D) Si reflectance at about 33 eV.

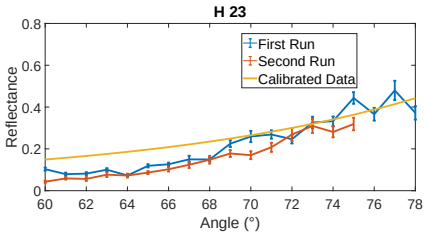


(E) Si reflectance at about 36 eV.

FIGURE 4.2. Si reflectance, measured for angles from 60° to 78° and energies from about 23 eV (harmonic 15) to 36 eV (harmonic 23). The results, obtained in two different runs, are compared to reference data, obtained from measurements performed with very high precision at a synchrotron facility (Trieste). As we can observe, the experimental results are in very good agreement with the calibrated data. In case of harmonic 15 our results seem to slightly overestimate the reflectance, whereas in all the other cases the results are quite comparable to the reference. The measurement for higher angles is very delicate and the data are typically less reliable than the ones for smaller angles.

## 2. Titanium Sample

Since the outcome of the very first experiment was positive and encouraging, we decided to try our setup with many different samples, in order to have as many benchmark results as possible. The second substance we tested our system on was titanium (Ti). Having no precisely measured data on this sample, we only relied on simulation and calculation to compare the experimental results to.

Reference data were obtained by simulations run on MATLAB®, implementing a simple model for angular dependent reflectance, based on the determination of the Fresnel coefficients and applying it to arbitrarily complex layered structure. The approach we used ([**36**]) relies on the usage of a transfer matrix method, much more powerful and computationally efficient than any layer-by-layer method (see Appendix C).

In order to use such formalism to calculate the angular reflectance of the multilayer, the refractive index of all the substances is needed. In some cases, it is very difficult to find a measured refractive index in the XUV spectral region, so it is often useful to calculated it. The main issue in doing so is that no Sellmeier's equations or similar exist for this radiation energy. A useful tool that can be used to calculate the refractive index for such high-energy radiation, once we know the chemical composition of the material of interest, is represented by the atomic scattering factors, as we can see in Appendix D. The main limitation of this approach is that it is reliable only for energies above the 30 eV

In order to find a suitable reference for our experiment, we considered that typically titanium, when exposed to air, forms a passive oxide layer ($TiO_2$) of about 50 Å on top of a substrate of pure Ti. Fortunately, in this case reflectance data were available (we used the free version of the software IMD by Reflective X-ray Optics[1]), so we could

[1]http://www.rxollc.com/index.html

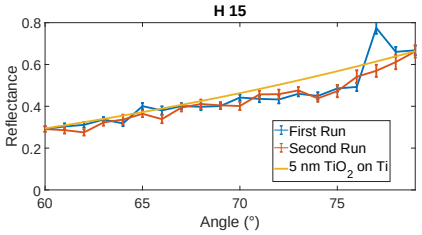


(A) Ti reflectance at about 23 eV.

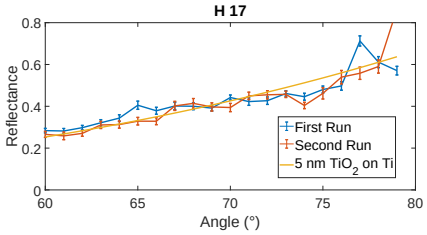


(B) Ti reflectance at about 26 eV.

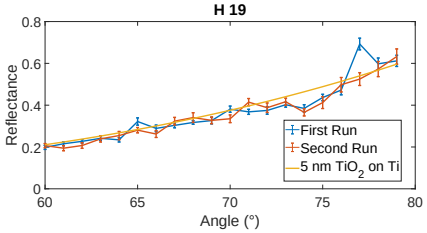


(C) Ti reflectance at about 29.5 eV.

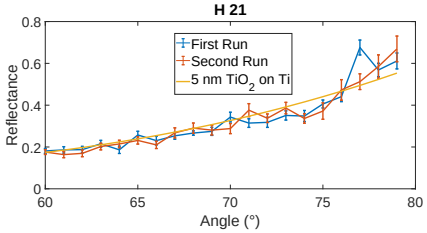


(D) Ti reflectance at about 33 eV.

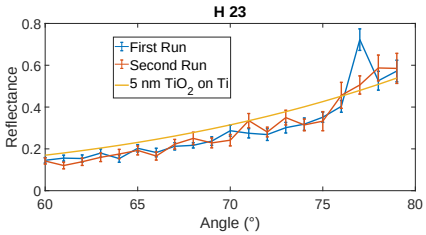


(E) Ti reflectance at about 36 eV.

FIGURE 4.3. Reflectance of the Ti sample, compared to the calculated data of Ti with 5 nm of $TiO_2$ on top, measured for angles from 60° to 79° and energies from about 23 eV (harmonic 15) to 36 eV (harmonic 23). Again, we ran two separate experiments and compared to calculated values, obtained from tabulated refractive index data. The result is very positive and compares well to the simulated data. Even in this case, the reflectance for higher angles is less accurate.

compare the reflectance data to the tabulated values for all the energies we have access to. The experimental result and the comparison to such simulated structure is shown in figure 4.3. Just like the experiment on

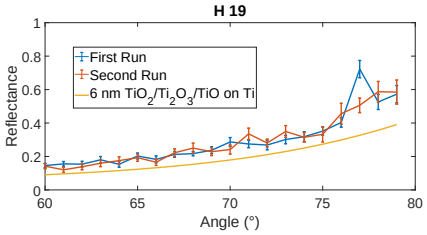


(A) Ti reflectance at about 29.5 eV.

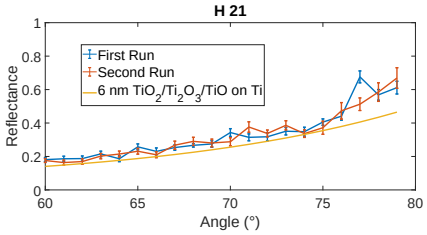


(B) Ti reflectance at about 33 eV.

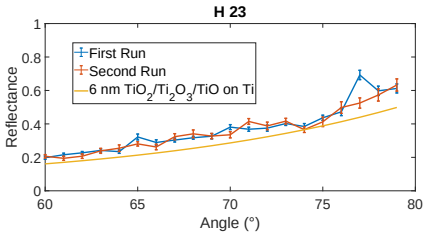


(C) Ti reflectance at about 36 eV.

FIGURE 4.4. Reflectance of Ti sample, compared to calculated data of Ti with a complex oxides structure on top ($TiO_2/Ti_2O_3/TiO$), measured for angles from 60° to 79° and energies from about 29.5 eV (harmonic 19) to 36 eV (harmonic 23). The results from the two separate runs are compared to simulated values, obtained from calculated refractive index data (for this reason harmonics 15 and 17 are omitted). The result is very positive and compares well to the simulated data.

silicon, we ran two subsequent series of measurements, at angles from 60° to 79° and for all the available harmonics. In the two cases the results are very much alike, besides the normal deviations that may arise due to the difficulty in blindly aligning the reflectometer at each measurement, verifying again that the setup is very robust. Moreover, in this case the agreement with calculated data is exceptional, confirming that our experimental apparatus is also reliable.

According to the work [**37**], another typical structure for oxidized titanium consists on the multilayer $TiO_2/Ti_2O_3/TiO$ with a total thickness

of 6 nm (we considered 2 nm per layer), on top of pure Ti. We decided to test our experimental results with this kind of structeure. Unfortunately, in this case we were forced to compute the reference reflectance data by estimating the refractive index, since no tabulated data were available in our spectral region. For this reason, the results for harmonics 15 and 17 are omitted. Figure 4.4 shows the results. Even in this case the result is quite encouraging, as the calculated reference reflectance compares very well with the measured data

## 3. Germanium Sample

Last benchmark experiment was done on germanium (Ge). In this case the comparison to either measured or calculated values of the reflectance was very difficult. Indeed, we first tried to compare the measurements to calculated reflectance for pure Ge, but the result was not satisfactory. Therefore we decided to try a comparison considering some layer of germanium oxides but since we did not find any typical structure we could consider, we opted for a trial-and-error approach, considering the case of ($GeO_2$). Another problem was that no tabulated data for the refractive index of germanium oxide were available, so we had to use the tool described in Appendix D but, as mentioned, the results from this method are reliable for energies greater than 30 eV, so harmonics 15 and 17 were excluded. On the other hand, we were able to extract information from higher harmonics, assessing reflectance data at higher energy. Additionally, we considered the effect of surface roughness and we found many possible structures that would match with the data within our experimental uncertainty. In particular, we observed that an increasing oxide thickness increases the reflectance, whereas larger surface roughness determines, of course, a reduction in the reflection signal. For this reason, we could basically tailor the characteristics of the sample in the simulation, in order to match the experimental data. However, being our setup made for measuring the reflectance and not for the determination of the nature of the sample,

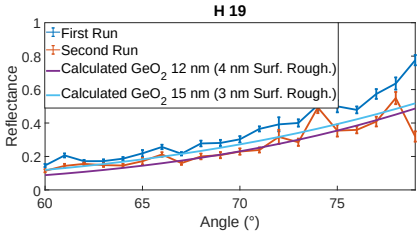


(A) Ge reflectance at about 29.5 eV.

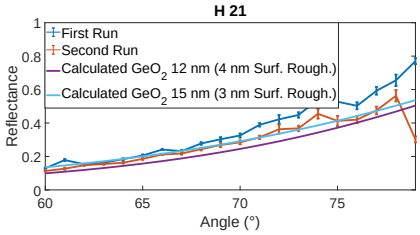


(B) Ge reflectance at about 33 eV.

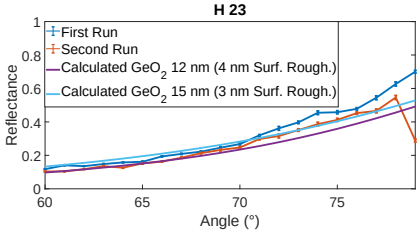


(C) Ge reflectance at about 36 eV.

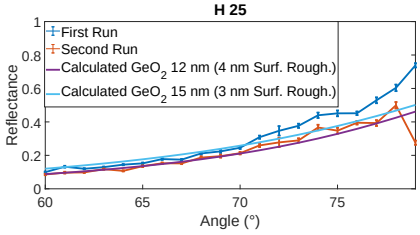


(D) Ge reflectance at about 39 eV.

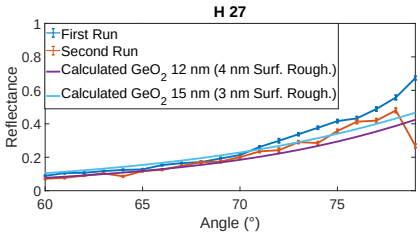


(E) Ge reflectance at about 42 eV.

FIGURE 4.5. Reflectance of the Ge sample, from harmonic 19 (about 29.5 eV) to 27 (about 42 eV), compared to the calculated reflectance of $GeO_2$, with different oxides features, on top of pure Ge.

the result was still very positive. Figure 4.5 displays the experimental results for the two consecutive runs as well as calculated data for two possible structures of the multilayer, among the many suitable ones we computed.

CHAPTER 5

# Conclusions and future perspectives

We have developed an experimental setup for performing pump-and-probe transient reflectance experiments on solids with attosecond resolution. First of all, we have built the apparatus and designed some major parts, rearranging an existing system that was not suitable for this kind of measurements. In particular, we have constructed, entirely from scratch, the reflectometer, a very simple device allowing us to perform time-resolved experiments with very good energetic and angular resolution. Then, we have characterized the apparatus, in order to measure its performances. In particular, we have observed that the system is able to produce attosecond pulse trains with a duration of about 3.5 fs, consisting of a set of XUV pulses with about 260 as FWHM. Such APTs are generated using an IR pulse, suitably compressed by means of an hollow-core fiber, filled with neon. As a result, the IR pulse has a duration of about 12 fs. Then we have tested the reliability of the setup by measuring the static reflectance of known samples. The results are very promising and we expect to perform temporal-resolved measurements very soon. In particular, our idea is to measure the transient reflectance of samples that have never been studied before, focusing on materials of great technological importance, from semiconductors to topological insulators. In this perspective, our aim is to access the transient dielectric function of such material, mirroring the phenomena involving ultra-fast electron dynamics.

In terms of improvement of the presents apparatus, many things can be done to boost the performances of the system. For example, we can improve the generation of high-order harmonics by implementing a well known scheme for the IR pulse compression, consisting in the

differential pumping of the hollow-core fiber for self-phase modulation, that can lead to a significant improvement of both spatial and spectral features of the pulses. Indeed, with a constant pressure inside the fiber, the maximum pulse energy is limited, since with too high intensity, phenomena like self-focusing and ionization arise and they can reduce the beam quality. If we use a pressure gradient, we can first of all improve the coupling of the beam to the fiber, since no plasma is formed at the entrance, and also, because of the gradual self-phase modulation the pulse experiences, losses can be dramatically reduced [**44**] and high-quality very short laser pulses can be obtained even with significantly large energy.

Finally, if our aim is to have a system with extreme temporal resolution, we can implement a strategy for the generation of isolated attosecond pulses, like polarization gating [**45**]. Actually, as soon as we conclude the characterization experiments on the beam line, in order to be completely sure that the apparatus is working properly, we plan to immediately implement such scheme, for single XUV pulses generation.

APPENDIX A

# Acousto-optic modulators

The use of acousto-optic modulators (AOM), such as the acousto-optic programmable gain control filter (AOPGCF) for spectral amplitude shaping, together with the acousto-optic programmable dispersive filter (AOPDF) for spectral phase control, is very effective in dealing with the problem of gain narrowing, an effect that can compromise the generation of very short pulses out of chirped-pulse amplifier.
The basic operating principle of both devices is the same and quite easy to be understood. The AOPDF is based on a collinear acousto-optic interaction of the electromagnetic radiation with an acoustic wave, generated in a birefringent crystal (paratellurite, $TeO_2$)[**46**] by a piezo-actuator, driven by a signal $S(t)$ with a variable frequency over time, in the radio-frequency range. The transducer launches a wave that propagates with a velocity V in the crystal, reproducing in space the temporal profile of the electrical signal. As the velocity of the optical wave is much larger than the one of the acoustic wave and since we can assume very short optical pulses, the incident electromagnetic radiation sees a static dielectric grating inside the device, represented by the following equation [**47**]

$$\epsilon(z) = \epsilon + 2\epsilon_1 cos[\psi(z)] \tag{A.1}$$

where $\epsilon$ is the unperturbed dielectric tensor and $\psi(z)$ is the acoustic phase. Such grating, as a result of the interaction with the electromagnetic wave, produces scattering of the latter and a change in its polarization. We call the entrance mode the Mode 1 and the scattered

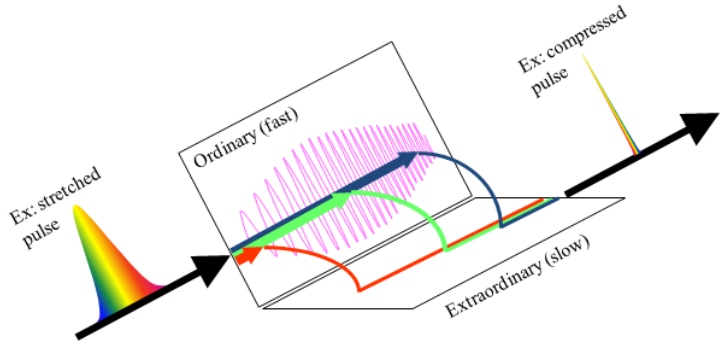


FIGURE A.1. Basic operating principle of the AOPDF and AOPGCF: different wavelengths are scattered in different positions inside the crystal, based on acousto-optical effects. The dispersion can be arbitrarily controlled by setting the scattering position inside the crystal. The main difference between the two devices is that with an AOPDF the scattered pulse, whose dispersion can be finely tuned, is of interest and the residual transmitted part is lost, whereas with an AOPGCF the scattered frequencies are removed from the main, unscattered beam.

one the Mode 2. A representaion of such phenomenon is shown in figure A.1[1].

The diffracted optical wave spectral phase and amplitude can be controlled respectively by the instantaneous frequency of the acoustic wave and its intensity. In fact, as we already said, the electric signal is chirped (its frequency is a function of time) and the acoustic signal replicates this behavior in the spatial domain. As it is well known [**46**],[**47**], two optical modes can be efficiently coupled by an acoustic wave, only in the case of phase matching between the three. Assuming that the frequency chirp of the acoustic wave is monotonic (not

[1]https://commons.wikimedia.org/wiki/File:AOPDF_principle.png. Picture licensed under CC BY-SA 3.0.

necessarily true), in the acoustic grating there exist only one position $z$ with the correct acoustic frequency, providing phase matching and therefore scattering of each optical frequency in the pulse. This means that, each frequency in the optical pulse will travel a certain distance inside the crystal before being scattered, at a position $z(\omega)$. Therefore, at $z(\omega)$ part of the energy in Mode 1 is scattered into Mode 2 (with a different polarization, for simplicity orthogonal to the previous one but non compulsory to the implementation of an AOPFD). The pulse that leaves the device is now made of different spectral components, each one diffracted at a different position. Since the crystal we use is birefringent, the two modes have a different velocity, meaning that each spectral component is independently delayed with respect to the other. Then, by properly setting the temporal shape of the RF signal driving the piezo-actuator and therefore choosing the form of the acoustic wave, an arbitrary group delay distribution as a function of the frequency can be generated. More precisely, by setting the amplitude and instantaneous frequency of the optical wave at each position, we can freely control the amplitude and the phase of each pulse spectral component, respectively. From a more mathematical point of view, the output diffracted field is related to input one and the RF signal by the following expression [**48**]

$$E_{out}(t) \propto E_{in}(t) \otimes S(t/\alpha) \tag{A.2}$$

where the scaling factor is $\alpha = \Delta n \frac{V}{c}$, depending on the ratio of the speed of the sound to the speed of light and on the difference in refractive indexes between the ordinary and extraordinary axis of the crystal. If we now consider the Fourier transform of the above mentioned output field, we obtain

$$E_{out}(\omega) \propto E_{in}(\omega) S(\alpha\omega) \tag{A.3}$$

Clearly the function $S(\alpha\omega)$ behaves like a transfer function of a filter (and $S(t/\alpha)$ is its impulse response). Therefore, by properly choosing the function $S(t)$ we can tune the spectrum of the pulse, limited only

by the maximum bandwidth of the signal we can generate, by simultaneously and independently controlling both the amplitude and the phase, allowing for the generation of short, transform-limited pulses. In our system, the $TeO_2$ crystal is 2.5 cm long, the speed of sound is V=1000 m/s and the refractive index difference is $\Delta n = 0.04$ corresponding to a scaling factor $\alpha = 10^{-7}$.

As we said, the main role of the AOPDF is to control the spectral phase of the pulse and it is used to pre-compensate for the large dispersion introduced by the AOPGCF, the real player devoted to suppression of the gain narrowing issue. The AOPGCF is a device able to accurately control spectral losses inside the cavity of the regenerative amplifier [**49**], thus shaping the spectral amplitude of the pulse. This can be used to contrast gain narrowing. Spectral losses are obtained through partial diffraction of the unwanted spectral component. The device, indeed, behaves like a programmable spectral filter, with a transmission modified by the induced diffraction: total diffraction of a wavelength corresponds to zero transmission whereas no diffraction of a wavelength corresponds to 100% transmission. To optimize the diffraction efficiency, the device is based on the same principle as the AOPDF (quasi-collinear propagation of the optical and acoustic waves for maximizing the efficiency, etc.), with the only difference that now the part of the wave we are interested in is the non-scattered one. Indeed, in our configuration the scattered field is lost whereas the transmitted one remains in the regenerative cavity and is amplified. Since all the parameters of the crystal are well determined, the calibration of the device is easy and can be instantaneously done by software. The idea is simply to check the accuracy of the device action by setting, for a narrow spectral range around a given wavelength, the maximum losses. This will produce a hole in the pulse spectrum, that can be checked on a standard spectrometer. Now, by comparing the programmed hole wavelength and the measured one, the control software is immediately able to calibrate the system. The main drawback of this device, as

we already discussed, is the significant dispersion introduced by the 25-mm long $TeO_2$ crystal. In particular, at 800 nm the second, third and fourth order dispersions, by manufacturer data, are respectively 12406 $fs^2$, 8114 $fs^3$ and 4700 $fs^4$, which are amplified by the passages in the regenerative amplifier. Using the compressor one can easily compensate for second order dispersion but nothing can be done to cope with the higher orders. To help with this, we use an AOPDF, as already discussed, to pre-compensate for this additional dispersion.

The correction of gain narrowing is therefore carried out by both devices, to produce a minimum-duration pulse. To do so, the AOPGCF is used to flatten the spectral amplitude of the pulse, by increasing losses for the peaks in the spectrum, whereas the AOPDF is used to flatten the phase, thus obtaining a transform-limited pulse. Such result is obtained by very few optimization passages, used to optimally program the parameters of both devices. The amplitude optimization is really straightforward, as it is obtained by a direct feedback to the AOPGCF, based on the measured pulse spectrum. The spectral amplitude of the pulse is indeed directly used as the spectral amplitude to be diffracted away by the filter. Doing so, the peaks are more attenuated than the valleys and the spectrum converges onto a roughly square shape. In fact, the goal of this setup is to determine the optimal losses configuration, suitable for globally flattening the shape of the amplifier gain (namely compensating for gain narrowing). This optimization procedure is really robust and powerful, since for the flattening of even a very broadband gain, very few steps are needed. Not to mention that, once the optimal configuration is found, it can be used as long as the cavity is not changed. Indeed, day-by-day fluctuations are small enough not to require major re-optimizations. Then, the phase optimization is obtained by another procedure, similar to the previous one. The phase of the pulse is measured by the FROG (see Chapter 3, Section 1 for a discussion) and the AOPDF is driven by this. In particular, the device is programmed to add to the pulse a phase that is the opposite of the

measured one. With few steps, a relatively flat phase is reached.

Another important use of the acousto-optical modulators (AOM) is the stabilization of the carrier-envelope phase (CEP) of the pulses generated by the mode-locked laser system. It is simply the relative phase of the underlying carrier wave with respect to the envelope, also called the absolute phase. In general, the CEP is not important in optics; however, for ultrashort laser pulses, with a duration of few optical cycles it may become relevant and have physical consequences. For example, it may have an influence on the conversion efficiency of nonlinear optical processes, like high-order harmonic generation (HHG), since they strongly depend on the instantaneous electric field strength [**50**]. Also, in specific HHG schemes, like in the generation of isolated attosecond pulses, the CEP stability is required. In general, the CEP is not constant from pulse to pulse, as a result of the difference in the phase and group velocity in the cavity [**51**]. In this framework, the carrier wave "slips" with respect to the envelope and each pulse shows an additional absolute phase $\Delta\Phi$ with respect to the previous one. The scheme for controlling the CEP is relatively easy to be understood. It is known that the spectrum of a mode-locked laser is a comb of evenly spaced frequencies, with a separation equal to the round-trip frequency in the laser cavity (also called repetition rate, $f_{rep}$). It can be proved that such frequencies are not necessarily integer multiples of the repetition rate, as the presence of a non-zero absolute phase produces an offset of the comb. It can observed that, if the pulse-to-pulse phase shift is equal to $2\pi/m$, where $m$ is an integer, then the frequency offset is equal to $f_{rep}/m$ and every $m$ pulses have the same CEP. Additionally, the pulse-to-pulse phase may experience fast fluctuations and slow drift, thus every pulse is in principle different from the other. In order to suppress those effects and produce, out of the mode-locked laser system, a train of identical pulses, both the pulse-to-pulse phase contribution and its fluctuations have to be suppressed. In order to achieve such result, an acousto-optical modulator, like the AOPDF we already discussed, can

be used to control the power of the oscillator pump allowing for a direct control and stabilization of the measured CEP shift [**52**]. To measure the absolute phase shift many approaches are possible, requiring in any case the use of non linear effects. The simplest one relies on the use of the second-harmonic generation process (SHG) and consists of measuring the beat signal produced by the blue-part of the non-doubled pulse spectrum and the red-part of the spectrum after frequency doubling via SHG. In particular, let $f_n = nf_{rep} + f_{shift}$ and $f_{2n} = 2nf_{rep} + f_{shift}$ be the $n$th and $2n$th frequencies in the mode-locked frequency comb. Consider now the frequency-doubled signal $2f_n = 2nf_{rep} + 2f_{shift}$. We clearly have that $2f_n - f_{2n} = f_{shift}$. This means that the beating signal produced by the two oscillates at a frequency $f_{shift}$, directly related the CEP shift and therefore, by analyzing the spectrum of the beating signal and driving the AOM to stabilize or control the beat note, the CEP can be directly stabilized and controlled. In our apparatus this approach is implemented for the stabilization of the fast fluctuations of the CEP at the oscillator.

APPENDIX B

# High-order harmonic generation

High-order harmonic generation (HHG) is a highly non linear process that occurs when a target (for example gas) is illuminated by a laser pulse with high intensity ($\approx 10^{14}\ W/cm^2$). The interaction with the target atoms produces high harmonics of the illuminating laser radiation. Such a process is of great importance since it can be used to generate radiation in XUV spectral region, with a relatively simple setup. Although the process can be completely described by a full-quantum theory [**38**], the use of a semiclassical model, called three-step model (TSM), is enough for understanding the basic features of the HHG. The teoretical description is fully derived from the works [**27, 39**]. Such model describes the process as a sequence of three different passages: tunnel-ionization, acceleration and recombination of the electron.

Consider for simplicity the 1-dimensional problem and let

$$\epsilon_L(t) = E_L cos(\omega_0 t) \tag{B.1}$$

be a linearly polarized laser electric field (we neglect the magnetic effects) at a given position $x = 0$. $\omega_0 = \frac{2\pi}{T_0}$ is the fundamental frequency and the phase of the field is set to zero. Consider an atom at the same position, with its own potential well. As the first step of the process, the radiation electric field "bends" the potential well, turning it into a barrier, as illustrated in figure B.1, step 1. The electron has therefore a non-zero probability of tunneling away from the parent ion, a fully-quantum process that can explain the ionization of an atom by means of a pulse with photon energy far below the ionization potential (for example, the photon energy of a pulse at 800 nm is only 1.5 eV,

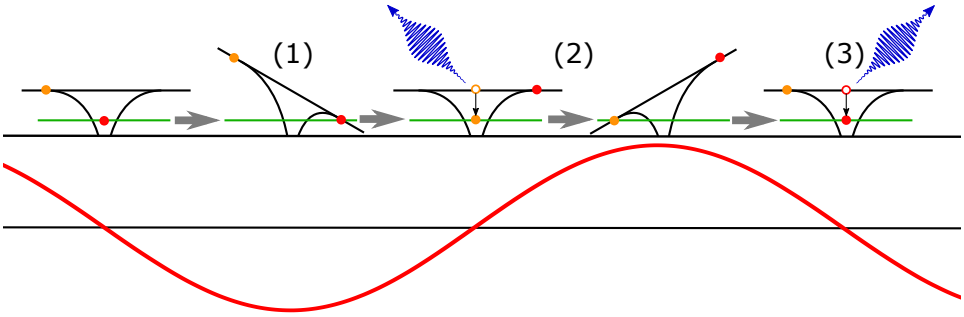


FIGURE B.1. Three-step model for high order harmonic generation. Consider the red circle, representing one electron. The driving pulse electric field "bends" the potential well of the atom, that is ionized by tunneling effect (1). Then, the electron is accelerated by the oscillating field and driven back to the parent ion (2), where it recombines: the excess energy is converted in a XUV pulse (3). The orange circle shows that two processes of this kind occur in parallel and therefore two bursts are generated per cycle of the laser radiation.

whereas the ionization potential of argon, typically used in HHG, is almost 16 eV, ten times larger). For simplicity, we assume that the electron is generated at the position of the parent ion ($x = 0$), with no kinetic energy ($v_0 = 0$, null initial velocity). A quantum theory, that we skip in this dissertation, is required for the calculation of the ionization rate. As a rule of thumb, the tunneling time, defined as the average time for the electron to cross the Coulomb barrier, can be estimated by assuming that the electron moves through with the same velocity it had in the ground state ($v_{gr}$). We can retrieve the ground state velocity from the expression of the kinetic energy, assumed equal to the electron energy in the bound state:

$$\frac{1}{2}m_e v_{gr}^2 = -E_b = I_p \tag{B.2}$$

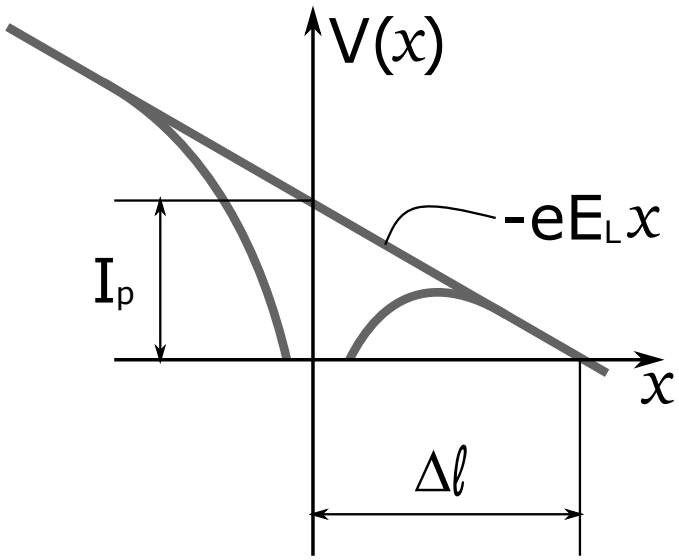


FIGURE B.2. Estimation of the width of the potential barrier induced by the laser electric field. The width $\Delta l$ can be estimated considering the slope of the laser electric potential.

where $E_b$ is the electron energy, corresponding to the ionization potential $I_p$, and $m_e$ is the electron mass. We find:

$$v_{gr} = \sqrt{\frac{2I_p}{m_e}} \tag{B.3}$$

Let $\Delta l$ be the width of the barrier, The tunneling time is

$$t_{tu} = \frac{\Delta l}{v_{gr}} \tag{B.4}$$

The barrier width can be easily estimated, as shown in figure B.2, by considering the slope of the electric potential of the laser radiation. In particular, we find

$$\Delta l = \frac{I_p}{eE_L} \tag{B.5}$$

where $e$ is the electron charge. Finally, the tunneling time is

$$t_{tu} = \frac{I_p/(eE_L)}{\sqrt{2I_p/m_e}} = \frac{\sqrt{2I_p m_e}}{2eE_L} \tag{B.6}$$

Once the electron has been emitted, it interacts with the electric field of the laser pulse, where we neglect the potential of the parent ion, and is accelerated (B.1 step 2). The second step can be treated classically. In this picture, the behavior of the electron is described by equation of motion

$$\frac{d^2x}{dt^2} = -\frac{e\epsilon_L(t)}{m_e} = -\frac{eE_L}{m_e}cos(\omega_0 t) \tag{B.7}$$

If the electron is emitted at time $t'$, the solution of Eq. B.7 is

$$x(t) = \frac{eE_L}{m_e\omega_0^2}\left\{[cos(\omega_0 t) - cos(\omega_0 t')] + \omega_0 sin(\omega_0 t')(t - t')\right\} \tag{B.8}$$

$$v(t) = -\frac{eE_L}{m_e\omega_0}\left[sin(\omega_0 t) - sin(\omega_0 t')\right] \tag{B.9}$$

where $v(t)$ is the electron velocity. Let $x_0 = \frac{eE_L}{m_e\omega_0^2}$: one can show that this value is the maximum displacement of the electrons, corresponding to the emission time $t' = 0$. Finally, to determine the energy of the radiation emitted after the recombination (B.1, step 3) we consider the electron kinetic energy, corresponding to the recombination time $t$, defined as usual by

$$E_k(t) = \frac{1}{2}m_e v^2(t) = 2U_p\left[sin(\omega_0 t) - sin(\omega_0 t')\right]^2 \tag{B.10}$$

where

$$U_p = \frac{(eE_L)^2}{4m_e\omega_0^2} \tag{B.11}$$

is the ponderomotive energy. This is, as defined, the kinetic energy acquired by the electron after a time $t$. If the electron recombines, this kinetic energy, plus the ionization potential, is converted in energy of the XUV photon. We find

$$\hbar\omega_X(t) = I_p + 2U_p\left[sin(\omega_0 t) - sin(\omega_0 t')\right]^2 \tag{B.12}$$

To properly evaluate the radiation properties, it is necessary to compute the recombination time. To do so, we can consider that the electron recombines if $x(t) = 0$, corresponding to the equation

$$[cos(\omega_0 t) - cos(\omega_0 t')] + \omega_0 sin(\omega_0 t')(t - t') = 0 \tag{B.13}$$

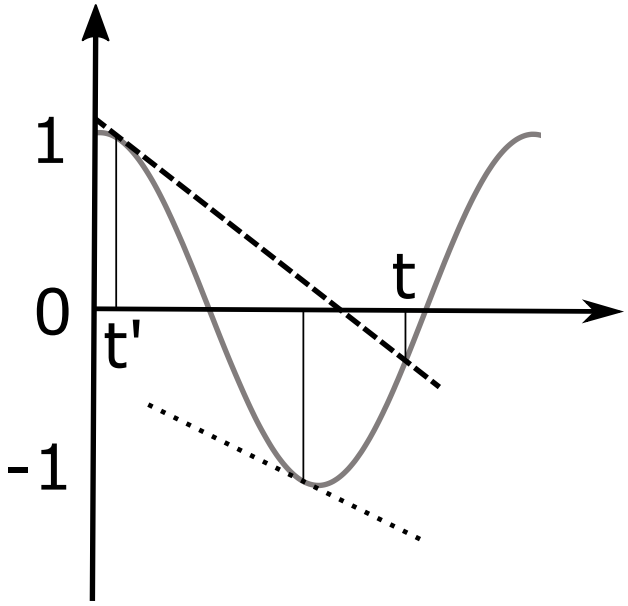


FIGURE B.3. Graphical solution of recombination equation: the solid line is the left-hand side of the equation. The dashed line represents the right-hand side of the equation, with an emission time $t'$, corresponding to the tangent in that point. The second intersection gives the recombination time $t$ (remember that the condition $t > t'$ holds. The dotted line shows that there exist some emission times for which the electron drifts away from the parent ion and never recombines.

Such equation has no analytical solution but it can be solved graphically. In particular, the equation can be rewritten as

$$cos(\omega_0 t) = cos(\omega_0 t') + \frac{d}{d(\omega_0 t)} cos(\omega_0 t') \Big|_{t'} \omega_0 (t - t') \tag{B.14}$$

The right-hand side of the equation corresponds to a straight line tangent to the function $cos(\omega_0 t)$ in the point $(t', cos(\omega_0 t'))$. Figure B.3 shows the graphical representation of the equation, for different $t'$. It

shows that, for some emission times $t'$ the equation has a solution, corresponding to a recombination time $t$ (dashed line). For example, electrons emitted at $t' = 0$ recombine after one optical cycle ($t = T_0$), with a null kinetic energy (see Eq. B.10) and corresponding XUV photon energy $\hbar\omega_X = I_p$ (Eq. B.12). This corresponds to the maximum round trip the electron can have in the laser field. Indeed, for later emission times, the recombination occurs earlier and earlier, until $t' = T_0/4$, corresponding to a recombination time $t = T_0/4$. In this case, the electron never leaves the parent ion. If we consider an emission for $T_0/4 < t' < T_0/2$ (dotted line in figure B.3) and considering that the recombination must always occur after the emission ($t > t'$), the electron never recombines to the parent ion and simply drifts away. Consider that, being the cosine function periodical, for $T_0/2 < t' < 3T_0/4$ the emitted electron recombines to the parent ion from the opposite direction with respect to the case we just discussed. This simple mathematical approach has a very straightforward physical interpretation, as it corresponds to a reference frame called the Kramers-Hanneberger frame. Here, the parent ion has a periodical motion, following the function $cos(\omega_0 t)$ whereas the electron is characterized by a linear drift, corresponding to the straight lines in the figure B.3.

Eq. B.14 can be solved numerically and the solution can be easily fitted by the following expression, useful for further analysis:

$$\frac{t}{T_0} = \frac{1}{4} - \frac{3}{2\pi} sin^{-1}\left(4\frac{t'}{T_0} - 1\right) \tag{B.15}$$

or in terms of the phase

$$\omega_0 t = \frac{\pi}{2} - 3sin^{-1}\left(\frac{2}{\pi}\omega_0 t' - 1\right) \tag{B.16}$$

The solution (Eq. B.15) is shown in figure B.4 The fact that the emission time spans for 0.75 times the laser period $T_0$ suggests that, for Ti:Sapphire laser at 800 nm, whose period is 2.7 fs, the XUV pulses may have a duration of less than 2 fs (about 1 fs FWHM). Upon satisfying some condition that we will discuss later, much shorter pulses

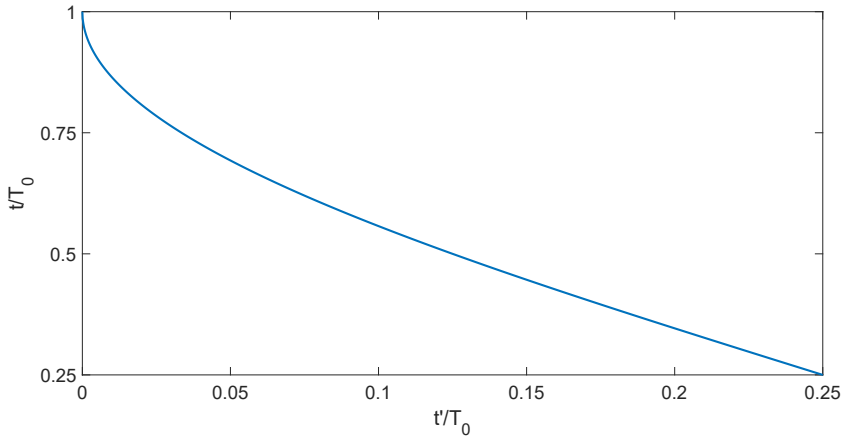


FIGURE B.4. Solution of recombination equation. Both axes are normalized with respect to the laser period.

can be generated. We can combine Eqs. B.16 and B.10 we can find the expression of the kinetic energy, as a function of the electron emission time $t'$. We find the expression

$$E_k(t') = 2U_p \left\{ cos \left[ 3sin^{-1} \left( \frac{2}{\pi} \omega_0 t' - 1 \right) \right] - sin\left(\omega_0 t'\right) \right\}^2 \tag{B.17}$$

Such result is illustrated in figure B.5 that shows the dependence of the kinetic energy on the electron emission time. As we can observe, the electrons can be emitted with a maximum kinetic energy $E_{k,max} \approx 3.17U_p$, corresponding to electrons with emission time $t' = 0.05\ T_0$ and return time $t' = 0.7\ T_0$. This means that this process can emit photons with maximum energy

$$\hbar\omega_{X,max} = I_p + 3.17U_p \tag{B.18}$$

the corresponding frequency is typically referred to as the cut-off frequency. An important consideration is that, in order to extend the spectral range of the generated harmonics, the ponderomotive energy should be as large as possible. Besides the use of high peak intensities of the laser beam, to reach such result we can use low-energy radiation, since $U_p$ grows quadratically as the laser frequency decreases. An

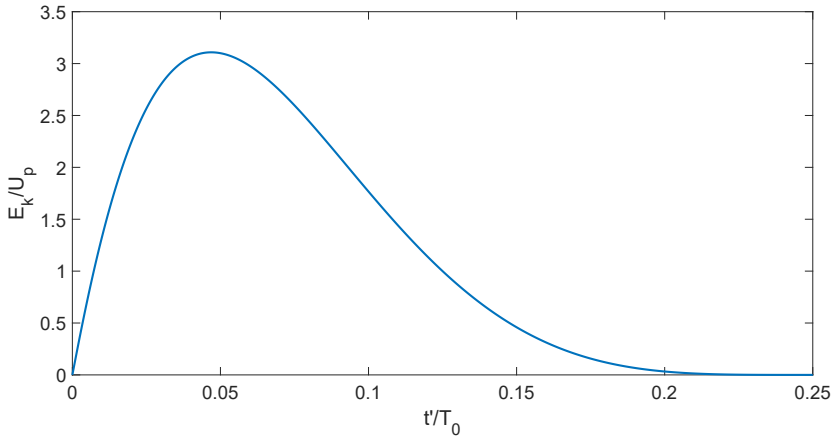


FIGURE B.5. Electron kinetic energy as a function of different emissions times. The maximum value of the kinetic energy is $E_{k,max} \approx 3.17U_p$, corresponding to the emission time $t' = 0.05\ T_0$ and return time $t' = 0.7\ T_0$.

estimation of the cut-off energy can by obtained by considering the following formula for the determination of the ponderomotive energy

$$U_p[eV] = 9.33 \times 10^{-14} I_L[W/cm^2](\lambda_0[\mu m])^2 \tag{B.19}$$

where $I_L$ is the laser intensity in $W/cm^2$ and $\lambda_0$ the fundamental wavelength in $\mu m$. With typical intensities ($1 \div 2 \times 10^{14} W/cm^2$), we obtain a ponderomotive energy of $6 \div 12 eV$, corresponding to maximum photon energies in the range $35 \div 50\ eV$, in line with the experiments. This cutoff law is, however, an approximation derived from a semiclassical approach. The full quantum theory [**38**] predicts a slightly larger cutoff energy:

$$\hbar\omega_{X,max} = 1.32 I_p + 3.17 U_p \tag{B.20}$$

Another important property of the HHG as described in this semiclassical approach is the fact that two different electrons, generated at different times, can have the same kinetic energy. This can be clearly seen in figure B.5. We have therefore two different situations for the

generation of the same spectrum, with different timing. In particular, since, as we said, electrons that are emitted earlier recombine later and electrons emitted later recombine earlier, we can call them "long-trajectory" electrons (with $t' < 0.05\ T_0$) and "short-trajectory" electrons (with $t' > 0.05\ T_0$), respectively. In this picture, suppressing one set of trajectories [**40**] or the other may lead to the emission of XUV pulses that are shorter than the ones we have estimated earlier in the discussion. For example, we can consider short trajectories only, whose recombination time, corresponding to the photon emission time, spans from $t = 0.25\ T_0$ to $t = 0.7\ T_0$. The corresponding pulse may last for 0.5 times the laser cycle $T_0$, with a duration for a Ti:Sapphire laser smaller than 1.3 fs (less than 650 as FWHM). In order to obtain such result, the long-trajectories have to be suppressed (same considerations can be made for suppressing the short trajectories in favor of the long ones). This can be done by some suitable phase-matching condition [**41**]. The details about the derivation of such condition are omitted in this dissertation. The basic idea is that, in order to have the shortest pulse possible, all the harmonics have to be emitted at the same time [**29**]. One can show that, for example, to eliminate the long trajectories we can simply place the generation medium after the fundamental laser beam focal point, alongside the propagation direction. In this case, a collinear phase matching is achieved and short-trajectory harmonics are generated along the same direction as the IR beam. The suppression of the long-trajectories, however, does not ensure the generation of a tranform-limited XUV burst. Indeed, the pulse generated either by short or long trajectories is always characterized by an intrinsic degree of chirp. Such property can be outlined by simply computing the electron kinetic energy as a function of the recombination time. This can be obtained by combining Eq. B.10 to the following equation

$$sin(\omega_0 t') = cos\left[\frac{\pi}{2} sin\left(\frac{1}{3}\omega_0 t - \frac{\pi}{6}\right)\right] \tag{B.21}$$

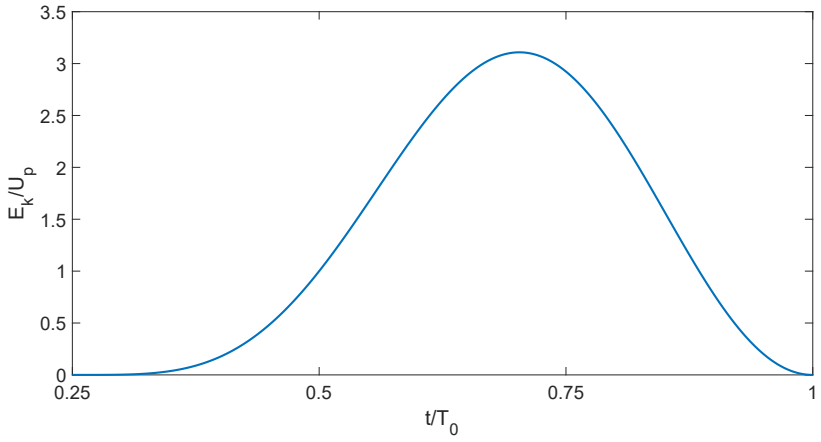


FIGURE B.6. Electron kinetic energy as a function of different recombination times. Considering the slope of such function as the chirp of the emitted radiation, the short-trajectory radiation (left-most part of the graph) has a positive chirp, whereas the long-trajectory one has it negative.

obtained from Eq. B.16. We obtain the kinetic energy as a function of the recombination time

$$E_K(t) = 2U_p \left\{ sin(\omega_0 t) - cos\left[ \frac{\pi}{2} sin\left( \frac{1}{3}\omega_0 t - \frac{\pi}{6} \right) \right] \right\}^2 \tag{B.22}$$

The result is also shown in figure B.6. Being the chirp related to the temporal derivative of the photon energy, directly related to the kinetic energy as follows

$$C = \frac{d(\hbar\omega_X)}{dt} = \frac{dE_k}{dt} \tag{B.23}$$

we can observe that the short-trajectory radiation ($t < 0.7\ T_0$) is positively chirped, whereas the long-trajectory one is negatively.

APPENDIX C

# Calculation of angle-resolved reflectance

The optical functions, such as reflection and transmission coefficients, for an arbitrarily complex layered structure can be obtained by means of a very powerful method, called the transfer-matrix method. We implemented such methodology on MATLAB®, whereas the theoretical description is fully derived from the work [**36**]. In this view, the full layered structure is associated to a matrix, called layer transfer matrix ($S$), that is able to bind the incident electric field to the one reflected and transmitted by the whole structure. In particular, describing the field by a forward (+) and back (-) propagating wave, as seen in Eq. C.1

$$\mathbf{E}(t) = \begin{bmatrix} E^{+}(t) \\ E^{-}(t) \end{bmatrix} \tag{C.1}$$

and considering a wave that impinges on the multilayer from one side only, such matrix is defined,in terms of its elements, as follows:

$$\begin{bmatrix} E^{(i)} \\ E^{(r)} \end{bmatrix} = \begin{bmatrix} S^{11} & S^{12} \\ S^{21} & S^{22} \end{bmatrix} \begin{bmatrix} E^{(t)} \\ 0 \end{bmatrix} \tag{C.2}$$

where $E^{(i)}$ is the (forward-propagating) *incident* wave, $E^{(r)}$ is the (back-propagating) *reflected* wave and $E^{(t)}$ is the (forward-propagating) *transmitted* wave (notice that the transfer matrix back-propagates the field). From this, one can easily retrieve

$$r = \frac{S^{21}}{S^{11}} \tag{C.3}$$

and

$$t = \frac{1}{S^{11}} \tag{C.4}$$

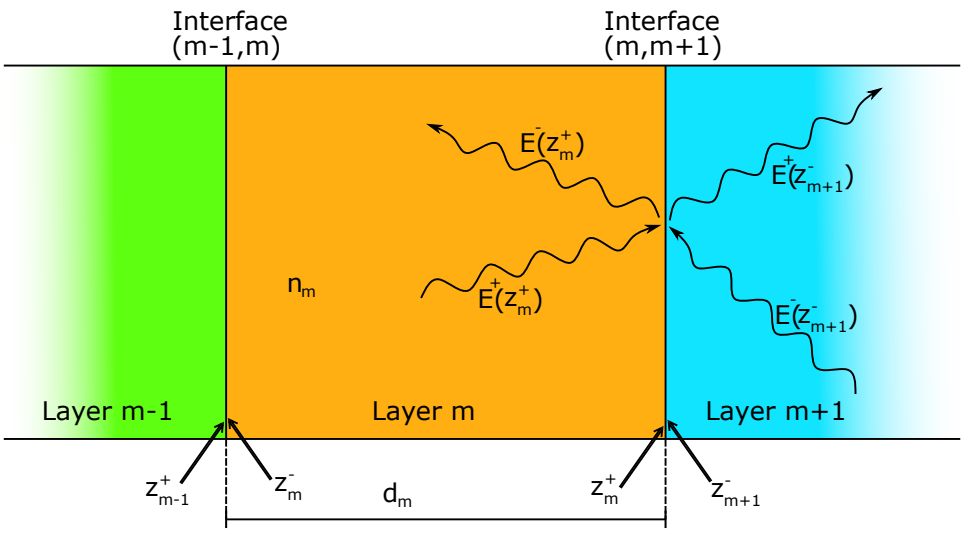


FIGURE C.1. Example of a multilayer structure. Each layer is identified by a number $m$, whereas each surface by a couple of number that indicate the corresponding layers on the left and on the right. Each layer has, of course, two interfaces, whose positions are identified by the quantity $z_m^{\pm}$, where the symbols $+$ and $-$ identify the right and left interfaces respectively. Being precise, $z_m^+$ indicates a position very close to the interface, but still inside layer $m$, and so on. The electric fields in such positions are also displayed. At each interface, the forward and back-propagating fields are represented by the symbols $+$ and $-$ respectively.

It now remains to determine the expression of the transfer matrix. In order to do this, we can simply consider that a multilayer structure is an ordered sequence of "bulky" layers and and interfaces. Let $m$ label the layer, where $m = 0$ represents the entrance medium and $m = M$ the substrate. Also, let $z_m^+$ be the "forward" and $z_m^-$ the "backward" interface positions for the layer m (see figure C.1). We can define the interface matrix ($I^{(m,m+1)}$), that binds the value of the electric field before and after the interface, and the layer matrix ($L^{(m)}$), binding the

electric field on the two sides of the same layer, such that

$$E(z_m^+) = I^{(m,m+1)} E(z_{m+1}^-) \tag{C.5}$$

and

$$E(z_m^-) = L^{(m)} E(z_m^+) \tag{C.6}$$

It is now quite easy to notice that the overall matrix can be composed as

$$S = I^{(0,1)} L^{(1)} I^{(1,2)} \cdots I^{(M-2,M-1)} L^{(M-1)} I^{(M-1,M)} \tag{C.7}$$

To finally obtain a usable formula for the matrix $S$ we need to determine the layer and interface matrices. The expression for $L^{(m)}$ is straightforward since it can be obtained by simply propagating the wave, assumed to be plane, through the layer. It immediately results in

$$L^{(m)} = \begin{bmatrix} exp(-i\gamma^{(m)}) & 0 \\ 0 & exp(i\gamma^{(m)}) \end{bmatrix} \tag{C.8}$$

where $\gamma^{(m)} = 2\pi n_m cos\theta_m d_m/\lambda$, $n_m$ is the refractive index of the layer, $d_m$ is thickness and $\theta_m$ the propagation angle, with respect to the normal.

The determination of the layer matrix is a little more complicated and requires the use of the Fresnel coefficients ($r^{(m,m+1)}$, $t^{(m,m+1)}$ and $r^{(m+1,m)}$, $t^{(m+1,m)}$, for the two sides of the interface). Consider, in particular, the forward and backward propagating wave from the interface $(m, m+1)$. It is easy to show that

$$\begin{aligned} E^+(z_{m+1}^-) &= t^{(m,m+1)} E^+(z_m^+) + r^{(m+1,m)} E^-(z_{m+1}^-) \\ E^-(z_m^+) &= r^{(m,m+1)} E^+(z_m^+) + t^{(m+1,m)} E^-(z_{m+1}^-) \end{aligned} \tag{C.9}$$

If we now rearrange the two expressions and use the Stokes relations, connecting the Fresnel coefficients on the two sides of the same interface, in the form

$$\begin{aligned} r^{(m,m+1)} &= -r^{(m+1,m)} \\ 1 &= (r^{(m,m+1)})^2 + t^{(m,m+1)} t^{(m+1,m)} \end{aligned} \tag{C.10}$$

we can easily obtain the Interface Matrix:

$$I^{(m,m+1)} = \frac{1}{t^{(m,m+1)}} \begin{bmatrix} 1 & r^{(m,m+1)} \\ r^{(m,m+1)} & 1 \end{bmatrix} \tag{C.11}$$

We can finally retrieve the $S$ matrix for a multilayer by simply computing, interface by interface, the Fresnel coefficients. Since in our apparatus we used s-polarized radiation, the relations read:

$$\begin{aligned} r_s^{(a,b)} &= \frac{n_a cos\theta_a - n_b \sqrt{1-(\frac{n_a}{n_b} sin\theta_a)^2}}{n_a cos\theta_a + n_b \sqrt{1-(\frac{n_a}{n_b} sin\theta_a)^2}} \\ t_s^{(a,b)} &= \frac{2n_a cos\theta a}{n_a cos\theta_a + n_b \sqrt{1-(\frac{n_a}{n_b} sin\theta_a)^2}} \end{aligned} \tag{C.12}$$

Notice that all the parameters we used, like the refractive index or the propagation angle, can be in principle complex number, also accounting for absorption in the considered medium.

In some cases, this approach is not enough for a correct evaluation of the optical functions of a multilayer. Indeed, the impact of the surface roughness of the structure can dramatically effect the reflection and transmission properties. There exist several ways for evaluating such a property. A very easy tool, typically used for studying the impact of the residual manufacturing errors and tolerances on the optical elements fabrication, is the so-called total integrated scatter (TIS) [**42**]. Despite this method is mainly used in a wavelength range from IR to near UV, we can assume that it still holds in the XUV region.

In general, the reflection from a surface is simply defined as the ratio between the total reflected intensity and the incident intensity. However, in a real surface, always characterized by residual roughness, the reflectance is always made of two separate contribution: the specular reflectance, with the incident power reflected in a well determined direction, like in an ideal mirror, and the diffused or scattered reflectance, with the incident power reflected in random directions. Considering a moderately rough surface, the fraction of the total reflected intensity that is diffusely reflected, a sort of specular reflectance efficiency, can

be estimated by

$$\frac{R_s}{R_t} = exp\left[-(4\pi cos\theta_i \sigma/\lambda)^2\right] \tag{C.13}$$

where $R_s$ is the specular reflectance, $R_t$ is the total reflectance, $\theta_i$ is the incidence angle, $\sigma$ is the surface roughness root-mean-square (rms) and $\lambda$ is the radiation wavelength. On the other hand, the total integrated scatter is defined as the ration of the diffused reflectance ($R_d$) over the total reflectance. Since $R_t = R_s + R_d$, we find

$$TIS = 1 - exp\left[-(4\pi cos\theta_i \sigma/\lambda)^2\right] \tag{C.14}$$

APPENDIX D

# Determination of the refractive index

According to the online dictionary of crystallography, by the international union of crystallography, the scattering factor is "a measure of the scattering power of an isolated atom" [**43**] and depends both on the atom and radiation properties. In general, the scattering of XUV or X-Ray is due to the interaction of the electromagnetic field of the incoming radiation and the electronic cloud in the system. In particular, the efficiency of such process depends on the number of electrons in the atom, corresponding to the atomic number $Z$, and more in general on the full electron distribution. Indeed, the corresponding scattering factor can be easily computed as the spatial Fourier transform of the atomic electron distribution

$$f = \int_{-\infty}^{+\infty} \rho(\mathbf{r}) e^{i\mathbf{k}\cdot\mathbf{r}} d^3\mathbf{r} \tag{D.1}$$

Being in general a complex value, we can consider its real and imaginary parts, such that

$$f = f_1 + i f_2 \tag{D.2}$$

The real and imaginary parts of this values can be directly estimated by the properties of the atom under analysis [**31**]. The imaginary part is directly derived from the absorption cross-section $\sigma_a$

$$f_2 = \frac{\sigma_a}{2 r_e \lambda} \tag{D.3}$$

where $r_e$ is the classical electron radius and $\lambda$ the radiation wavelength. The real part, instead, is related to the imaginary part of the Kramers-Kronig dispersion relation

$$f_1 = Z^* + \frac{1}{\pi r_e hc} \int_0^{+\infty} \frac{\epsilon^2 \sigma_a(\epsilon)}{E^2 - \epsilon^2} d\epsilon \tag{D.4}$$

where $E$ is the photon energy and $Z^* = Z - (Z/82.5)^{2.37}$ is the atomic number with a small relativistic correction. The values of the scattering factors can be, therefore, computed, despite they are available in the literature. From such values it is possible to give an estimation of the refractive index, as a function of the wavelength, in any chemical compound of known structure. In particular, one can see that [**31**]

$$n = 1 - \frac{r_e \lambda^2}{2\pi} \sum_{k=1}^{K} N_k \left( f_{1,k} - i f_{2,k} \right) \tag{D.5}$$

where $r_e$ is the classical electron radius, $N_k$ is the number of atoms of type $k$ per unit volume and $f_{1,k} - i f_{2,k}$ is the complex, energy-dependent atomic scattering factor for each type of atoms present in the compound of which we are computing the refractive index. The sign of the imaginary part of the scattering factor, directly related to the sign of the imaginary part of the refractive index accounting for absorption, depends on the reference frame for the propagation of the electromagnetic wave. Such expression is very useful and powerful, as the atomic scattering factors are well characterized. Unfortunately, it produces a very precise result only for photon energies greater than 30 eV.

# Bibliography


[1] Shah, Jagdeep. Ultrafast spectroscopy of semiconductors and semiconductor nanostructures. Vol. 115. Springer Science & Business Media, 2013.

[2] König, Dirk, et al. "Hot carrier solar cells: Principles, materials and design." Physica E: Low-dimensional Systems and Nanostructures 42.10 (2010): 2862-2866.

[3] Loh, Zhi-Heng, et al. "Quantum state-resolved probing of strong-field-ionized xenon atoms using femtosecond high-order harmonic transient absorption spectroscopy." Physical review letters 98.14 (2007): 143601.

[4] Goulielmakis, Eleftherios, et al. "Real-time observation of valence electron motion." Nature 466.7307 (2010): 739.

[5] Wang, He, et al. "Attosecond time-resolved autoionization of argon." Physical review letters 105.14 (2010): 143002.

[6] Holler, M., et al. "Attosecond electron wave-packet interference observed by transient absorption." Physical review letters 106.12 (2011): 123601.

[7] Schultze, Martin, et al. "Controlling dielectrics with the electric field of light." Nature 493.7430 (2013): 75.

[8] Mashiko, Hiroki, et al. "Petahertz optical drive with wide-bandgap semiconductor." Nature Physics 12.8 (2016): 741.

[9] Schultze, Martin, et al. "Attosecond band-gap dynamics in silicon." Science 346.6215 (2014): 1348-1352.

[10] Cho, B. I., et al. "Electronic structure of warm dense copper studied by ultrafast x-ray absorption spectroscopy." Physical review letters 106.16 (2011): 167601.

[11] Lucchini, M., et al. "Attosecond dynamical Franz-Keldysh effect in polycrystalline diamond." Science 353.6302 (2016): 916-919.

[12] Mathias, Stefan, et al. "Probing the timescale of the exchange interaction in a ferromagnetic alloy." Proceedings of the National Academy of Sciences (2012).

[13] Turgut, Emrah, et al. "Controlling the competition between optically induced ultrafast spin-flip scattering and spin transport in magnetic multilayers." Physical review letters 110.19 (2013): 197201.

[14] Husek, Jakub, et al. "Surface electron dynamics in hematite ($\alpha$-Fe 2 O 3): correlation between ultrafast surface electron trapping and small polaron formation." Chemical science 8.12 (2017): 8170-8178.

[15] Hasan, M. Zahid, and Charles L. Kane. "Colloquium: topological insulators." Reviews of Modern Physics 82.4 (2010): 3045.

[16] König, Markus, et al. "Quantum spin Hall insulator state in HgTe quantum wells." Science 318.5851 (2007): 766-770.

[17] Kaplan, Christopher J., et al. "Femtosecond tracking of carrier relaxation in germanium with extreme ultraviolet transient reflectivity." Physical Review B 97.20 (2018): 205202.

[18] Kraus, Peter M., et al. "Attosecond kinetics of photoexcited Germanium." CLEO: QELS_Fundamental Science. Optical Society of America, 2017.

[19] Attwood, David, and Anne Sakdinawat. X-rays and Extreme Ultraviolet Radiation: Principles and Applications. Cambridge university press, 2017.

[20] Kittel, Charles, Paul McEuen, and Paul McEuen. Introduction to solid state physics. Vol. 8. New York: Wiley, 1996.

[21] Nisoli, Mauro, et al. "Toward a terawatt-scale sub-10-fs laser technology." IEEE Journal of selected topics in quantum electronics 4.2 (1998): 414-420.

[22] Trebino, Rick, and Daniel J. Kane. "Using phase retrieval to measure the intensity and phase of ultrashort pulses: frequency-resolved optical gating." JOSA A 10.5 (1993): 1101-1111.

[23] Muller, H. _. G. "Reconstruction of attosecond harmonic beating by interference of two-photon transitions." Applied Physics B 74.1 (2002): s17-s21.

[24] Mairesse, Yann, and F. Quéré. "Frequency-resolved optical gating for complete reconstruction of attosecond bursts." Physical Review A 71.1 (2005): 011401.

[25] Trebino, Rick, et al. "Measuring ultrashort laser pulses in the time-frequency domain using frequency-resolved optical gating." Review of Scientific Instruments 68.9 (1997): 3277-3295.

[26] DeLong, Kenneth W., et al. "Pulse retrieval in frequency-resolved optical gating based on the method of generalized projections." Optics letters 19.24 (1994): 2152-2154.

[27] Chang, Zenghu. Fundamentals of attosecond optics. CRC Press, 2016.

[28] Paul, P. M., et al. "Observation of a train of attosecond pulses from high harmonic generation." Science 292.5522 (2001): 1689-1692.

[29] Mairesse, Y., et al. "Attosecond synchronization of high-harmonic soft x-rays." Science 302.5650 (2003): 1540-1543.

[30] Jordan, Inga, and Hans Jakob Wörner. "Extracting attosecond delays from spectrally overlapping interferograms." Journal of Optics 20.2 (2018): 024013.

[31] Thompson, A., et al. "X-ray data booklet (2009)." URL http://xdb. lbl. gov (2009).

[32] Cattaneo, Laura, et al. "Comparison of attosecond streaking and RABBITT." Optics express 24.25 (2016): 29060-29076.

[33] Lucchini, Matteo, et al. "Ptychographic reconstruction of attosecond pulses." Optics express 23.23 (2015): 29502-29513.

[34] McCallum, B. C., and J. M. Rodenburg. "Two-dimensional demonstration of Wigner phase-retrieval microscopy in the STEM configuration." Ultramicroscopy 45.3-4 (1992): 371-380.

[35] Maiden, Andrew M., and John M. Rodenburg. "An improved ptychographical phase retrieval algorithm for diffractive imaging." Ultramicroscopy 109.10 (2009): 1256-1262.

[36] J. P. Landry, "Appendix B: Reflection and Transmission of Light from Multilayer Films", https://jameslandry.files.wordpress.com/2012/02/09-appendix-b.pdf, [15/08/2018].

[37] Pouilleau, Jerome, et al. "Structure and composition of passive titanium oxide films." Materials Science and Engineering: B 47.3 (1997): 235-243.

[38] Lewenstein, Maciej, et al. "Theory of high-harmonic generation by low-frequency laser fields." Physical Review A 49.3 (1994): 2117.

[39] Corkum, Paul B. "Plasma perspective on strong field multiphoton ionization." Physical Review Letters 71.13 (1993): 1994.

[40] Sansone, G., et al. "Control of long electron quantum paths in high-order harmonic generation by phase-stabilized light pulses." Physical Review A 73.5 (2006): 053408.

[41] Balcou, Philippe, et al. "Generalized phase-matching conditions for high harmonics: The role of field-gradient forces." Physical Review A 55.4 (1997): 3204.

[42] Harvey, James E., et al. "Total integrated scatter from surfaces with arbitrary roughness, correlation widths, and incident angles." Optical Engineering 51.1 (2012): 013402.

[43] International union of crystallography, Online dictionary of crystallography, http://reference.iucr.org/dictionary/Atomic_scattering_factor, [18/08/2018].

[44] Suda, Akira, et al. "Generation of sub-10-fs, 5-mJ-optical pulses using a hollow fiber with a pressure gradient." Applied Physics Letters 86.11 (2005): 111116.

[45] Corkum, P. B. "PB Corkum, NH Burnett, and MY Ivanov, Opt. Lett. 19, 1870 (1994)." Opt. Lett. 19 (1994): 1870.

[46] Kaplan, D., and P. Tournois. "Theory and performance of the acousto optic programmable dispersive filter used for femtosecond laser pulse shaping." Journal de Physique IV (Proceedings). Vol. 12. No. 5. EDP sciences, 2002.

[47] Verluise, Frédéric, et al. "Arbitrary dispersion control of ultrashort optical pulses with acoustic waves." JOSA B 17.1 (2000): 138-145.

[48] Verluise, Frederic, et al. "Amplitude and phase control of ultrashort pulses by use of an acousto-optic programmable dispersive filter: pulse compression and shaping." Optics letters 25.8 (2000): 575-577.

[49] Oksenhendler, Thomas, et al. "Intracavity acousto-optic programmable gain control for ultra-wide-band regenerative amplifiers." Applied Physics B 83.4 (2006): 491.

[50] Telle, Harald R., et al. "Carrier-envelope offset phase control: A novel concept for absolute optical frequency measurement and ultrashort pulse generation." Applied Physics B 69.4 (1999): 327-332.

[51] Jones, David J., et al. "Carrier-envelope phase control of femtosecond mode-locked lasers and direct optical frequency synthesis." Science 288.5466 (2000): 635-639.

[52] Xu, Lin, et al. "Route to phase control of ultrashort light pulses." Optics letters 21.24 (1996): 2008-2010.

# Acknowledgments

Innanzitutto, ci tengo a ringraziare il Professor Mauro Nisoli e il Dottor Matteo Lucchini, per avermi dato la possibilità di fare un'esperienza così positiva, mostrandomi con quanta fatica e sudore si fa la scienza.
Ringrazio Davide, lo sherpa che mi ha guidato nei meandri del laboratorio, con cui ho condiviso il bello e il brutto di questo mondo, ma sempre con il sorriso sulle labbra e qualche canzone di sottofondo, e Mario, un vero punto di riferimento per (quasi) ogni cosa.
Ringrazio la mia famiglia tutta, che sin dall'inizio ha creduto in me e mi ha sostenuto, da vicino e da lontano con la stessa intensità.
Ringrazio i miei amici che, tra un drink e un sushi, mi hanno sempre dato la forza di andare avanti e superare ogni avversità.
Ringrazio Simo. Non basterebbero tutte le pagine di questo mondo per dire quanto hai fatto per me.